Microfluidic Capillary in a Waveguide Resonator for Chemical and Biochemical Sensing

Elizabeth Lee (née McKeever)

Submitted for the degree of Doctor of Philosophy

Heriot-Watt University

School of Engineering and Physical Sciences

August 2015

Abstract

This thesis presents a novel microwave sensor for the characterisation of fluids with the integration of a microfluidic capillary.

Various designs and fabrication methods were investigated for the integrated microfluidic capillary. SU-8 and PDMS were investigated as possible materials, however proved difficult to produce large volumes of capillaries. PMMA a cheap readily available material was also investigated. Using an Epilog CO2 laser ablation machine rapid prototyping of microfluidic capillaries was achieved using PMMA.

Two microwave resonator designs are proposed as non-contact sensing devices. The first design utilizes an E-plane filter in a split-block rectangular waveguide housing. This offers advantages in enhanced near fields and simple manufacturing techniques. Simulation and experimental results are presented, demonstrating sensitivity of such microwave sensors. Various materials under test were used: Methylated spirit/water concentrations, lubricant and motor oils and animal red blood cell concentrations. Resonant frequency shifts in the region of 10s of MHz were observed. However most notably in the methylated spirit concentrations there was no resonant frequency shift, only a shift in the return losses were observed. The integration of the E-plane filter and the microfluidic capillary resulted in poor repeatability due to alignment issues of the filter and capillary.

The second design incorporates the use of Distributed Bragg Reflectors for a compact and fully integrated, no moving parts, device. The simulation results produced a Q-factor 1,942 at a resonant frequency of 23.3 GHz. The Bragg sensor produced promising simulation results as well as initial experimental results. There was up to 20 MHz resonant frequency shift between the samples. Samples included Eppendorf tubes filled with water and oil.

Dedication

For my Mum

Acknowledgements

Firstly, I would like to thank Prof. Marc Desmulliez for giving me the opportunity to study within the MISEC research group and for his guidance and support throughout.

I would like to thank Dr. Sumanth Pavuluri for his help and tips on HFSS modelling and general microwave theory. I also thank Dr. Deirdre Kavanagh for help with SU-8 fabrication and biological cell preparation.

I am grateful to Yves for letting me sit him for 4 years and for the conversations and LTCC help. I would like to thank Stefan Wilhelm for his invaluable help with the Epilog and LTCC fabrication.

I would also like to thank all the past and present MISEC members for their friendship, advice and support. Namely (and in no particular order): Alex, Shilong, Jia Ni, Iqy, Soni, Dave W, Ross, Maria, Wenxing, Curro, Dave H, Raul, Gordon, Suzanne, Jack, Maiwenn, Scott, Brian.

Most importantly I would like to thank my Dad, and two sisters, Yvonne and Michelle, and my husband Kris for their everlasting support and love.

Without all the people mentioned above I would not be the person I am today, all giving me the strength and drive to succeed and complete this project.

DECLARATION STATEMENT

(Research Thesis Submission Form should be placed here

Contents

1 Introduction

1.1 Background and Motivation

The demand for sensors has grown tremendously over the recent years as the automation of industrial processes becomes more prevalent. Various applications require rapid characterisation of materials including biomedical, environmental and industrial systems monitoring. Microwave sensors in particular have become more common as they work in a wide range of areas that required distance, movement, shape and particle size to be measured accurately and in a reproducible manner. However, microwave sensors can also be used for the characterisation of material properties. This is achieved by an interaction between the microwaves and the material under test. The interaction can be in the form of reflection, refraction, scattering, emission, absorption, or change of speed or phase. The interaction between the microwaves and the medium of propagation is completely determined by the relative permittivity of the medium. Different materials have different permittivities with the permittivity of a mixture depending on the permittivity of the components. The increasing number of components in the mixture adds to the total unknowns and therefore several microwave parameters are required e.g. resonant frequency, quality factor, insertion loss and phase. There are many advantages and disadvantages of using microwaves as sensors. Advantages include:

- Microwave sensors do not need mechanical contact with the material under test.
- Microwaves penetrate all materials except metals. The measured result therefore represents a volume of the material, not only the surface.
- There is an excellent contrast between water and most other materials using microwaves, making them well suited for water content measurements.
- Microwave resonator sensors are inherently stable because the resonant frequency is related to the physical dimensions of the sensor
- The power levels used for microwave sensors are very low and are therefore safe unlike radio-active sources.
- The microwaves do not affect the material under test

The disadvantages are as follow:

- As the frequency increased so does the cost of the device
- Microwave sensors must be calibrated separately for different materials; this makes them very specific to their application, resulting in low universal acceptability.

In the face of the large number of advantages that microwave sensing encompasses, a number of microwave technologies have been implemented as non-contact sensing devices. Microwave cavity perturbation works on the principle of perturbing a resonant cavity with the sample material. This has been carried out in various works by Lin *et al*. [1.1] and Nikawa and Guan [1.2]. Each of their devices uses solid samples in various waveguide cavity designs. Only a handful of devices have liquid sensing capabilities such as those found in the works of Kawabata *et al*. [1.3] and Saeed [1.4], however these devices operate at lower frequencies of less than 6 GHz. In order to achieve high sensitivities higher frequency devices such as coplanar waveguides have been demonstrated by Grenier *et al.* [1.5] and Mateu *et al.* [1.6] amongst others. The advantages of such circuits is the fabrication process using photolithography which is a well-established technique. The difficulty with these devices lies in the incorporation of the microfluidic channels for fluid measurement. Dalmay *et al*. [1.7] negated the use of the microfluidic channel all together and used freeze dried cell samples. This involves a rigorous sample preparation requiring highly skilled staff that would be time consuming. The increased sensitivity with increased frequency has been developed by Treizebre *et al*. [1.8]. A Terahertz frequency device, greater than 100 GHz, was created using standard photolithography processes and was able to demonstrate high sensitivity in measuring various cell concentrations. However at this frequency range absorption of water molecules could prove to be detrimental especially with biological cells. Therefore this thesis will demonstrate an X-band waveguide resonator device with integrated microfluidic capillaries for sensing.

Microfluidics allows the sensor to work with micro-, nano- and even pico-litre volumes. This has the advantage of reduced sample size and reagent volume reducing cost and extending the use of the sample by allowing a larger number of tests to be performed on the same sample. Quantities of waste are also reduced.

Using a waveguide resonator as the sensing device offers a non-contact sensor with no adverse effects to the sample tested. Integrating an E-plane resonator with enhanced near fields increases the devices capability as a sensor.

A second device is also investigated using the well-documented Bragg reflections at microwave frequencies. As the resonator device is fully integrated there are no alignment

problems between the sample under test and the microwave field. The sample can be introduced externally ensuring no contact with the resonant structure.

1.2 Objectives of the thesis

The main objective of this thesis is to investigate an E-plane filter configuration for use as a biochemical sensor. The work includes:

- Using Finite Element Method (FEM) software to analyse and design a suitable E-plane filter
- Investigate techniques for fabricating microfluidic channels. As this device is intended for use with biological medium the material for the channels must be biocompatible.
- Conduct experiments of the e-plane sensor with an integrated microfluidic channel. Various fluids including solvents, oils, biological medium including live cells.
- Comparisons between the model of the sensor and the empirical results to obtain characterisation data of different materials.

In addition higher quality factor devices will also be investigated. The objectives for this will include:

- Investigation of Distributed Bragg Reflector (DBR) resonators for use as a sensing device.
- Design and fabrication of a DBR resonator using the FEM software. The material sapphire is used for the low-loss dielectric reflectors.
- Conduct preliminary test on the DBR resonator sensor using similar materials under test as in the E-plane sensor experiments.

1.3 Structure of the thesis

This thesis is organised according the following structure shown in Figure 1.1:

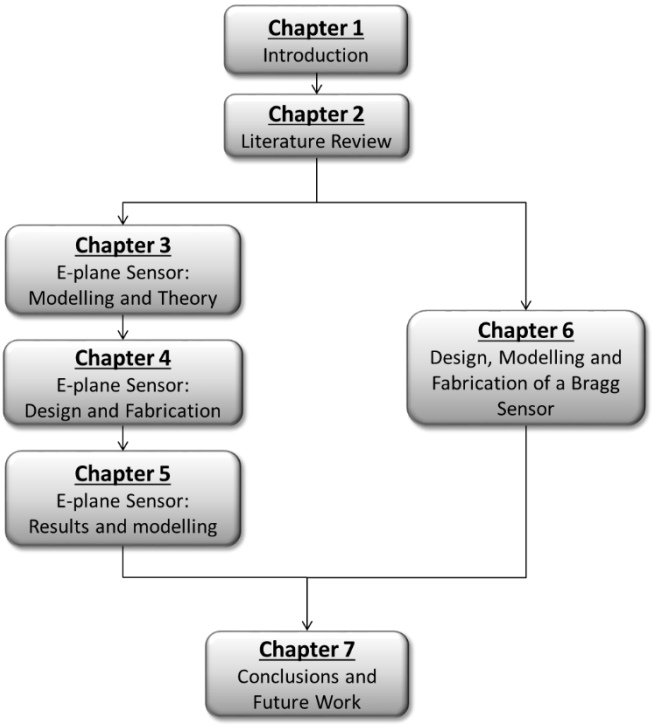

Figure 1.1: Schematic flow diagram of the thesis layout

Chapter 2 Literature Review includes an up-to-date review of the various sensors using microwave and Terahertz frequencies, as well as the design of the high Q-factor DBR resonators. Emphasis has been given to sensors that have incorporated microfluidic channels in line with the objectives of this work.

Chapter 3 Modelling and Theory of E-plane Sensor will present the methods used to design an E-plane filter for the sensing device. It includes an investigation into the effects of introducing microfluidic capillaries into the waveguide analysis. Finite Element Modelling (FEM) techniques using the Ansoft HFSS software package is investigated.

Chapter 4 Design and Fabrication of the E-plane Sensor will focus on the design strategies of the microfluidic channels and the difficulties in fabrication. Studies are also performed on the reproducibility and repeatability of the different fabrication techniques. Fabrication of the waveguide resonator is also included with options of incorporating the microfluidic channels.

Chapter 5 Results and Modelling of E-plane Sensor analyses the experimental results achieved using the various designs of microfluidic channels. These results are then compared to the simulated models produced in HFSS for Chapter 3. Studies include aqueous solutions, dilutions of alcohols, as well as investigations of animal blood cells and plasma.

Chapter 6 Design and Modelling of Bragg Sensor investigates the various techniques used to calculate the optimised design for the Distributed Bragg Reflector resonators. This includes Finite Element analysis using Ansoft HFSS. The fabrication of the prototype sensor and preliminary results of the DBR resonator sensor are also presented

The thesis concludes with **Chapter 7 Conclusions and Future Work.**

1.4 References

[1.1] L. Mi, W. Yong, and M. N. Afsar, "Precision measurement of complex permittivity and permeability by microwave cavity perturbation technique." pp. 62-63 vol. 1.

[1.2] Y. Nikawa, and G. Yong, "Dynamic Measurement of Temperature Dependent Complex Permittivity of Material by Microwave Heating Using Cylindrical Cavity Resonator." pp. 1-4.

[1.3] H. Kawabata, and Y. Kobayashi, "Accurate measurements of complex permittivity of liquid based on a TM₀₁₀ mode cylindrical cavity method." p. 4 pp.

[1.4] K. Saeed, R. D. Pollard, and I. C. Hunter, "Substrate Integrated Waveguide Cavity Resonators for Complex Permittivity Characterization of Materials," *Microwave Theory and Techniques, IEEE Transactions on,* vol. 56, no. 10, pp. 2340-2347, 2008.

[1.5] K. Grenier, D. Dubuc, P. E. Poleni, M. Kumemura, H. Toshiyoshi, T. Fujii, and H. Fujita, "Integrated Broadband Microwave and Microfluidic Sensor Dedicated to Bioengineering," *Microwave Theory and Techniques, IEEE Transactions on,* vol. 57, no. 12, pp. 3246-3253, 2009.

[1.6] J. Mateu, N. Orloff, M. Rinehart, and J. C. Booth, "Broadband Permittivity of Liquids Extracted from Transmission Line Measurements of Microfluidic Channels." pp. 523-526.

[1.7] C. Dalmay, A. Pothier, P. Blondy, F. Lalloue, and M. O. Jauberteau, "Label free biosensors for human cell characterization using radio and microwave frequencies." pp. 911-914.

[1.8] A. Treizebre, B. Bocquet, D. Legrand, and J. Mazurier, "Studies of cellular informative transfer by THz BioMEMS." pp. 1-2.

2 Literature Review

Characterization of fluid samples is becoming increasingly important in medical, biomedical and industrial applications as well as in academic research. In that regard, the electromagnetic characterization of such materials is emerging as an alternative solution to optical and chemical detection schemes, both of which require the chemical alteration of the sample prior to analysis; a process, which is time consuming and requires specialised technicians. In contrast, electromagnetic detection is a label free technique offering a highly sensitive approach to material characterization. This literature review outlines the different approaches in electromagnetic characterization over the widest range of frequencies ranging from Very Low Frequency (VLF) devices to systems that operate in the terahertz frequency region.

The electromagnetic spectrum, shown in Figure 2.1**,** outlines the different regions of electromagnetic radiation. The Very Low Frequencies (VLF) range is located in the region marked 'radio', in which the electromagnetic radiation has a frequency of less than 10^8 Hz. Section 2.1 will discuss the various sensing techniques at this frequency range.

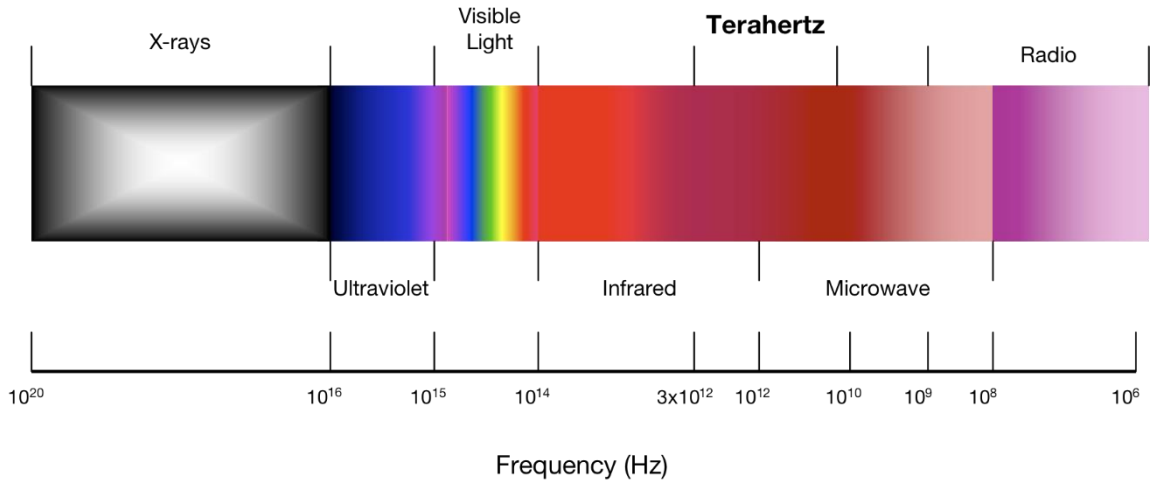

Figure 2.1 Electromagnetic spectrum

The subsequent section, entitled 2.2 Millimetre/Microwave Sensing, will present an extensive review of the various sensing techniques at the microwave frequencies ranging from 10^8 to 10^{10} Hz. This frequency range offers a higher level of sensitivity compared to VLF with the ability to manufacture microdevices and integrate microfluidics to support the sensing of various gases and liquids. Many microfabricated devices have basic

rectangular/circular waveguides; others have more complex coplanar device configurations.

The third section, Terahertz (THz) Frequency Sensing, will look at the heavily researched but still relatively unexploited Terahertz frequency region, which lies between the microwave and infrared domains of the electromagnetic spectrum. Traditionally associated with astronomy, Terahertz technology is emerging in other areas of science and technology with industrial applications in national security [2.1], medicine [2.2], chemistry [2.3] and pharmaceuticals [2.4], some of which will be discussed in that section. The penultimate section will focus on the Bragg reflection waveguide methods of sensing. This application has not been explored extensively, which is why part of this project will be researching this area. The chapter finishes with some conclusions of the work reviewed in the various sections, which includes a comparison table evaluating the different sensing techniques, based on frequency, fabrication techniques and achieved sensitivity.

2.1 Very Low Frequencies (VLF) Sensing

Dielectric spectroscopy examines the permittivity of a sample as a function of frequency. Facer *et al*. developed a microfabricated waveguide for the analysis of biological samples [2.5]. The device is fabricated on a glass substrate with a titanium/aluminium coplanar waveguide (CPW). The samples are confined within a microfluidic well or channel fabricated in PDMS. A schematic of the device showing the CPW, microfluidic channel, and connectors, is shown below in Figure 2.2.**Error! Reference source not found.**

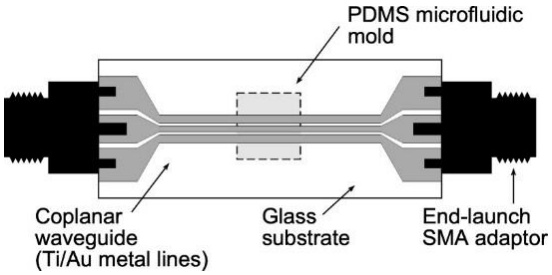

Figure 2.2 CPW device, showing the Ti/Au waveguide (not to scale) and microfluidic sample containment [2.5].

The samples, measured with this device, included solutions of haemoglobin, bacteriophageλ-DNA, and live E-*coli* suspensions. The results are shown in Figure 2.3 for the samples in a 10 μL capped well over a frequency range of 40 Hz to 26.5 GHz.

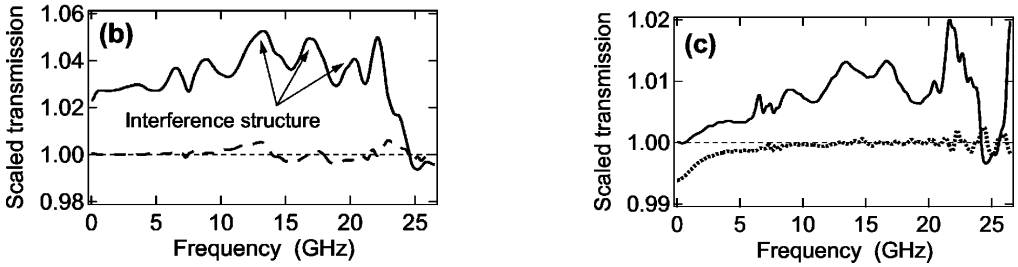

Figure 2.3 Normalised transmission data for (b) haemoglobin (solid trace) and phage λ-DNA (dashed line) (c) E.coli (solid) and Tris buffer from the haemoglobin solution (dashed) [2.5].

Facer *et al.* demonstrated various transmission data for live cell suspensions. Although this work covers a wide frequency range that is useful for spectroscopy analysis, its use as a sensor is limited by the lack of quantitative frequency features. For example the data above shows that there are interference structures that are caused by the connections used in the experimental setup.

Another low frequency method involves the use of interdigitated capacitor arrays as demonstrated by Qureshi *et al.* [2.6]. They present a label free capacitive biosensor for the sensitive detection of multiple biomarkers using gold interdigitated capacitor arrays. In order to detect the biomarkers an immunoassay is used where recognition elements, such as antibodies, are immobilized onto the electrode surface. When an analyte binds, changes in the dielectric properties can be observed. A schematic of the complete device is shown in Figure 2.4.

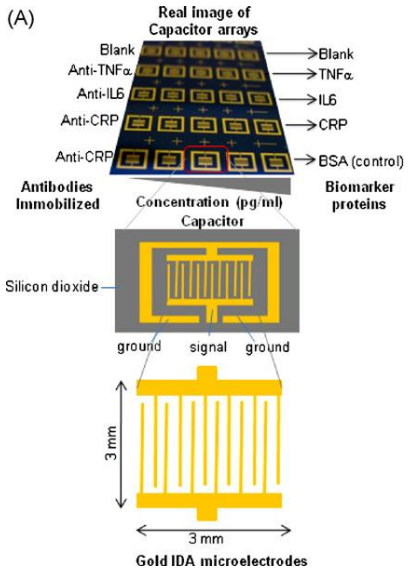

Figure 2.4 Schematic representation of the gold interdigitated capacitor array chip [2.6].

The devices were tested over the frequency range of 50 MHz to 173 MHz using a Vector Network Analyser (VNA) and probe station. The dielectric constant was extracted using the following equation

$$C = \frac{2n\varepsilon\varepsilon_0 A}{d} \qquad (2.1)$$

Where C is the capacitance of the overall structure, n is the number of electrodes, ε_0 is the permittivity of free space, A is the area of the electrodes, and d is the distance between the electrodes. The relative dielectric constant of the medium between the plates, ε, is extracted using the above equation. This is multiplied by a factor of two to represent each electrode forming two capacitors. The measurement results are shown in Figure 2.5, and give the dielectric constant against frequency for varying concentrations.

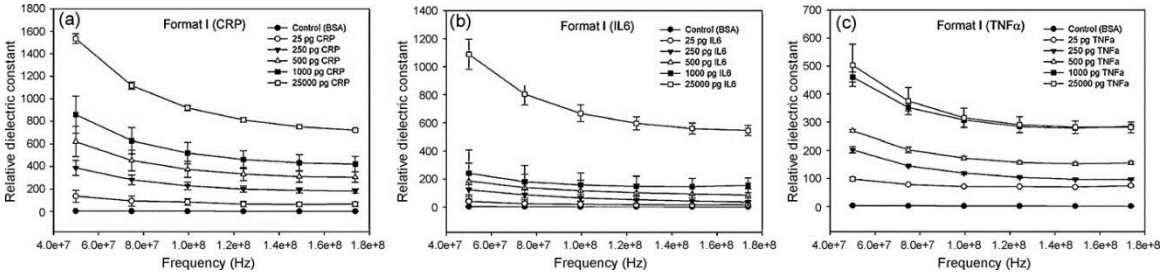

Figure 2.5 Changes in dielectric responses to different concentration of pure protein biomarker targets (a) CRP (b)IL6, and (c) TNFα as a function of frequency [2.6].

This study shows the dielectric constants of various biomarkers as a function of frequency and concentration. The calculated detection range of this measurement scheme is in the range of 25 pg/ml to 25 ng/ml. This is a significant enhancement to the previous work as outlined in [2.7]. The authors further published the label-free capacitance based aptasensor platform in 2015, this time for the detection of HER2 cancer biomarkers [2.8]. HER2 is a biological protein that is shown to indicate instances of aggressive forms of breast cancer [2.9]. The capacitance response profiles of varying concentrations of the HER2 protein are shown in the figure below Figure 2.6.

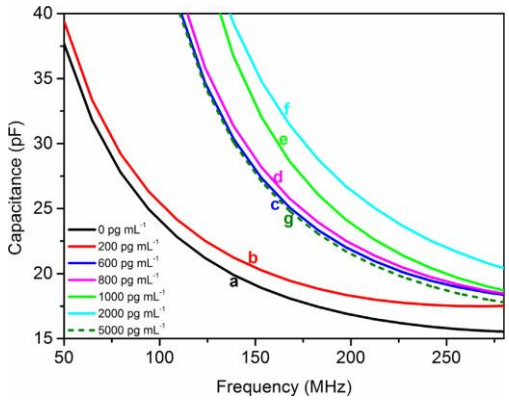

Figure 2.6 Capacitive response profiles showing HER2 protein dependant changes against frequency sweep from 50 to 300 MHz. [2.8]

The observed change in capacitance was found to be more stable at frequencies above 240 MHz. A linear increase of relative capacitance change was obtained at 242 MHz with dynamic concentraions from 200 pg/ml to 2 ng/ml of HER2 protein. The sensor in this case has a limitation at 2 ng/ml as well as at 5 ng/ml due to the abundance of molecules compared to limited binding sites on the sensor. Therefore the sensor must be fine-tuned by optimising the sensor are and geometry of the electrodes for obtaining the desired detection range.The authors presented a label free detection of multiple biomarkers for cardiovascular risk and breast cancer risk using interdigitated capacitor arrays immobilized with antibodies. Even though the system offers high sensitivity, there are still challenges to overcome. Inconsistences in batch fabrication of these sensors lead to variability in electrode specific area, which modifies the density of antibodies present and therefore the level of detection. As a result it is not advantageous to include assay type sensing.

2.2 Millimetre/Microwave Sensing

This section will look at the microwave frequency range. The devices in this section are split into two groups, the cavities and the coplanar devices. The advantages and disadvantages of each method are discussed below.

2.2.1 Microwave Cavity Perturbation

The cavity perturbation technique works on the principle of introducing a sample into a resonant cavity, and its complex permittivity or complex permeability are determined from the change in resonant frequency and quality factor of the cavity. Lin *et al.* [2.10] developed a microwave cavity perturbation technique for precision measurement of the complex permittivity and permeability of materials. The device consists of a rectangular waveguide with a non-radiating slot for insertion of the solid material under test as shown in Figure 2.7. In order to measure over a large frequency band, 4.5 GHz to 26.5 GHz, the measurements were taken using several standard waveguides, namely WR 187, WR 137, WR 90, WR 62 and WR 42 [2.11].

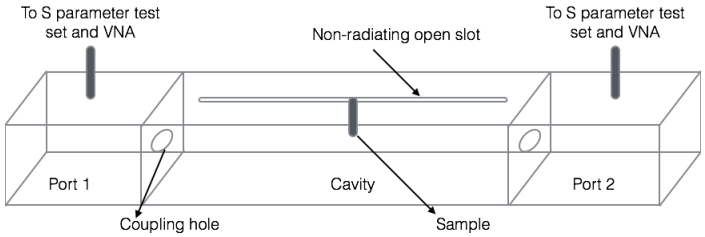

Figure 2.7 Rectangular waveguide measurement set-up showing the sample under test [2.10].

The measured results of the complex permittivity and permeability of various solid materials are shown below in Figure 2.8. The measurement results show that boron nitride and magnesium fluoride are both low loss dielectric materials. Boron nitride and magnesium fluoride have a real permittivity of around 4 and 5, respectively over the frequency range. The results for 99.9% pure Yttrium Iron garnet (YIG) show that it is a low loss ferrite material with a real permittivity of around 15, which is in good agreement with the manufacturers data. The measurements also illustrate that YIG has a natural magnetic resonant frequency at 5 GHz. These experiments demonstrate the accuracy of the cavity perturbation technique. They use solid samples, with reference to

manufacturers data they were able to show good agreement. This set-up, however, does not support fluid characterisation.

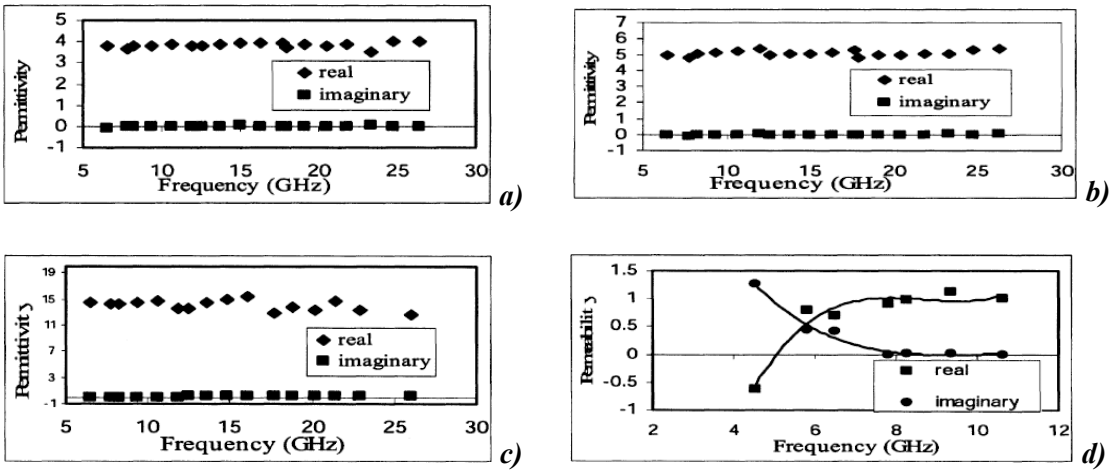

Figure 2.8 (a) Complex permittivity of boron nitride (b) Complex permittivity of magnesium fluoride (c) Complex permittivity of 99.9% pure YIG (d) Complex permeability of 99.9% YIG [2.10].

Jyh Sheen [2.12] developed an amended cavity perturbation technique to characterize ceramic samples. The measurement technique is shown below in Figure 2.9.

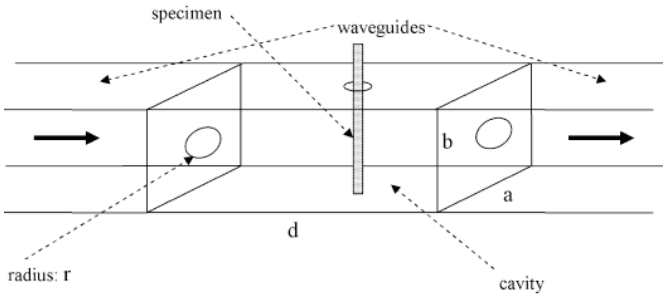

Figure 2.9 Amended cavity perturbation technique [2.12].

To verify the technique the results were compared to that of sampling using an X-band cavity of standard WR90 and using the post resonance technique as outlined in Figure 2.10.

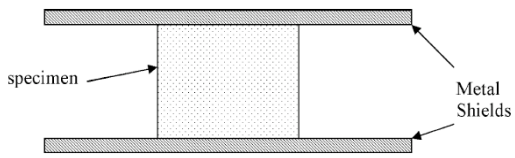

Figure 2.10 The post resonance technique [2.12].

The results are shown in the table below, Table 2.1. The results show that the technique is in good agreement with that of the post resonance technique for 2 ceramic samples. Again this technique is only capable of characterising solid materials.

Table 2.1 Comparison between the dielectric constant and loss tangent values of ceramic samples measured by the cavity perturbation technique at 10.16 GHz and post resonance technique [9]

Materials	Measurement Techniques	F_c (GHz)	ε'	tanδ
Sample #1	Conventional Method	10.16	18.5	0.00113
	Post Resonance	8.56	18.2	0.00104
Sample #2	Conventional Method	10.16	37.0	0.00150
	Post Resonance	9.36	37.2	0.00143

Nikawa and Guan [2.13] developed a measurement technique for obtaining the temperature dependent complex permittivity of a material by microwave heating using a cylindrical cavity resonator. The set-up includes a cylindrical resonator operating at 2.45 GHz and is fed with high power to induce microwave heating of the sample. A schematic and measurement set-up picture is shown in Figure 2.11.

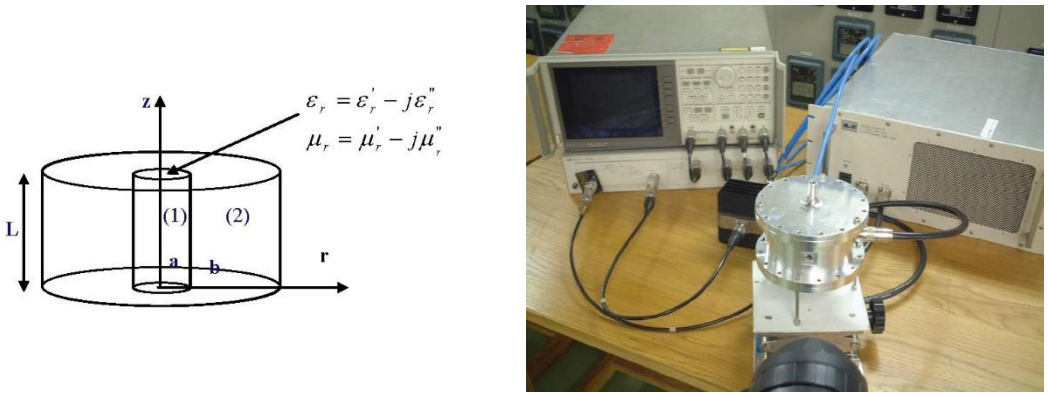

(a) ***(b)***

Figure 2.11(a) Schematic of cylindrical cavity resonator with location of the sample (b) experimental set-up [2.13].

The set-up also includes a cooling system to prevent the thermal expansion of the cavity and an infrared thermometer is used to measure the surface temperature of the test material. The samples tested using this system were alumina particles of 99.9% and 99.5% purity and, PolyPhenylene Sulphide (PPS), Polyether Ether Ketone (PEEK) and Polyamide Imide (PAI) as shown below.

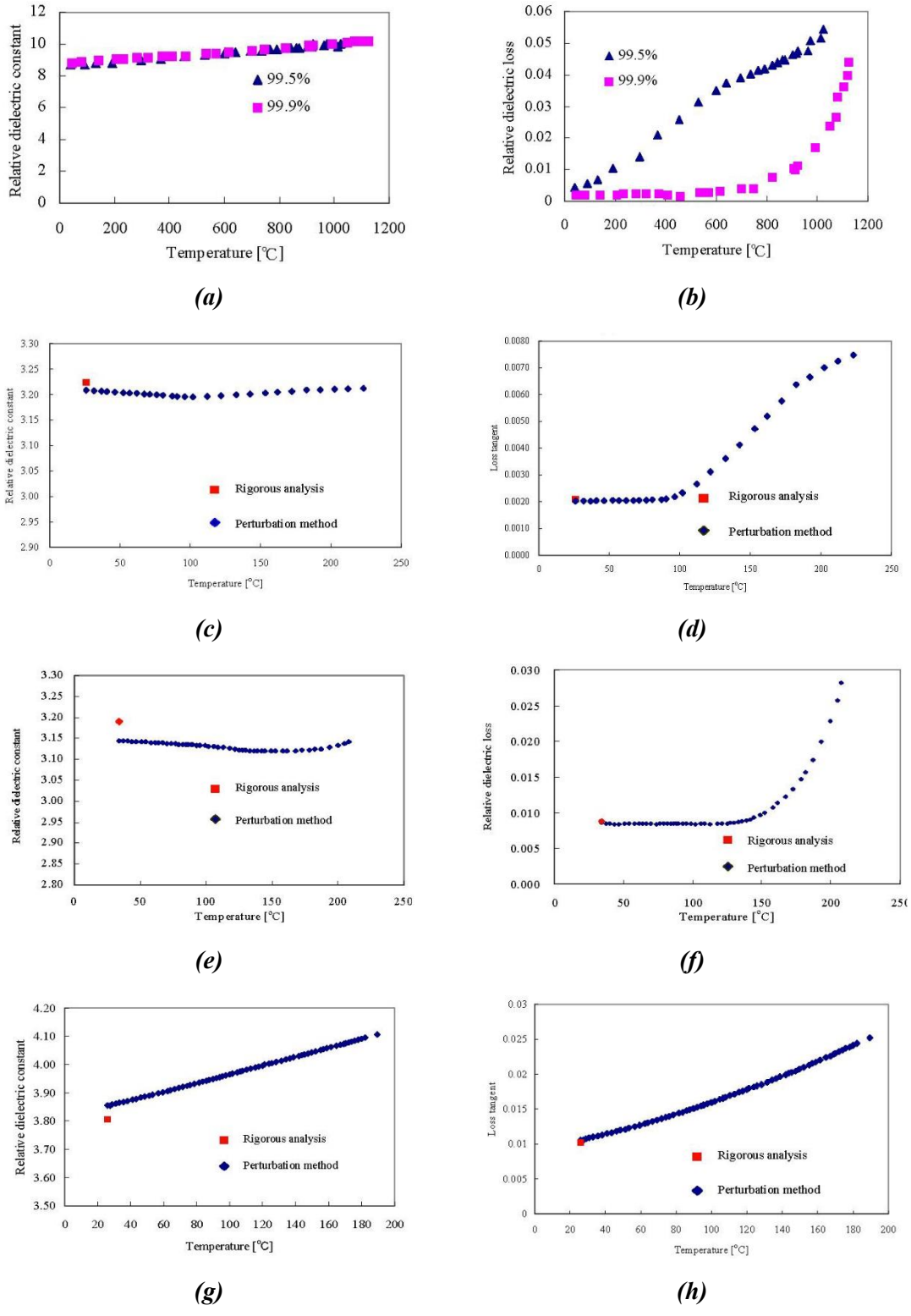

Figure 2.12 Complex permittivity and dielectric loss of (a)(b) Alumina, (c)(d)PPS, (e)(f)PEEK, (g)(h)PAI [2.13].

The relative dielectric constant of alumina increases slightly as the temperature increases. For the 99.9% pure alumina, the relative dielectric loss dramatically increases above 800°C. This dramatic increase in loss as the temperature increases is due to the material entering the glass transition mode. The same can be seen for PPS and PEEK, when the glass transition temperature for these materials is reached. For the amorphous organic material PAI, the relative dielectric constant and the loss tangent increased linearly with increasing temperature. Using a cavity perturbation technique they were able to extract the dielectric properties of some materials over a temperature range. However the samples were solid and the device did not incorporate fluid sampling. Also the device operated at a relatively low frequency making it less sensitive than other higher frequency devices.

A cylindrical cavity technique was also used by Kawabata *et al.* [2.14] to accurately measure the complex permittivity of liquids. The device consists of a copper cylindrical cavity operating at a resonant frequency of 1,967.331 MHz. The complex permittivity of liquids was measured using a rigorous analysis where the effects of sample insertion holes, a dielectric tube, and airgap between a dielectric tube and sample insertion holes are taken into account [2.15]. The liquid samples are inserted into the cavity using a dielectric PTFE tube located in the centre of the cavity shown in the schematic below, Figure 2.13.

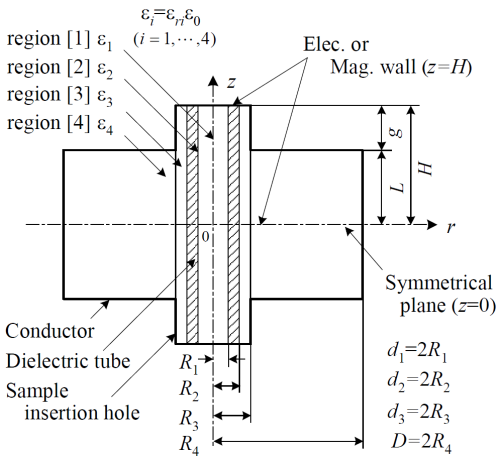

Figure 2.13 Schematic of the TM_{0mp} mode cylindrical cavity with a dielectric tube [2.14]

The measured frequency responses of the cavity are show in Figure 2.14.

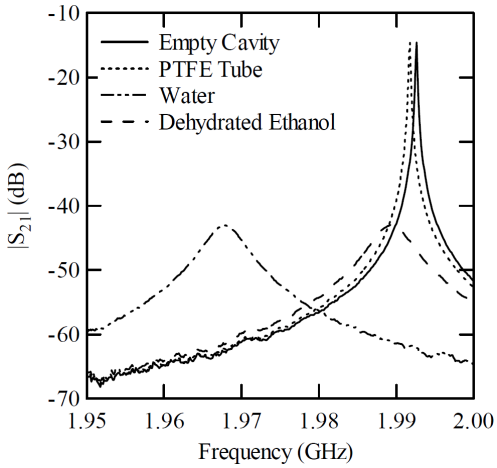

Figure 2.14 Frequency responses of the cavity with liquid samples [2.14].

Measurements were then carried out on the percentage of ethanol in water. The resonant frequency and unloaded Q were shown to increase proportionally with the increase in ethanol. The complex permittivity of the ethanol-water mixtures were then obtained from these measured values and are shown in Figure 2.15.

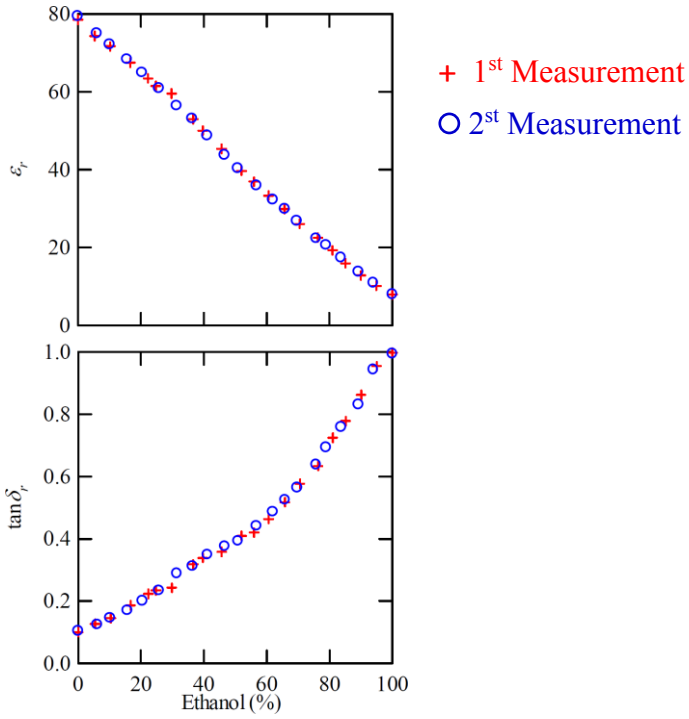

Figure 2.15 Variation of ε_r and $\tan\delta_r$ as a function of ethanol percentage [2.14].

A shown the dielectric loss increases linearly with increasing ethanol percentage. The measurements were also carried out on milk with different fat percentages and the results are shown in Figure 2.16. The values of complex permittivity ε_r decrease and the values

of dielectric loss tanδ_r increase with increasing fat percentage. This method verified the cavity perturbation method, incorporating a dielectric tube for liquid sampling. However as with other techniques this is operating at a lower frequency resulting in reduced sensitivity.

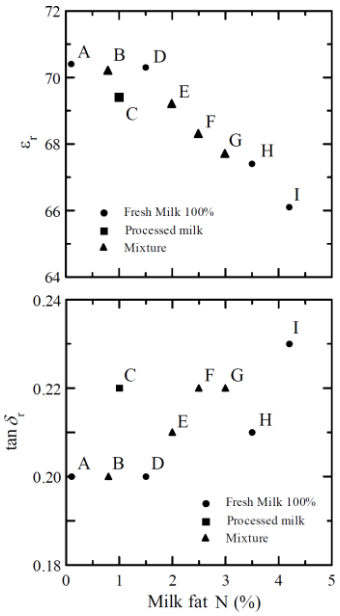

Figure 2.16 Variation of complex permittivity ε_r and dielectric loss tanδ_r as a function of milk fat percentage [2.14].

Saeed *et al.* [2.16] introduced a substrate integrated waveguide (SIW) cavity resonator for the complex permittivity characterization of materials. Fabrication of the device was carried out on an RT/Duroid 5880 substrate with a thickness of 2.8 mm. The walls of the cavity were metallised uniformly using deposition of a thin layer of silver epoxy. The capillary is made from borosilicate glass and is inserted into one of the sidewalls of the cavity as shown in Figure 2.17.

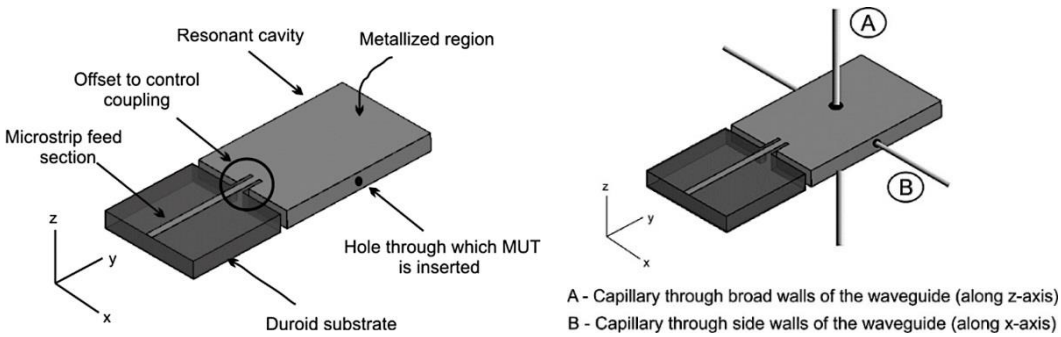

Figure 2.17 (a) Layout of substrate integrated waveguide cavity resonator (b) location of capillary inside the cavity [2.16].

The measurements were taken at room temperature with an Agilent PNA E8361A with the capillary in position B as indicated in Figure 2.17 (b). They measured various solvents including a study on dilute solutions of isobutanol and isopropanol; the results are shown below in Figure 2.18.

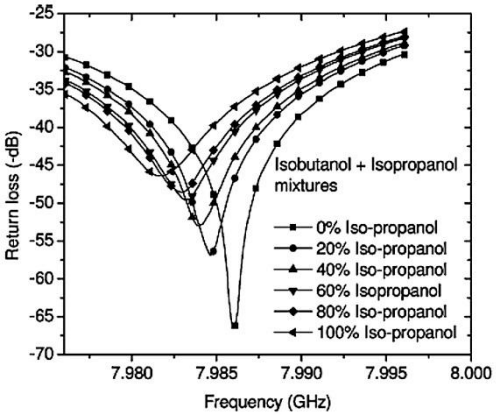

Figure 2.18 Return-loss performance of isobutanol and isopropanol mixture [2.16].

A comparison of their theoretical calculations and the measurements taken were presented in Figure 2.19, and show good agreement.

	ε_r'		
φ_f	Waveguide cavity	Mixture Theory	Substrate Integrated Waveguide Cavity
0	3.45 ± 0.04	3.454*	---
0.2	3.56 ± 0.02	3.557	3.579 ± 0.02
0.4	3.642 ± 0.03	3.657	3.667 ± 0.011
0.6	3.78 ± 0.023	3.76	3.755 ± 0.012
0.8	3.814 ± 0.02	3.864	3.856 ± 0.017
1	3.96 ± 0.04	3.968	---

	tan(δ)		
φ_r	Waveguide cavity	Mixture Theory	Substrate Integrated Waveguide Cavity
0	0.197 ± 0.002	0.1979*	---
0.2	0.22 ± 0.012	0.219	0.218 ± 0.021
0.4	0.236 ± 0.03	0.24	0.236 ± 0.011
0.6	0.26 ± 0.01	0.261	0.26 ± 0.015
0.8	0.28 ± 0.01	0.282	0.27 ± 0.01
1	0.3 ± 0.013	0.3026*	---

Figure 2.19 Comparison of measured and theoretical complex permittivity for isobutanol-isopropanol mixtures [2.16] *Values obtained from [2.17] and also measured with a waveguide resonant cavity

The device shows high sensitivity: for a change of dielectric constant of 0.5, there is a resonant frequency shift of almost 4.4 MHz. Furthermore for a loss tangent change of 0.1 there is a change of 2.9 MHz in the 3-dB bandwidth. The reported error for these measured results is within ±0.5%. This device offers high sensitivity and accuracy and the manufacturing technique is simple and cost-effective offering the possibility of an

integrated disposable sensor. However this technique only supports the characterisation of materials whose dielectric constant is of a median value e.g. solvents, as the system becomes insensitive to further changes in dielectric constant.

Another resonant cavity based technique is presented by Ferrier *et al.* [2.18], which also involves the use of microelectrodes that demonstrate the electro-manipulation and capacitive detection of biological cells within a microfluidic channel. The device consists of a high-Q quarter-wavelength cylindrical cavity resonator, a resistance/capacitance (R/C) circuit, microfluidic channel and an electrode pair as shown in Figure 2.20.

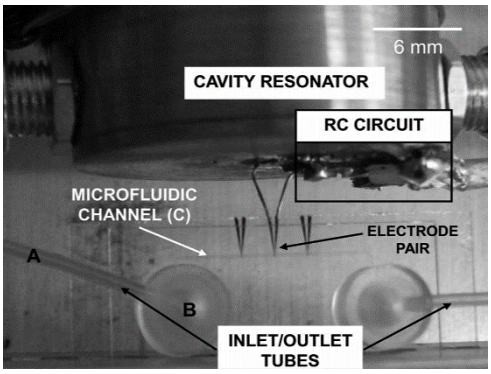

Figure 2.20 Experimental apparatus. Fluid and cells are delivered through PEEK tubing (a) into inlet connector (b) to the microfluidic channel (c) [2.18].

The microfluidic channel and electrodes are fabricated using standard lithography and etching techniques on glass. Measurements were carried out using 10 μm polystyrene spheres and 6 μm diameter yeast cells and the results are shown below in Figure 2.21.

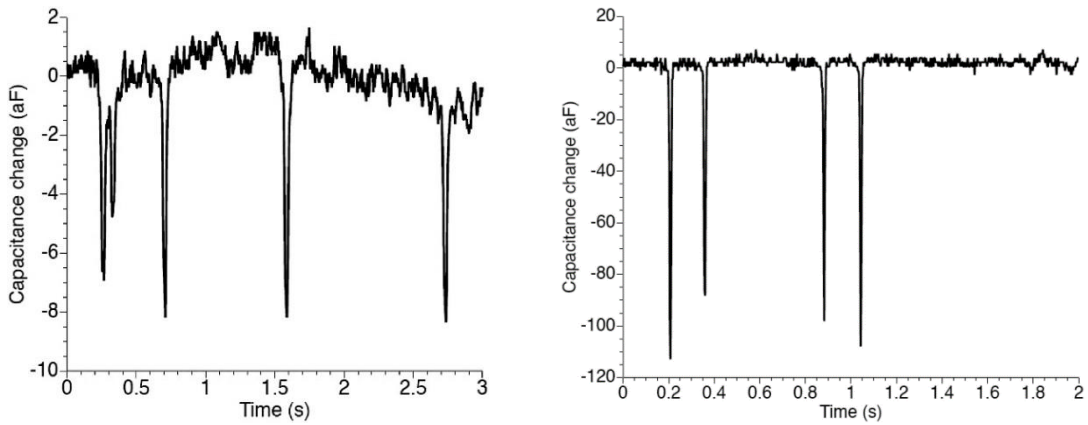

a) ***b)***

Figure 2.21 (a) yeast cells (b) polystyrene spheres [2.18].

As illustrated in both cases the presence of a bead or cell results in a decrease in capacitance due to the particles having a lower dielectric permittivity than that of water. There is a larger capacitance change observed from the polystyrene spheres as they are a larger particle and their dielectric constant has a higher contrast with that of water. Also, in both measurements, the capacitance differences between the same particle is due to them passing their passage at different heights above the electrode plane and size variations. Through a combination of electromanipulation and capacitive sensing they were able to distinguish and count particles in a microfluidic channel.

A recent study of complex permittivities through the use of a cavity perturbation has been studied by Lobato-Morales *et al.* [2.19] using substrate integrated waveguide (SIW) cavities. This technique is similar to the work of Saeed *et al.* discussed earlier. However instead of solid metallised walls, this design uses small metallic posts arranged so to enclose the electric field. The cavity is excited using a coaxial probe and the design is shown in Figure 2.22.

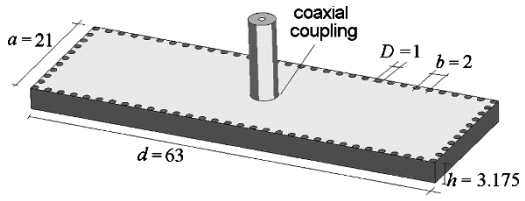

Figure 2.22 Layout of the SIW cavity 1. [2.19].

The cavity was fabricated on a Rogers RT/Duroid 5880 substrate with the lateral walls realised by metallic posts. The samples were inserted in a 2.4 mm hole at positions of maximum electric field and measured using an Agilent PNA series Vector Network Analyser (VNA) (E8362A). The results for various solid samples are shown in Figure 2.23.

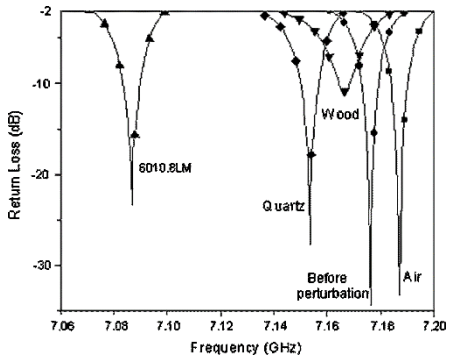

Figure 2.23 Experimental response of the cavity with various materials [2.19].

The sample labelled 6010.8LM is a type of Rogers RT/Duroid material. The higher the dielectric permittivity of the sample is, the lower the resonant frequency. Also, samples such as wood, which have higher losses, also exhibit a lowering of the Q-factor. Sample variations in permittivity constant of 0.5 and loss tangent of 0.01 were characterised with the designed SIW cavity. Although this device shows good sensitivity there is no integration of a system for delivering fluid samples as the previous devices.

2.2.2 Coplanar Devices

The Coplanar Waveguide (CPW) is a structure like that shown in Figure 2.24, where a conductor is separated from a pair of ground planes, all atop a dielectric substrate.

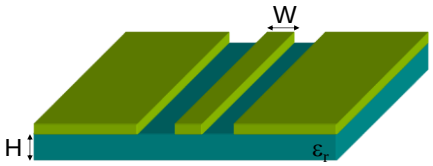

Figure 2.24 Basic coplanar waveguide structure.

Ideally the dielectric substrate is infinite however in practice the height, *H*, is chosen so that the field remains within the device and does not escape into free space. The advantage of using such a structure is in the fabrication, which uses standard photolithographic processes. Another advantage is that extremely high frequency responses can be achieved, as there are no parasitic discontinuities in the ground plane.

Grenier *et al.* [2.20] combined this coplanar waveguide design with a polydimethylsiloxane (PDMS) microfluidic channel for a high-frequency-based biosensor. The device is fabricated on a quartz substrate with the CPW transmission lines realised with a lift-off process of Chromium/Gold, Cr/Au. The microfluidic channel is fabricated in PDMS using soft lithography. This is then bonded to the metallised quartz substrate as shown in Figure 2.25.

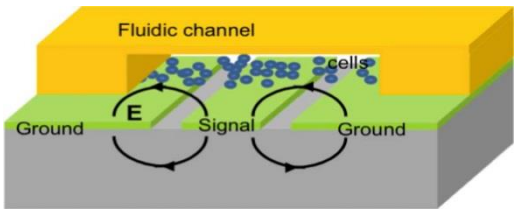

Figure 2.25 Schematic view of HF interaction between a CPW and a biological solution, which is localised in a microfluidic channel [2.20].

In order to validate their sensor capabilities and their proposed permittivity extraction method, principle standard liquids such as deionised (DI) water, solvents, and air have been successfully evaluated. The results are shown below in Figure 2.26.

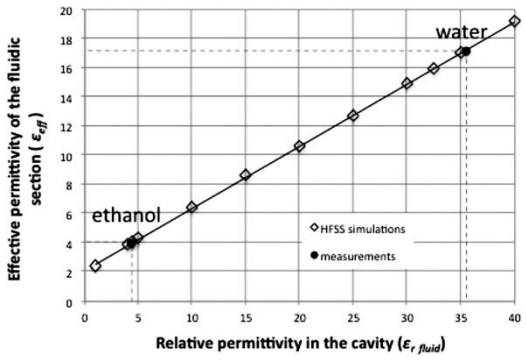

(a)

Fluid Type	Measured ε_{eff}	Extracted ε_{fluid}	Theoretical ε_{fluid}	% Error
Ethanol	3.94	4.34	4.2	3.0
DI Water	17.2	35.4	34.8	1.7

(b)

Figure 2.26 (a) Effective permittivity of the fluidic line portion as a function of relative permittivity of the material, which is localized in the cavity (b) Results for Ethanol and DI water at 25GHz [2.20].

The extracted permittivities are in good agreement with that reported in literature [2.21] and, in both cases, the error is equal to or less than 3%. The varying temperature during measurement may cause discrepancies in their results. Once validation was complete they then presented results for the characterisation of the Human Umbilical Vein Endothelial Cell (HUVEC) characterisation. The results for the cell suspension and the biological medium in which the cells were suspended are given in Figure 2.27.

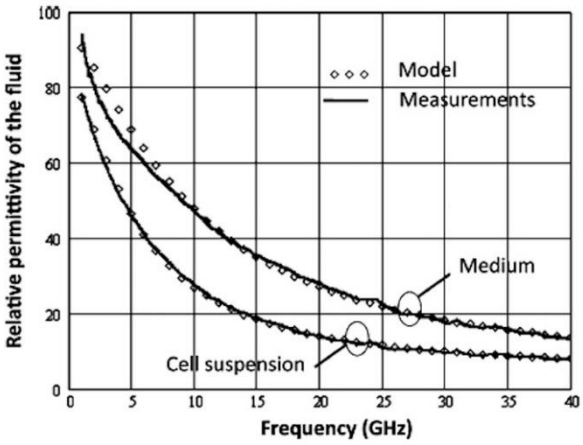

Figure 2.27 Relative permittivity extracted from measurements and Cole-Cole modelling for the (100%) cell suspension and the biological medium [2.20].

As observed there is good agreement with the model and the measured data obtained for both the HUVEC suspension and biological medium. There is a noticeable shift in the permittivity of the cells compared to that of the biological medium. This can be explained due to the cells containing more water and hence a lower relative permittivity than the biological solution itself. This also describes the relaxation phenomenon as the frequency increases as more absorption occurs at higher frequencies. In order to test the sensitivity of such a device Grenier *et al*. measured various concentrations of cells as shown in Figure 2.28.

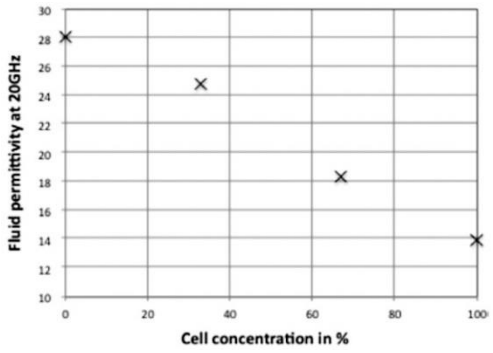

Figure 2.28 Impact of the cell concentration on the detected effective relative permittivity of the fluid [2.20].

In addition to the 100% cell suspension and 0%, where only biological solution is present, measurements were taken at 33% cell concentration and 67% concentration at a frequency of 20 GHz. As the cell concentration increases there is a clear decrease in the relative permittivity of the media. The difference in the relative permittivities is large and therefore allows the device to be used for quantitative analysis of biological media. The minimum cell concentration was calculated to be 35 x 10^6 cells/ml.

Another coplanar device was also created by Greniers team, W. Chen, D. Dubuc and K.Grenier produced a microwave sensor dedicated to the dielectric spectroscopy of single particles [2.22]. The coplanar waveguide is realised on a quartz substrate with gold deposition for the RF structure. The microfluidic channel is placed over the waveguide structure and a trap is constructed to guide a single particle into the high electromagnetic field region as shown in the figure below, Figure 2.29.

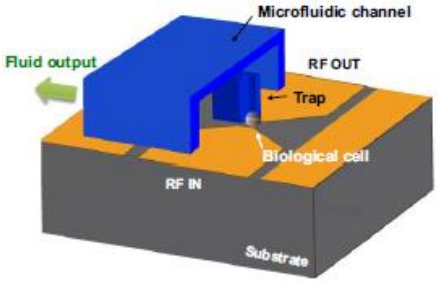

Figure 2.29 3D schematic of the microwave-based sensor for single particle dielectric analysis. [2.22]

Measurements were carried out on a single living biological cell in suspension, C_{cell}. The S parameters were measured for the suspension alone, C_{medium}, and the corresponding capacitive contrast is calculated using the equation below, Equation (2.1).

$$\Delta C = C_{cell} - C_{medium} \qquad \textbf{(2.1)}$$

The capacitive contrast spectrum over 40 GHz is shown in the graph, Figure 2.30.

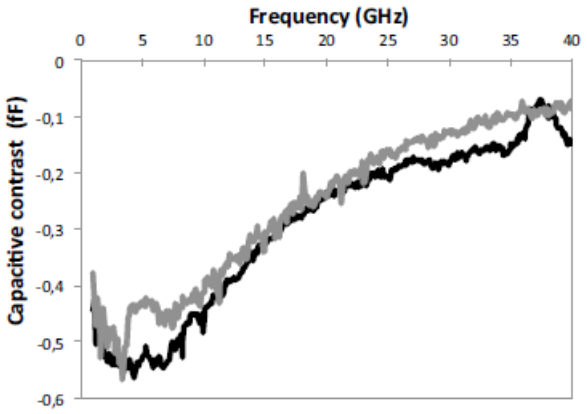

Figure 2.30 Capacitive contrast of living single cells trapped in the sensor. [2.22]

The results show two different spectra of two single cell measurements. The differences in the spectra are attributed to the intrinsic cell differences and cell cycle. The repeatability of the sensor is unclear given the nature of biological cells. However if different media could be tested this device could exhibit interesting results with better repeatability.

Y.-F. Chen *et al.* also developed a similar CPW biosensor for cancer cell dielectric characterisation [2.23]. The device was fabricated on a quartz substrate with titanium gold coplanar waveguide as shown in the graphic below Figure 2.31.

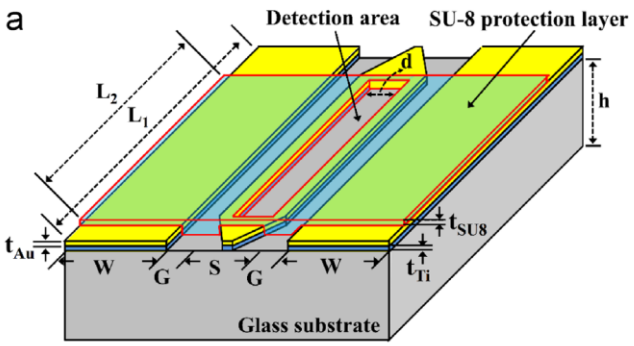

Figure 2.31 Illustration of the fabricated device. [2.23]

The results were obtained by using an Agilent N5247 on-wafer Vector Network Analyser (VNA). The results for varying cell concentrations placed into the detection area over 0 to 40 GHz are shown below in Figure 2.32.

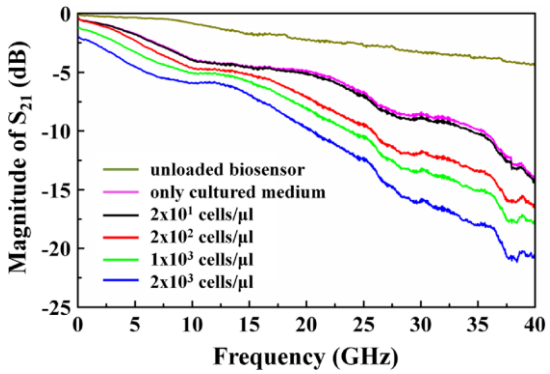

Figure 2.32 S_{21} – magnitude measurements of different cell densities placed in the sensor. [2.23]

The results demonstrate the ability to distinguish between varying cell concentrations down to 20 cell/µl. The degradation of the S_{21}-magnitude at different cell densities is attributed to the polarization effects, including ion vibration and deformation losses between the cells at microwave frequencies. The sensor offers a label-free dielectric characterisation method for biological cells up to 40 GHz. Although the system offers micro-litre volume detection, the sensor does not incorporate a microfluidic channel system. This would make it easier to integrate it with other detection systems.

Another CPW with microfluidic channel device for measuring permittivity was demonstrated by Mateu *et al.* [2.24] [2.25]. The technique contains a polydimethylsiloxane (PDMS) substrate with CPW transmission lines integrated with a microfluidic channel. A schematic of the device structure and the actual manufactured device is shown below in Figure 2.33.

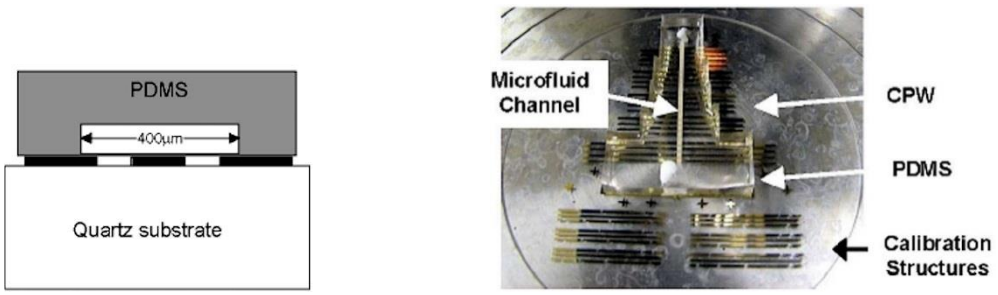

(a) ***(b)***

Figure 2.33 Integrated microelectronic/microfluidic test structures. (a) Cross-section schematic; solid black represents the gold conductors; grey the PDMS; (b) Fabricated measurement platform [2.25].

The structure was fabricated on a quartz substrate using standard photolithography techniques to pattern 0.4 μm thick metallic Titanium/Gold, Ti/Au, coplanar waveguide transmission lines and interdigitated capacitors. The microfluidic channel is formed using a cast moulding technique that uses a Silicon wafer template with 25 μm thick features of photoresist. The PDMS is then applied to the Si/photoresist mould and cured. This then forms the microfluidic channel that is then bonded to the test wafer with the meandering microfluidic channel aligned directly over the metallic electrodes of the transmission lines or capacitors, as shown in Figure 2.34.

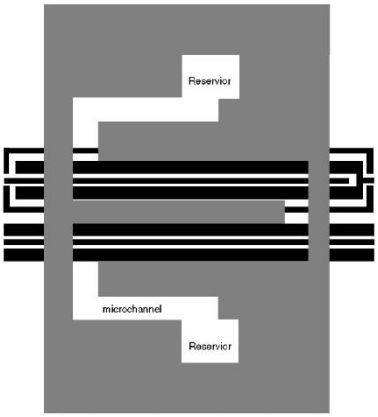

Figure 2.34 Schematic of the transmission line and the capacitors in black aligned with the microchannel cast in PDMS shown in grey [2.25].

In order to carry out measurements, the lumped-element series-capacitor structures at lower frequencies less than 100 MHz, and distributed transmission line structures at higher frequencies need to be measured. Once the capacitance and conductance per unit length of the two different structures are measured, using an additional analysis step the relative permittivity can be calculated as a continuous function of frequency. The measured results for both deionized water and methanol of the real and imaginary parts of the extracted relative permittivity in the frequency range of 100 Hz to 40 GHz are shown in Figure 2.35.

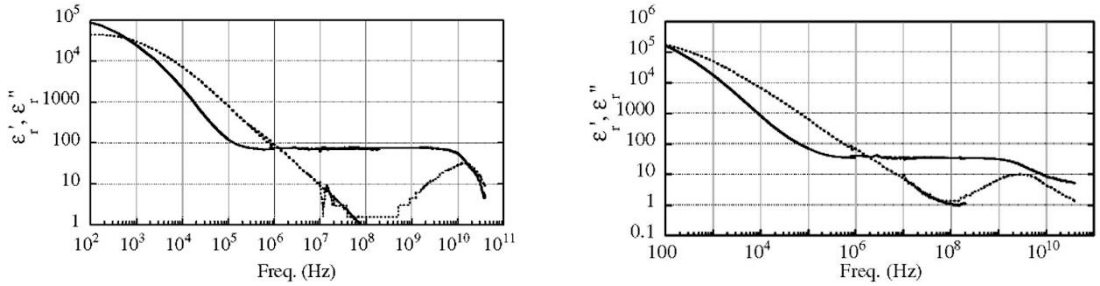

(a) *(b)*

Figure 2.35 Real (solid line) and imaginary (dotted line) relative permittivity of (a) deionized water (b) methanol [2.25].

There is a region of frequency independent permittivity values, which are both consistent with water and methanol at room temperature. However an anomaly occurs in both measurements at low frequencies where the extracted permittivity dramatically increases. This is thought to be due to the electrode polarization effects as described by Schwan [2.26], which adds an extra capacitance in series with the fluid capacitance and conductance. To analyse the accuracy of the device in determining the relative permittivity, the high frequency results of the methanol measurements are compared to that of permittivity measurements of the bulk methanol samples at 20°C using an open-circuit measurement fixture.

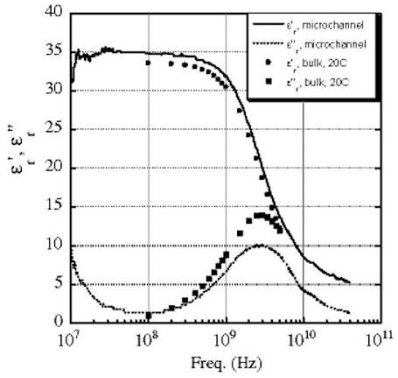

Figure 2.36 Relative permittivity measurements at high frequencies of methanol at room temperature (lines) and measurement on bulk samples at 20°C (symbols) [2.25].

The error in the measurement analysis is calculated to be less than 10%; this discrepancy could be due to the non-control over the temperature in the measurement structure. In 2007 Mateu *et al.* [2.25] expanded the system analysis and included results, Figure 2.37,

of the permittivity of an aqueous solution containing 10% polystyrene latex beads as well as comparing results from different CPW line sizes.

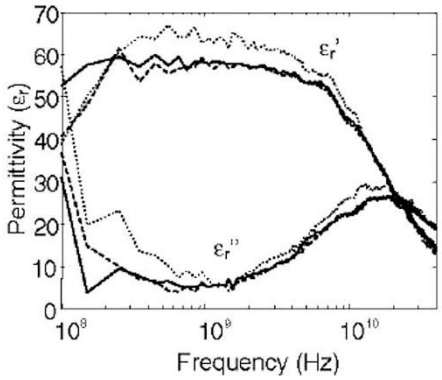

Figure 2.37 Real and imaginary parts of the permittivity of an aqueous solution containing 10% polystyrene latex beads. Solid, dashed and dotted lines corresponds respectively to measurements from lines with 10µm, 20µm and 50µm gap. [2.25]

As the results show there is good consistency between each of the geometries with an error less than ±5%. Since the 50 µm geometry gap structure is more sensitive to measurement errors due to the small values for the capacitance per unit length, this is where the biggest deviation occurs. Although able to determine the permittivity of various substances up to 40 GHz this device needs more work on the repeatability and accuracy if this is to be applied to the medical field.

The Finite Ground Coplanar Waveguide (FG-CPW) is similar to that of the CPW but with a ground plane formed on the opposite side of the dielectric as shown in Figure 2.38. This has the advantage of, among others, to prevent spurious resonances from occurring.

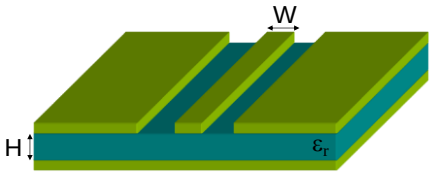

Figure 2.38 Finite Ground Coplanar Waveguide (FG-CPW).

Sanghyun *et al. 2008* [2.27] presented a FG-CPW device for the complex permittivity measurements of liquids and living cell suspensions in a SU-8 reservoir. The FG-CPW was fabricated on a Pyrex 7740 glass wafer substrate 550 µm thick using standard

photolithography and electroplating techniques. The finite-width ground plane was fabricated using gold. In order to measure the liquids and living cell suspensions a SU-8 well was fabricated with walls 300 μm high to ensure that most of the EM field is confined inside this structure.

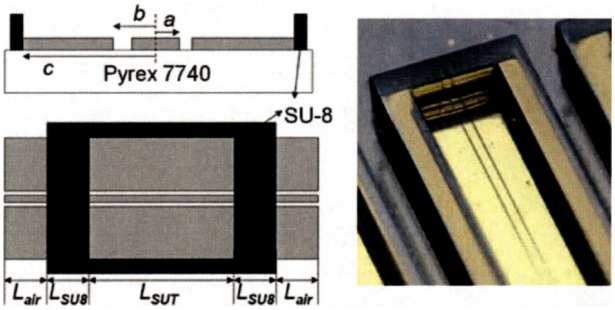

Figure 2.39 Schematic and image of the fabricated CPW test structure with SU-8 reservoir [2.27].

Using microwave probes and an Anritsu 37397C Vector Network Analyser (VNA) they were able to perform permittivity measurements of methanol and isopropanol up to 32 GHz as shown in Figure 2.40.

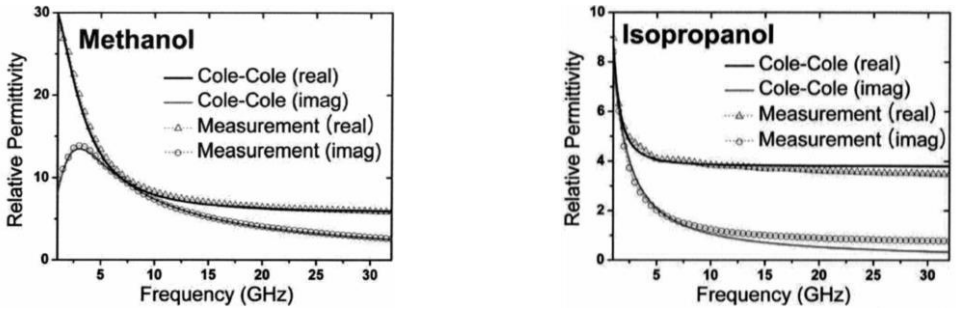

(a) ***(b)***

Figure 2.40 Measured complex permittivity of (a) Methanol and (b)i Isopropanol by CPW sensors [2.27].

In order to verify their method they compared their results with that obtained from the Cole-Cole equation of [2.28]. The measurements taken agree well with other reported results. Sanghyun *et al.* also performed measurements on living cell suspensions, namely cells of the Human Embryonic Kidney cell-line (HEK-293). They examined the effect

that dimethylsulfoxide (DMSO) has on the permittivity. Results in Figure 2.41, show the measurements taken over 30min for a treatment of 10% of DMSO.

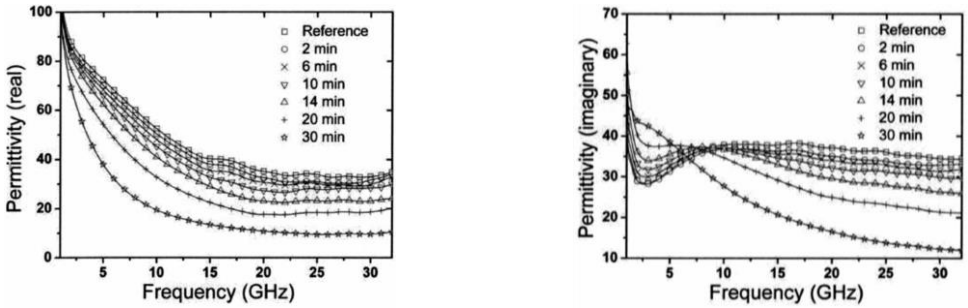

(a) *(b)*

Figure 2.41 Measured complex permittivity over time for 10% dimethylsulfoxide (DMSO) treated HEK-293 cells; (a) real and (b) imaginary [2.27]

There is an asymptotic decrease of the permittivity with frequency leading to more steady state values. The overall trend is towards similar characteristics as observed in the dielectric relaxation of water. This can be attributed to the DMSO interacting with the cell membrane causing water pores and promoting the diffusing of the salt suspension solution.

In order to limit the frequency in coplanar waveguide sensors a planar resonant structure can be incorporated, which allows a narrow band characterisation becoming more sensitive to small parameter changes. Dalmay *et al.* [2.29] used this technique to develop a label-free biosensor. Their device consists of a fused silica substrate with a fabricated band stop resistor-inductor-capacitor (RLC) resonator fed by a CPW line for on wafer RF measurements. The device design is shown in Figure 2.42.

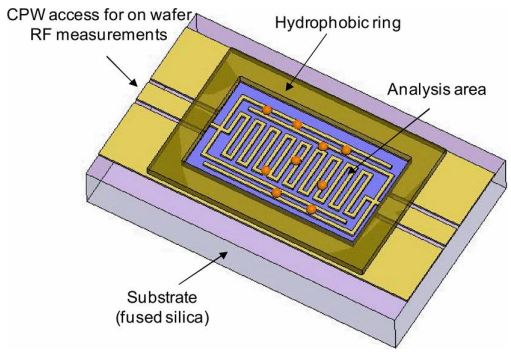

Figure 2.42 Design view of the proposed micro biosensor [2.29].

The resonator is fabricated with meandered gold metallic lines to form the inductor, which is coupled to an inter-digital capacitor. The electromagnetic field distribution is shown in Figure 2.43, which shows that the field is highest in the inductive area allowing sensitive detection.

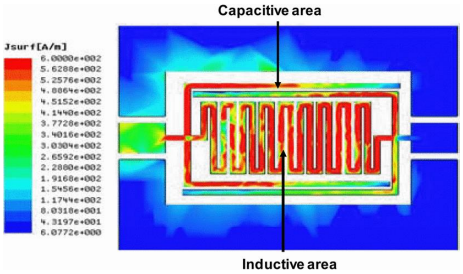

Figure 2.43 Surface current distribution plot at the resonant frequency [2.29].

With no microfluidic network integrated with this sensor the cells are prepared in a dried ficoll solution. Using a paraformaldehyde (PFA 4%) fixative solution the cells are kept intact and have the same electrical properties as in living conditions but are in fact no longer alive. The cells are then washed, dried and suspended in a biological support media. The solution is then deposited on a 20 µm thick SU-8 layer atop the resonator structure. S-parameter RF measurements, Figure 2.44, are performed on human karatinocytes HaCaT cells (skin cells) and glial-cells-derived tumour glioblastoma (nervous system astrocyte cells).

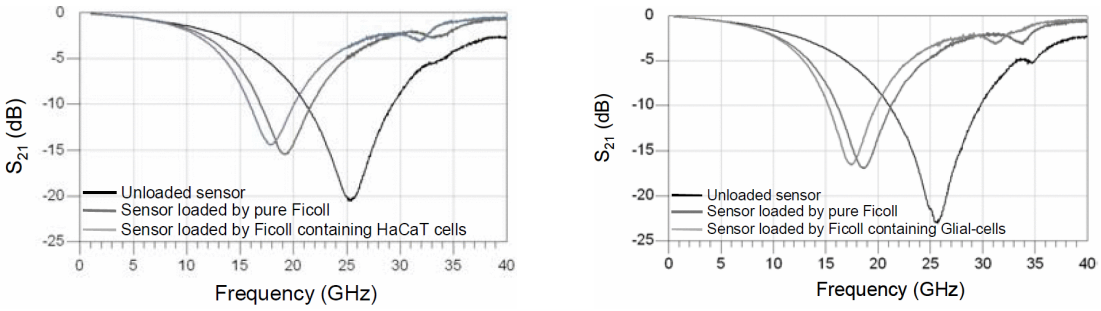

(a) ***(b)***

Figure 2.44 Measured biosensor frequency shift in (a) HaCaT and (b) Glial-cells embedded in ficoll matrix [2.29].

In observation of the results there is a clear frequency shift compared to the pure ficoll of 1.3 GHz for HaCaT cells and 1.18 GHz for the Glial cells. With the frequency shift directly relating to the number and position of the cells it is difficult for obtaining repeatability and simulation data without a high error margin. For diagnostic applications this system would have to integrate a microfluidic chip in order to preserve the cells under test. This is vital as for rapid characterization the less preparation is needed the quicker the diagnosis.

Further to this work Dalmay and collegues created a similar device for dielectric spectroscopy of liquid medium [2.30]. The device consists of a RF planar capacitive electrodes with a microfluidic channel defined using SU8 photoresist and PDMS as outlined in the graphic below, Figure 2.45.

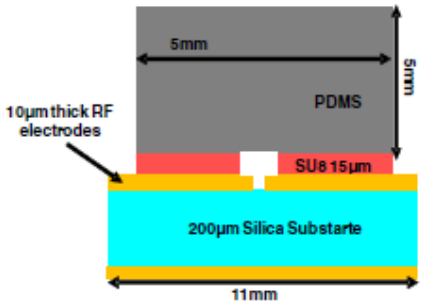

Figure 2.45 Cross sectional view of the fabricated sensor

The device was then characterised using water/ethanol mixtures over a frequency range of 0 Hz to 8 GHz. The results are shown in the figure below. Figure 2.46.

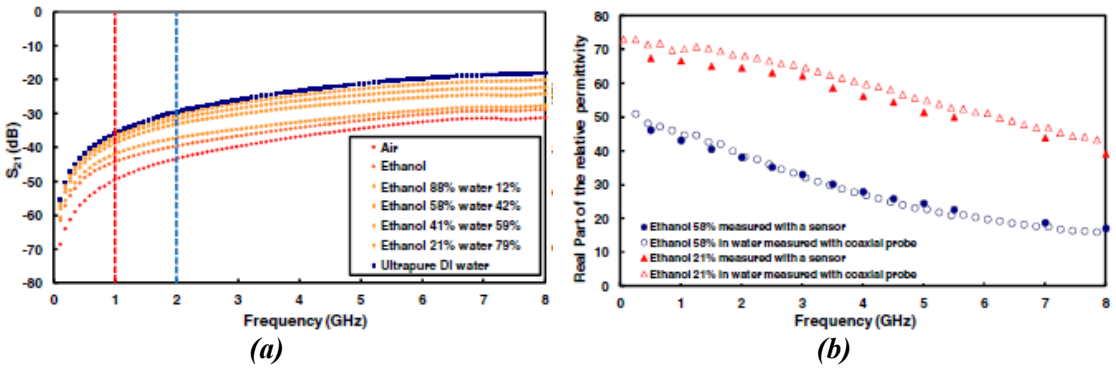

(a) *(b)*

Figure 2.46 (a) Normalised transmitted RF signal through sensor for difference ethanol/water mixtures. (b) Comparison of the real part of the permittivity versus frequency obtained with an Agilient 85070 probe kit (empty symbols) and the microfluidic sensor (dark symbols)

Figure 2.46(a) shows that the normalised transmitted RF signal increases with frequency over the 8 GHz range. There is also a clear distinction between the various ethanol and water mixtures. Figure 2.46(b) examines the difference in the real part of the permittivity as measured by the sensor and that measured with an Agilent 85070 probe. The results show good agreement with the proven technology. This is another example of a spectroscopy technique where the medium is measured over a given frequency range. The devices use as a sensor is however limited by this as there are no narrowband frequency features making it more difficult to discriminate between substances.

Another planar device is presented by Yun and Lim [2.31], as a Complementary Split Ring Resonator (CSRR) in a Substrate Integrated Waveguide (SIW). The sensors offers a high-Q allowing high resolution and sensitivity. The device is fabricated using Rogers Duroid 6010, a copper clad ceramic-PTFE composite substrate. The design of the sensor device is shown below in Figure 2.47.

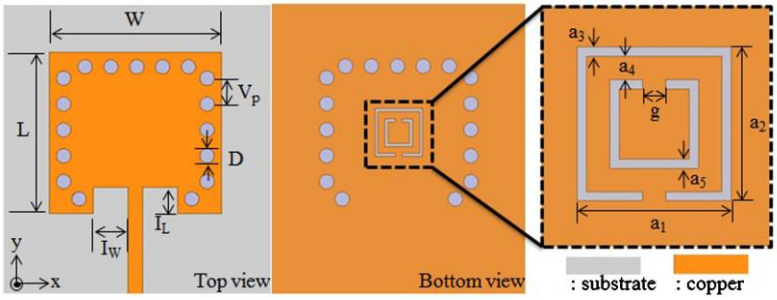

Figure 2.47 Planar views of the CSRR-loaded SIW with a detail of the split ring resonator. [2.31]

This sensor was used to detect cracks in aluminium samples. The results from the measurements are compared to simulations carried out in Ansys High Frequency Structure Simulator (HFSS) software. The results are shown below in Figure 2.48.

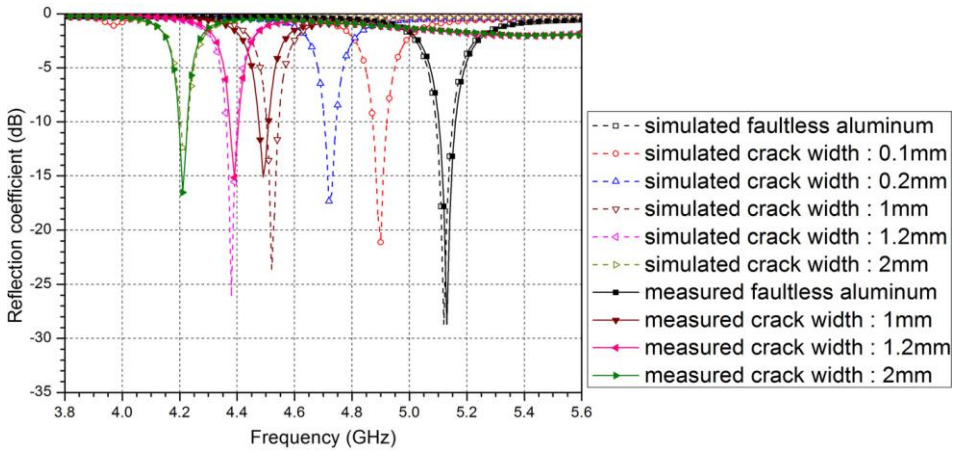

Figure 2.48 Simulated and measured results of the reflection coefficient for a crack depth of 1 mm. [2.31]

The results show excellent agreement with the simulations, however the sensor is very application specific. There were no trials with liquid media and did not incorporate a delivery method for liquids for this type of media testing.

2.3 Terahertz (THz) Frequency Sensing

The advantage of Terahertz radiation is that it is non-ionizing. It is high frequency therefore has the potential for high sensitivity and can also penetrate many dielectrics making it useful for non-invasive imaging techniques. The disadvantages of this frequency range is the high absorption of water molecules which can limit detection, also sources and detectors at this frequency are limited and are generally of low power. This obviously limits the type of materials and the volume of material that can be detected. Various techniques that have made use of the advantages of this frequency are presented.

A Goubau line or G-line is a type of single wire transmission line fabricated from a conductor coated in a dielectric typically used at Ultra High Frequencies (UHF) and microwave frequencies. Treizebre *et al.,* [2.32] developed a Terahertz Biological-Micro-Electro-Mechanical system (THz BioMEMS) for the study of cellular informative transfer based on a CPW to Goubau line transition. The device shown in Figure 2.49, is fabricated in two parts. The first part consists of the microfluidic channels and the THz transmission line constitutes the second part.

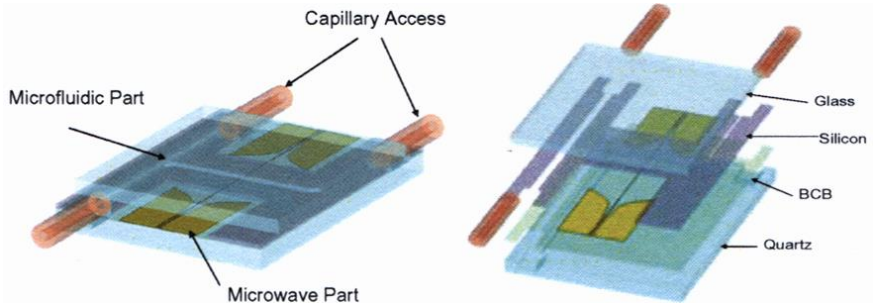

Figure 2.49 THz BioMEMS device [2.32].

The first part is fabricated in silicon using standard deposition, photolithography and etching techniques. Firstly a silicon nitride (SiN) layer is deposited forming a hard mask for the photolithography patterning steps. The SiN is etched followed by a silicon Reactive Ion Etch (RIE) to form the microchannels. The second part is fabricated on a quartz substrate that is deposited with titanium (50 nm) and a sputtering of gold (450 nm). Standard photolithography and RIE etch is then performed defining the THz waveguide. The two parts are then bonded using a layer of Benzocyclobutane (BCB), which forms closed microchannels under the transmission line of the sensor. The measurements for this paper are from experiments performed on different concentrations of lactoferrin solution in Phosphate Buffer Saline (PBS). The results are shown below in Figure 2.50.

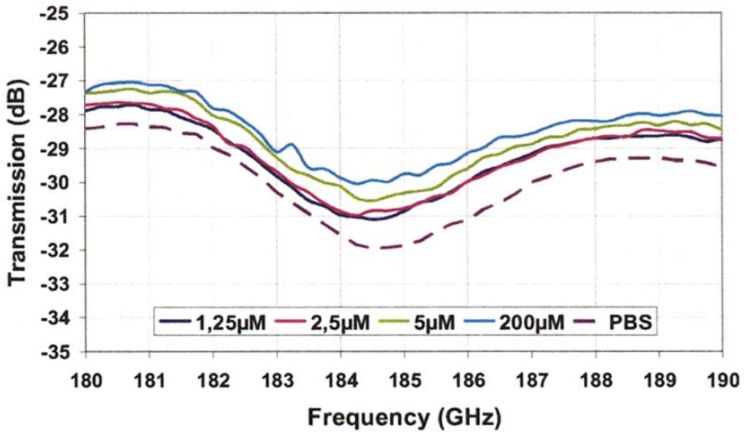

Figure 2.50 Experimental results obtained on different lactoferrin solution in PBS [2.32].

The dashed line shows a pure solution of PBS only; the others show varying concentrations, some at very low concentration values, of lactoferrin solution in PBS. The higher the concentration of lactoferrin the lower the losses; this can be explained by the replacement of water molecules with that of lactoferrin ones. The water molecules have

a higher absorption rate compared to the lactoferrin at this frequency. From these initial experiments, they have developed a cold plasma functionalised Terahertz BioMEMS for enzyme analysis [2.33], shown in Figure 2.51. The device fabrication is as before but with an additional 50nm plasma polymerised allylamine (ppAA) layer formed in a plasma reactor. Tripsin, a proteolytic enzyme, is immobilized onto the microchannel for the enzyme analysis once the device is bonded and connected to an inlet/outlet capillary system.

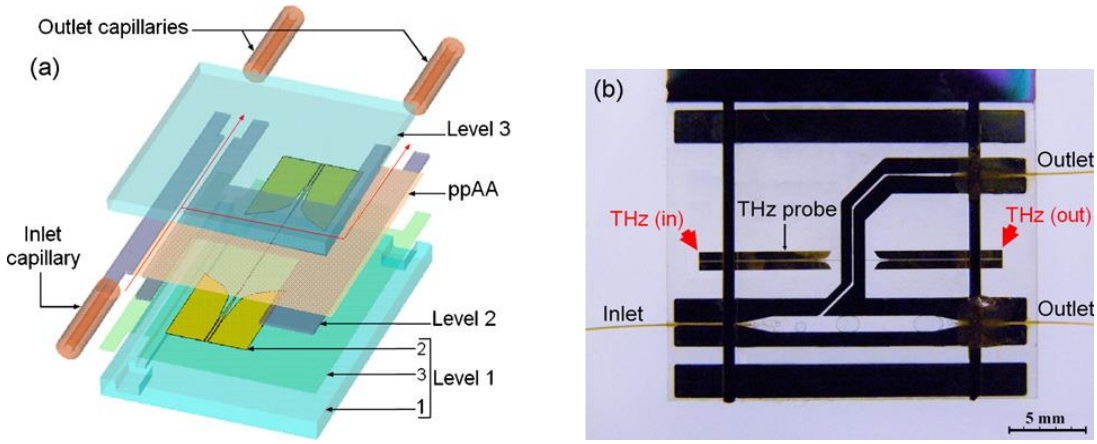

Figure 2.51 (a) Level 1: quartz substrate (1) supporting gold THz waveguide (2) this level is coated with BCB (3) to allow bonding of microfluidic circuit etched on silicon substrate (level 2) The obtained structure (levels 1+2) is exposed to plasma polymerization of allylamine (ppAA) before being covered by a glass substrate (level 3). (b) Overview photography of the THz BioMEMS. Red arrows show position of VNA tips [2.33].

As before the THz waveguide is connected to an 8510XF Agilent Technologies VNA and transmission spectra were measured over the range of 60 GHz to 110 GHz. The first tests were performed on the device before and after ppAA deposition and prior to and after trypsin immobilization.

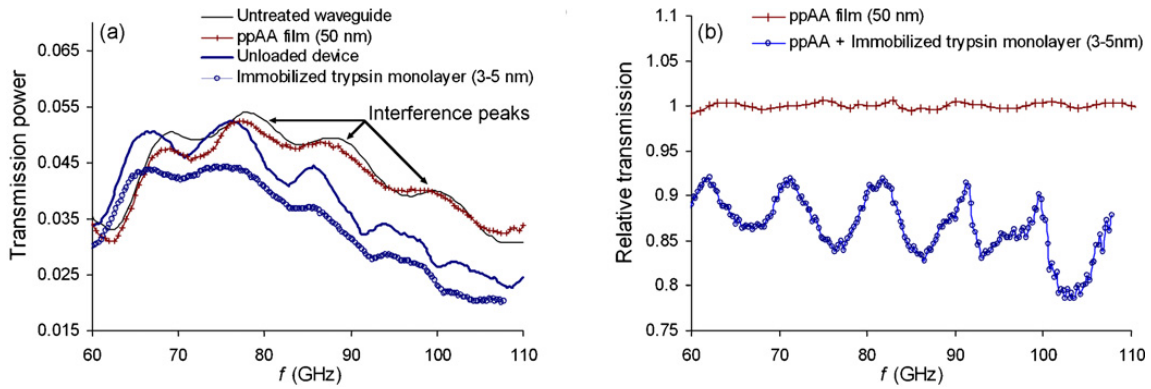

Figure 2.52 (a) Raw data for the transmission of the waveguide prior and after ppAA deposition, and the transmission of the BioMEMS before and after trypsin immobilization. (b) Normalized spectra for ppAA and trypsin monolayer using the untreated waveguide and the unloaded device respectively [2.33].

As shown in Figure 2.52(a), there are peaks at approximately 10 GHz apart, marked by the arrows; these are caused by standing wave effects. Notably the deposited 50 nm ppAA layer shows a flat, structure-less transmission spectrum and reveals that ppAA film is a highly transparent material with a very low reflection and low absorption in the spectral range of interest. In contrast, the immobilised trypsin causes the amplitude of the interference peaks to shift and decrease in the transmission data. The biomolecules exhibit absorption due to low-frequency molecular internal motions involving primarily the internal hydrogen bonds, which cause this type of transmission from trypsin. To further test their device various aqueous media were measured again in the frequency range 60-110 GHz. The results are show in Figure 2.53 below.

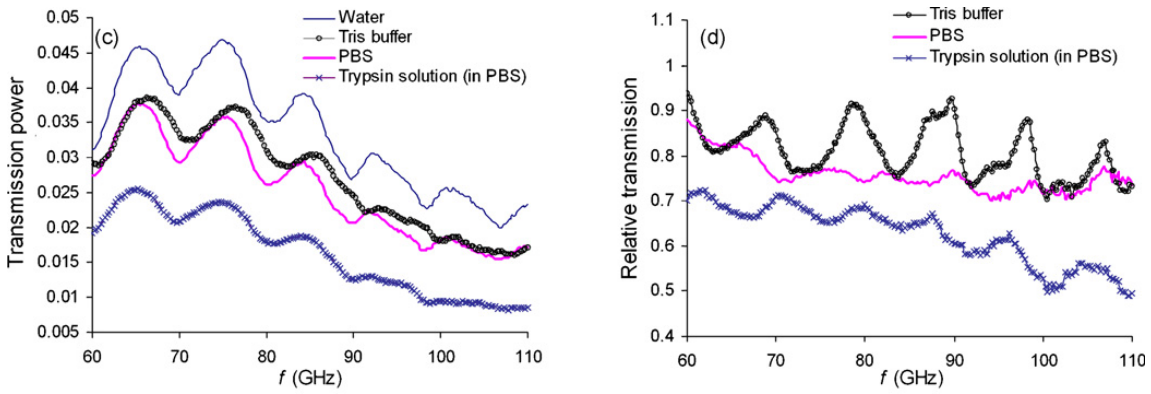

Figure 2.53 (a) Raw spectra for different aqueous media. (b) Normalized data were realized with respect to deionised water (for buffers) and Tris buffer (for trypsin solution) [2.33].

Tris buffer has more of an effect on the transmission that PBS. PBS contains no dipole structures whereas in Tris buffer orientational relaxations in the dipole moments of Tris and HCl molecules cause more distortions. Also, the concentration of Tris buffer was higher than that of PBS contributing additionally to the observed changes. In the Trypsin solution results, we can see a lower transmission with respect to the other media. Trypsin has a low specific dipole moment however, as explained before its structural and vibrational features are more absorbent than salts. In addition to these results a preliminary measurement of an enzyme assay was reported in Figure 2.54.

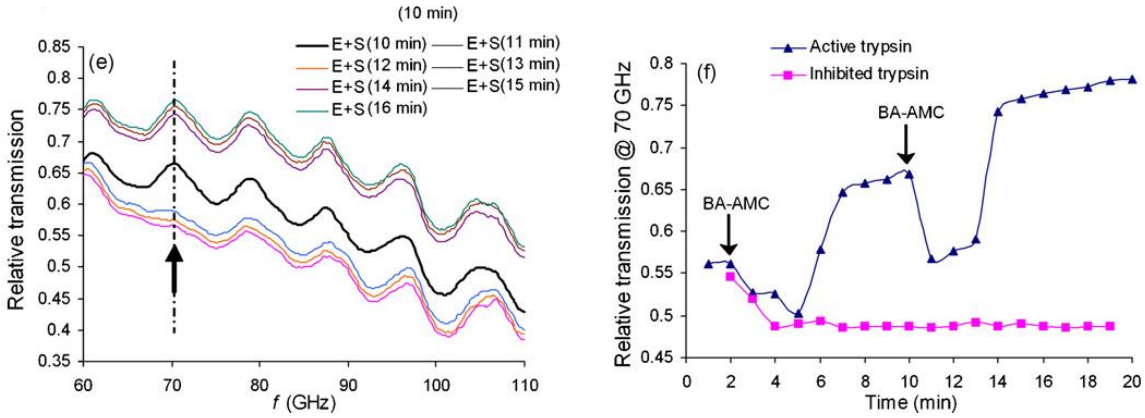

Figure 2.54 Relative transmissions after BA-AMC[1] addition. (a) Two consecutive BA-AMC injections (b) only the second injection is represented [2.33].

To highlight the transmission changes, the results they were plotted as a function of time at a frequency of 70 GHz Figure 2.54 (a). As illustrated the BA-AMC3 introduction causes a three-stage response. Firstly there is a rapid decrease in transmission, which can be explained by the same reasons as that of the trypsin effect. The transmission then increases linearly before reaching a plateau for approximately 2 minutes. The linear change corresponds to the medium becoming more transparent to millimetre waves, associated with the hydrolysis reaction of the enzyme activity. The plateau is a result of the enzyme reaching a maximum reaction rate. Reportedly these are the first results of detecting enzyme reactions in aqueous media using a sub-THz technique. This bio-functionalised device could become an interesting tool to monitor bio-interactions at very small volumes, thus approaching real values of the enzyme kinetic parameters.

1 Nα-benzoyl-L-arginine-7-amido-4-methylcoumarin hydrochloride

Matvejev *et al.* have produced an integrated waveguide structure for highly sensitive THz spectroscopy of small volume liquids in capillary tubes [2.34]. The device is composed of an integrated low-loss hexagonal cross-section waveguide and a commercially available fused silica capillary tube. The device is shown in the figure below, Figure 2.55.

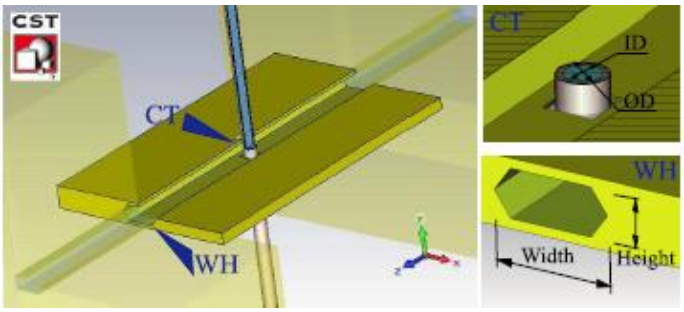

Figure 2.55 A schematic cut-away view of the hexagonal waveguide with integrated capillary sensor configuration. [2.35]

Studies were carried out on DNA concentrations, protein concentrations and protein binding. The results are shown in the figures below, Figure 2.56.

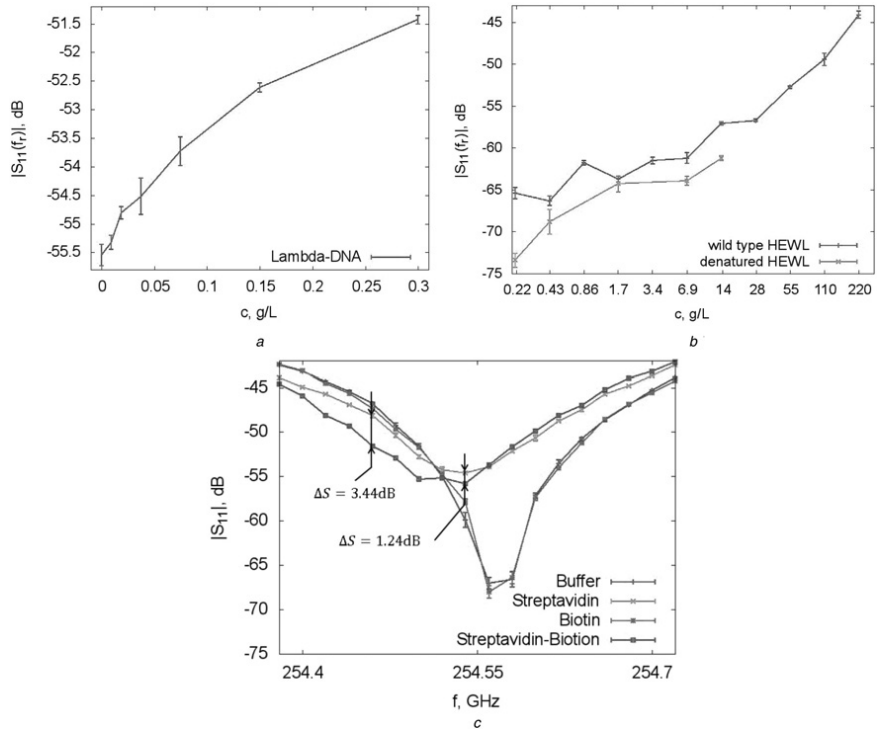

Figure 2.56 Resonant mode sensor reflection signal response to a) Lambda DNA concentration b) Wild-type and denatured hen egg white lysozyme (HEWL) protein, c) Streptavidin and biotin binding. [2.34]

A steady increase in the reflection signal magnitude is observed in the DNA and protein concentration studies. These are attributed to the gradual dielectric permittivity drift away from bure water value. The denatured protein shows a lower reflection magnitude compared to the wild-type protein, this is caused by dielectric properties of the denatured HEWL solution being closer to the buffer. The Streptavidin and biotin protein binding shows that on their own there is little difference in the spectra, however once they are bound the transmission signal drops significantly. This reduced reflection signal corresponds to an increased water content and indicates the protein-ligand interaction. The developed device achieves an excellent detection limit, DNA in the order of 53 dB/(g/l), however in order to outperform optical techniques this limit will need to be further improved.

As discussed, there are many techniques utilising the label-free nature of electromagnetic characterisation. From VLF to microwave to THz frequencies, there are advantages and disadvantages for each of them. As VLF offers poor sensitivity and as THz requires specialised sources and detectors this project focuses on using microwaves in the X-band, 7–12 GHz. Building on the work of Lopez-Villarroya [2.36] and detailed in Chapter 3 E-Plane Sensor: Modelling and Theory, a device with an integrated microfluidic channel within a waveguide-based resonator with localized increased near-fields and sharp resonant features for a label-free chemical/biochemical sensor is proposed.

2.4 Bragg Reflection Waveguides

In addition to the X-band waveguide-based device, the Distributed Bragg Reflector (DBR) resonator is also investigated. This type of device confines most of the field energy of the resonant mode in an empty cavity and shields the walls of the metal enclosure using low-loss dielectric reflectors. These reflective arrays are similar to the DBR commonly used in laser structures, however, the microwave DBR resonant structure must achieve full three-dimensional confinement to achieve the desired benefits. The achievable Q-factors of these devices can be in the 100 of thousands. Such a high Q-factor allows these types of devices to be exploited in sensing devices as the higher the Q-factor the higher the sensitivity. The following section describes the work currently being carried out on such devices.

Michael E. Tobar *et al.* produced a spherical Bragg reflector resonator with a Q-factor of 22,000 at 13.86 GHz [2.37]. The resonator was fabricated from a Teflon spherical shell suspended in a spherical copper cavity using polystyrene. The polystyrene foam did not affect the frequency or Q-factor as the permittivity is close to unity due to its porosity, and the microwave losses are therefore small.

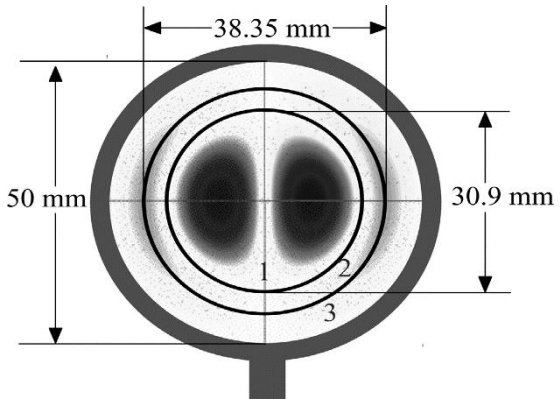

Figure 2.57 Schematic of the SBR resonator, showing the dimensions of the spherical Teflon shell (region 2) suspended in a spherical copper cavity. The magnetic field intensity of the mode is shown and exists mainly inside the Teflon shell (region 1) [2.37].

The measurements using a network analyser in transmission are shown below. The probe coupling was set to be uncoupled and small so that the loaded Q-factor was equal to the unloaded Q-factor. The frequency measured was 13.869 GHz. The Lorentzian bandwidth was 635 kHz, producing a Q-factor of approximately 22,000.

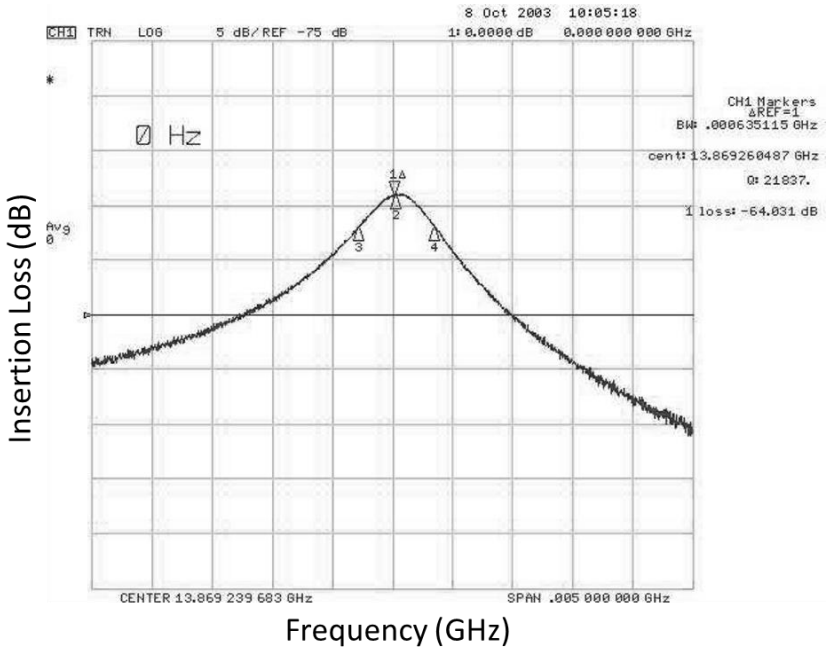

Figure 2.58 Frequency and q-factor measurements using the network analyser [2.37].

The main limitation of the Q-factor in this work was the use of Teflon. The simulations carried out by Tobar *et al.* suggest a low-loss dielectric such as sapphire would allow a higher Q-factor, in the order of 300,000. This work demonstrates the effectiveness of this type of resonator.

Laporte *et al.* also presented a Bragg Reflector structure that was capable of achieving an unloaded Q-factor in the region of 190,000 with one layer at 10 GHz using sapphire [2.38]. The device structure is depicted below, Figure 2.59, along with the fabricated device.

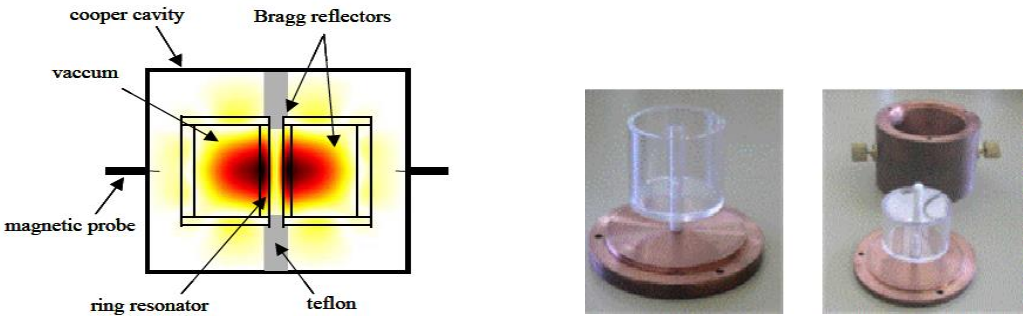

Figure 2.59 (a) Schematic of the sapphire resonator with axial and radial Bragg reflectors (b) Sapphire resonator and copper cavity [2.38].

The Q-factor and frequency was measured using a network analyser. The results are shown in the graph below, Figure 2.60.

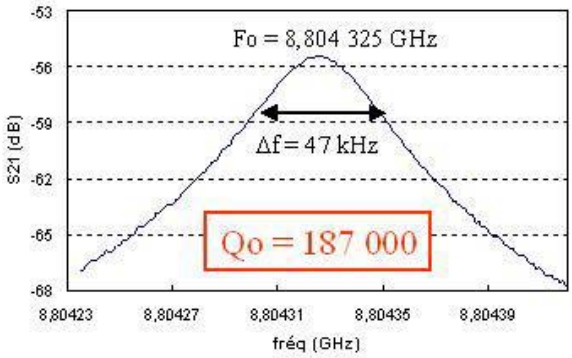

Figure 2.60 Measured transmission coefficient S_{21} along with the frequency and Q-factor of the device [2.38].

The measured results agree well with their theoretical work. This work demonstrates that low loss dielectric material such as sapphire can dramatically increase the q-factor of the device.

The work of Bale and Everard describe an X-band cylindrical distributed Bragg resonator that uses an aperiodic arrangement of non-lambda/4 low-loss aluminium plates [2.39]. The device consists of 6 dielectric plates mounted in an aluminium shield. The schematic and fabricated device is shown below, Figure 2.61.

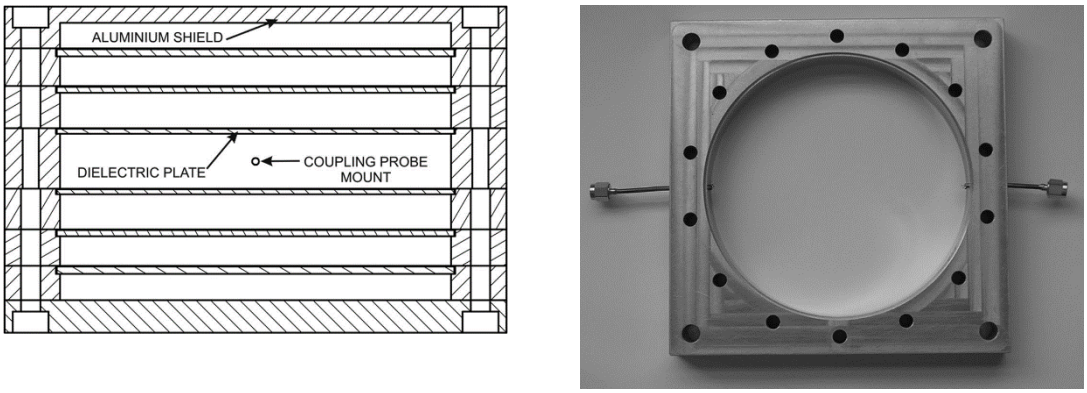

Figure 2.61 (a) a cross-sectional view of the 6 plate aperiodic Bragg resonator. (b) Aperiodic Bragg resonator with central air-filled section [2.39].

The device was measured and found to have a centre frequency of 9.94 GHz with a loaded Q-factor of 126,810 and an insertion loss S_{21} of -8.98 dB. The unloaded Q-factor was calculated to be 196,797. These measurements are in good agreement with their simulations. In comparison to the previous devices described the Q-factor is similar in value. The design simulations showed that higher Q-factors in the region of 400,000 were achievable.

Having explored the current DBR resonators and their capabilities, this project proposes a prototype device that exploits the high Q-factors of these devices for a highly sensitive chemical sensor.

2.5 Conclusions

In order to quickly and objectively compare each of the sensing devices from their various frequencies, waveguide-based techniques and tested mediums, a table of the various literature reviewed in this chapter is shown below inTable 2.2. The frequencies of each device range from 4 x 10^{-8} to 60 GHz, each requiring a Network Analyser. Most devices sampled liquids including water, ethanol, and biological material. Sheen [2.12] and Lobato [2.19] investigated the permittivities of solids. By identifying gaps in the literature a new sensing device can be investigated. The X-band (7 – 12 GHz) was chosen as it is in the microwave region providing more sensitivity to changes in permittivity than lower frequencies. This frequency band also, due to the nature of the waveforms, caters for cheaper and more established fabrication techniques.

Having reviewed this literature on microwave sensing devices, this thesis will investigate the E-plane microwave filter design with an integrated microfluidic channel. Experiments will be carried out on various chemical and biochemical solutions, as well as varying designs of the microfluidic channel to develop a novel sensing device. Further to this work the advantages of the high Q-factor distributed Bragg reflector resonators will also be investigated for use as a sensing device.

Table 2.2 Comparison of the various electromagnetic sensing techniques

Reference	Frequency Range (GHz)	Fabrication	Sample	Additional Equipment	Results (Sensitivity, Q-factor)
Facer, Notterman *et al.* 2001 [2.5]	4 10^{-8}	Glass substrate, Ti-Au Metal lines, PDMS channel, PECVD[2]	Haemoglobin, bacteriophage DNA, E. coli	Hewlett-Packard 4294A impedance analyzer Hewlett-Packard 8510C VNA	Permittivity data and transmission spectra
Qureshi, Niazi *et al.* 2010 [2.6]	0.05- 0.1573	Interdigitated gold capacitor arrays with immobilized antibodies	Biomarkers associated with cardiovascular risk (CPR, IL6, TNFα)	VNA with probe system	Good sensitivity, 25pg/ml to 25ng/ml, however variations in manufacturing and antibody stability offers poor reliability
Qureshi *et al.* 2015 [2.8]	0.15 – 0.275	Interdigitated gold capacitor arrays with immobilized antibodies	Biomarkers associated with aggressive forms of breast cance (HER2)	Agilent 8720ES VNA with Karl Süss PM-5 RF Probe Station	Good sensitivity, 200 pg/ml to 2 ng/ml, however variations in manufacturing and antibody stability offers poor reliability
Mi, Yong et al. 2005 [2.10]	4.5-26.5	Rectangular copper waveguide, cylindrical coupling, sample slot	99.9% Yrrtrium Iron Garnet(YIG), boron nitride, magnesium fluoride	VNA	Good comparison to manufacturers data
Sheen 2009 [2.12]	10.16	Rectangular cavity with circular aperture coupling	Solid ceramics	VNA	Q-factor around 900, agree with another measurement taken using a different method

2 Plasma Enhanced Chemical Vapour Deposition

Reference	Frequency Range (GHz)	Fabrication	Sample	Additional Equipment	Results (Sensitivity, Q-factor)
Nikawa and Yong 2007 [2.13]	2.45	Cylindrical cavity resonator	99.9% alumina, 99.5% alumina, Poly Phenylene Sulfide (PPS), Polyether Ether Ketone (PEEK), Polyimide imide (PAI)	VNA, Amplifier, attenuator, cooling system, infrared thermometer	1.5% or less error in dielectric constant
Kawabata *et al.* 2004 [2.15]	1.95 – 2.00	Cylindrical cavity resonator	Pure water, Alcohol	VNA	Within 2.2 % for ε_p and 1.6 % for tan δ_p
Saeed, Pollard et al. 2008 [2.16]	8	RT/Duroid 5880 substrate, silver epoxy metallization of cavity walls, borosilicate glass for the capillary	Various alcohol solutions	Agilent PNA E8361A	Worst case measurement discontinuity 0.5%, Q-factor unloaded 700 at 8GHz. For a change in dielectric constant of 0.5, there is a shift of almost 4.4 MHz in the resonant frequency, indicating a high sensitivity.
Ferrier, Hladio et al. 2008 [2.18]	2.3	Copper high-Q ¼ wavelength cylindrical cavity resonator. RC circuit. Glass and chromium/gold electrodes fabricated using standard photolithography processes.	Polystyrene spheres, yeast cells, water	Automation syringe pump, detection system as shown in Fig 3 in paper.	Electromanipulation of cells with simultaneous capacitive detection can be achieved, results agree reasonably well with simulation. The sensitivity of this resonator is estimated to be 1.44 MHz/ fF.

Reference	Frequency Range (GHz)	Fabrication	Sample	Additional Equipment	Results (Sensitivity, Q-factor)
Lobato-Morales, Corona-Chavez et al. 2010 [2.19]	7	Rogers RT/duroid 5880 substrate, metallic posts as lateral walls, coaxial probe transition	Solid samples including Teflon, wood, quartz etc.	Agilent-PNA series VNA E8361A	Maximum deviation compared to literature values 6%. Measured values of resonant frequency and *Q* factor are 7.17625 GHz and 517.2072, respectively. The sensitivity *s=dF/d_s_* from simulations with cavity 1 results of *s*=0.2338%, while the experimental sensitivity is of *s*=0.1576%.
Grenier, Dubuc et al. 2009 [2.20]	0.4	CPW – quarz substrate with CPW lines fabricated using lift-off process of chromium/gold, PDMS microfluidic channel	Ethanol, water, human umbilical vein endothelial cells (HUVECs)	Microwave probes, VNA	Validated method with water and ethanol. Rapid and precise characterisation of HUVAC cell suspensions. Minimal cell concentration of 35 10 cells/mL defined.
T. Chen *et al.* 2015 [2.22]	0 – 40	CPW with capacitive gap – quartz substrate with gold CPW lines, PDMS used for microfluidic channel	Living single B lymphoma cells	Microwave probes, VNA	At time of publication it was the first known work for presenting dielectric spectra of a single living cell.
Y. F. Chen *et al.* 2014 [2.23]	0 - 40	CPW – quartz substrate gold CPW lines, detection area etched into CPW line	Hepatoma G2 cancer cells (HepG2)	Agilent N5247 on-wafer Network Analyser	Cell characterisation down to 20 cells/µl

Reference	Frequency Range (GHz)	Fabrication	Sample	Additional Equipment	Results (Sensitivity, Q-factor)
Booth, Mateu et al. 2006; Mateu, Orloff et al. 2007 [18] [2.25]	10^{-6} – 40	Transmission lines, interdigitated capacitors integrated PDMS microfluidic channel	Water and ethanol latex beads	VNA	Accurate to 10%
Sanghyun, Stintzing et al. 2008 [2.27]	1	Photolithography, electroplating, su-8 reservoir, glass substrate	Methanol, isopropanol, human kidney cell-line (HEK-293)	Anritsu 37397C VNA, microwave probes, pipette	Permittivity measurements, DMSO[3] toxicity tests
Dalmay, Pothier et al. 2008 [2.29]	10	Not much given, fused silica substrate with gold metallic lines.	Keratinocytes HaCaT cells (skin cells), glial cells derived from tumor glioblastoma (nervous system astrocyte cells), ficoll solution	Wafer probing and standard VNA	RF Characterisation – S21 transmission parameters, relative effective permittivity and conductivity results
A. Landoulsi *et al.* 2014 [2.30]	0 - 8	Silica substrate with gold capacitance lines. SU8 and PDMS used to define the microfluidic channel	Ethanol and water concentrations	VNA and Agilent 85070 dielectric probe kit	Results agree well with the satandard dielectric probe kit method.

3 Dimethylsulfoxide

Reference	Frequency Range (GHz)	Fabrication	Sample	Additional Equipment	Results (Sensitivity, Q-factor)
T. Yun and S. Lim 2014 [2.31]	3.8 – 5.6	Rogers Duroid 6010 substrate with copper patterning	Alluminium with various depths of cracks	VNA	Results agree well with simulated measurements carried out in HFSS.
Treizebre, Bocquet et al. 2008 [2.32]	60	Quartz substrate – transparent and low loss, gold metallization.	Lactoferrin solution in PBS[4], CHO[5] cells	VNA Wafer probing and standard VNA	Spectrum of lactoferrin solutions in PBS, cell culture of CHO within channel
V. Matvejev *et al.* 2014 [2.34]	220 - 340	Silicon substrate metallised with gold. Standard fused silica capillary tube	Alcohol solutions, DNA, HEWL concentraions, Streptavidin and biotin binding	Millimeter Vector Network Analyser	State-of-the-art detection limit for DNA of 53 dB/(g/l)

4 Phosphate Buffer Saline

5 Chinese Hamster Ovary

2.6 References

[2.1] M. Leahy-Hoppa, M. Fitch, and R. Osiander, “Terahertz spectroscopy techniques for explosives detection,” *Analytical and Bioanalytical Chemistry,* vol. 395, no. 2, pp. 247-257, 2009.

[2.2] S. Y. Huang, Y. X. J. Wang, D. K. W. Yeung, A. T. Ahuja, Y.-T. Zhang, and E. Pickwell-MacPherson, “Tissue characterization using terahertz pulsed imaging in reflection geometry,” *Physics in Medicine and Biology,* vol. 54, no. 1, pp. 149, 2009.

[2.3] N. Krumbholz, T. Hochrein, N. Vieweg, T. Hasek, K. Kretschmer, M. Bastian, M. Mikulics, and M. Koch, “Monitoring polymeric compounding processes inline with THz time-domain spectroscopy,” *Polymer Testing,* vol. 28, no. 1, pp. 30-35, 2009.

[2.4] S. Yao-Chun, and P. F. Taday, “Development and Application of Terahertz Pulsed Imaging for Nondestructive Inspection of Pharmaceutical Tablet,” *Selected Topics in Quantum Electronics, IEEE Journal of,* vol. 14, no. 2, pp. 407-415, 2008.

[2.5] G. R. Facer, D. A. Notterman, and L. L. Sohn, “Dielectric spectroscopy for bioanalysis: From 40 Hz to 26.5 GHz in a microfabricated wave guide,” *Applied Physics Letters,* vol. 78, no. 7, pp. 996-998, 2001.

[2.6] A. Qureshi, J. H. Niazi, S. Kallempudi, and Y. Gurbuz, “Label-free capacitive biosensor for sensitive detection of multiple biomarkers using gold interdigitated capacitor arrays,” *Biosensors and Bioelectronics,* vol. 25, no. 10, pp. 2318-2323, 2010.

[2.7] A. Quershi, Y. Gurbuz, W. P. Kang, and J. L. Davidson, “A novel interdigitated capacitor based biosensor for detection of cardiovascular risk marker,” *Biosensors and Bioelectronics,* vol. 25, no. 4, pp. 877-882, 12/15/, 2009.

[2.8] A. Qureshi, Y. Gurbuz, and J. H. Niazi, “Label-free capacitance based aptasensor platform for the detection of HER2/ErbB2 cancer biomarker in serum,” *Sensors and Actuators B: Chemical,* vol. 220, pp. 1145-1151, 12/1/, 2015.

[2.9] I. Diaconu, C. Cristea, V. Hârceagă, G. Marrazza, I. Berindan-Neagoe, and R. Săndulescu, “Electrochemical immunosensors in breast and ovarian cancer,” *Clinica Chimica Acta,* vol. 425, pp. 128-138, 10/21/, 2013.

[2.10] L. Mi, W. Yong, and M. N. Afsar, "Precision measurement of complex permittivity and permeability by microwave cavity perturbation technique." pp. 62-63 vol. 1.

[2.11] *Hollow metallic waveguides, Part 2: Relevant specifications for ordinary rectangular waveguides* IEC Standard 60153-2*,* 1974.

[2.12] J. Sheen, “Measurements of microwave dielectric properties by an amended cavity perturbation technique,” *Measurement,* vol. 41, no. 1, pp. 57-61, 2009.

[2.13] Y. Nikawa, and G. Yong, "Dynamic Measurement of Temperature Dependent Complex Permittivity of Material by Microwave Heating Using Cylindrical Cavity Resonator." pp. 1-4.

[2.14] H. Kawabata, and Y. Kobayashi, "Accurate measurements of complex permittivity of liquid based on a TM₀₁₀ mode cylindrical cavity method." p. 4 pp.

[2.15] H. T. Hirokazu Kawabata, Yoshio Kobayashi, “Analysis and Experiments of a TM010 Mode Cylindrical Cavity to Measure Accurate Complex Permittivity of Liquid,” *IEICE Transactions on Electronics,* vol. E87-C, no. 5, pp. 694-699, 2004.

[2.16] K. Saeed, R. D. Pollard, and I. C. Hunter, “Substrate Integrated Waveguide Cavity Resonators for Complex Permittivity Characterization of Materials,” *Microwave Theory and Techniques, IEEE Transactions on,* vol. 56, no. 10, pp. 2340-2347, 2008.

[2.17] E. Grant, and B. J. Halstead, “Dielectric parameters relevant to microwave dielectric heating,” *Chemical Society Reviews,* vol. 27, no. 3, pp. 213-224, 1998.

[2.18] G. A. Ferrier, A. N. Hladio, D. J. Thomson, G. E. Bridges, M. Hedayatipoor, S. Olson, and M. R. Freeman, “Microfluidic electromanipulation with capacitive detection for the mechanical analysis of cells,” *Biomicrofluidics,* vol. 2, no. 4, pp. 044102, 2008.

[2.19] H. Lobato-Morales, A. Corona-Chavez, D. V. B. Murthy, and J. L. Olvera-Cervantes, “Complex permittivity measurements using cavity perturbation technique with substrate integrated waveguide cavities,” *Review of Scientific Instruments,* vol. 81, no. 6, pp. 064704-064704-4, 2010.

[2.20] K. Grenier, D. Dubuc, P. E. Poleni, M. Kumemura, H. Toshiyoshi, T. Fujii, and H. Fujita, “Integrated Broadband Microwave and Microfluidic Sensor Dedicated to Bioengineering,” *Microwave Theory and Techniques, IEEE Transactions on,* vol. 57, no. 12, pp. 3246-3253, 2009.

[2.21] F. Buckley, and A. A. Maryott, *Tables of dielectric dispersion data for pure liquids and dilute solutions*, Washington: U.S. Dept. of Commerce, National Bureau of Standards, 1958.

[2.22] T. Chen, F. Artis, D. Dubuc, J. J. Fourni, x00E, M. Poupot, and K. Grenier, "Microwave biosensor dedicated to the dielectric spectroscopy of a single alive biological cell in its culture medium." pp. 1-4.

[2.23] Y.-F. Chen, H.-W. Wu, Y.-H. Hong, and H.-Y. Lee, “40 GHz RF biosensor based on microwave coplanar waveguide transmission line for cancer cells (HepG2) dielectric characterization,” *Biosensors and Bioelectronics,* vol. 61, pp. 417-421, 11/15/, 2014.

[2.24] J. C. Booth, J. Mateu, M. Janezic, J. Baker-Jarvis, and J. A. Beall, "Broadband Permittivity Measurements of Liquid and Biological Samples using Microfluidic Channels." pp. 1750-1753.

[2.25] J. Mateu, N. Orloff, M. Rinehart, and J. C. Booth, "Broadband Permittivity of Liquids Extracted from Transmission Line Measurements of Microfluidic Channels." pp. 523-526.

[2.26] H. P. Schwan, “Electrical properties of tissue and cell suspensions,” *Adv Biol Med Phys,* vol. 5, pp. 147-209, 1957.

[2.27] S. Sanghyun, T. Stintzing, I. Block, D. Pavlidis, M. Rieke, and P. G. Layer, "High frequency wideband permittivity measurements of biological substances using coplanar waveguides and application to cell suspensions." pp. 915-918.

[2.28] M. Kent, “A simple flowthrough cell for microwave dielectric measurements,” *Journal of Physics E: Scientific Instruments,* vol. 22, no. 4, pp. 269, 1989.

[2.29] C. Dalmay, A. Pothier, P. Blondy, F. Lalloue, and M. O. Jauberteau, "Label free biosensors for human cell characterization using radio and microwave frequencies." pp. 911-914.

[2.30] A. Landoulsi, J. Leroy, C. Dalmay, A. Pothier, A. Bessaudou, and P. Blondy, “A Microfluidic Sensor Dedicated to Microwave Dielectric Spectroscopy of Liquids Medium and Flowing Colloidal Suspension,” *Procedia Engineering,* vol. 87, pp. 504-507, 2014/01/01, 2014.

[2.31] T. Yun, and S. Lim, “High-Q and miniaturized complementary split ring resonator-loaded substrate integrated waveguide microwave sensor for crack detection in metallic materials,” *Sensors and Actuators A: Physical,* vol. 214, pp. 25-30, 8/1/, 2014.

[2.32] A. Treizebre, B. Bocquet, D. Legrand, and J. Mazurier, "Studies of cellular informative transfer by THz BioMEMS." pp. 1-2.

[2.33] A. Abbas, A. Treizebre, P. Supiot, N.-E. Bourzgui, D. Guillochon, D. Vercaigne-Marko, and B. Bocquet, “Cold plasma functionalized TeraHertz BioMEMS for enzyme reaction analysis,” *Biosensors and Bioelectronics,* vol. 25, no. 1, pp. 154-160, 2009.

[2.34] V. Matvejev, Y. Zhang, and J. Stiens, “High performance integrated terahertz

sensor for detection of biomolecular processes in solution," *IET Microwaves, Antennas & Propagation,* vol. 8, no. 6, pp. 394-400, 2014.

[2.35] V. Matvejev, C. D. Tandt, W. Ranson, J. Stiens, R. Vounckx, and D. Mangelings, "Integrated Waveguide Structure for Highly Sensitive THz Spectroscopy of Nano-liter Liquids in Capillary Tubes," *Progress in Electromagnetics Research,* vol. 121, pp. 89-101, 2011.

[2.36] R. Lopez-Villarroya, G. Goussetis, J. S. Hong, and J. L. Gomez-Tornero, "E-plane Filters with Selectively Located Transmission Zeros." pp. 733-736.

[2.37] M. E. Tobar, J. M. le Floch, D. Cros, and J. G. Hartnett, "Distributed Bragg reflector resonators with cylindrical symmetry and extremely high Q-factors," *Ultrasonics, Ferroelectrics and Frequency Control, IEEE Transactions on,* vol. 52, no. 1, pp. 17-26, 2005.

[2.38] A. Laporte, J.-M. le Floch, D. Cros, and M. E. Tobar, "Optimization of high-Q Bragg reflector resonator." p. 4 pp.

[2.39] S. Bale, and J. Everard, "High-Q X-band distributed Bragg resonator utilizing an aperiodic alumina plate arrangement," *Ultrasonics, Ferroelectrics, and Frequency Control, IEEE Transactions on,* vol. 57, no. 1, pp. 66-73, 2010.

3 Modelling and Theory of E-plane Sensor

3.1 Background

A configuration of the sensor in this thesis is based on a microwave waveguide E-plane filter. Microwave waveguide filters are essential components of various telecommunication systems. They allow the transmission of desired signals and the attenuation of unwanted signals. Microwave filters in general can consist of any transmission line or waveguide periodically loaded with reactive elements. It is these elements that will determine the frequency response of the filter. Typical frequency responses include low-pass, high-pass, bandpass, and band-reject characteristics.

3.2 E-Plane filters

Metal inserts mounted in the E-plane of a split-block waveguide housing is a well-established technique for realising low cost mass producible microwave filters. A standard configuration of an E-plane filter is given in Figure 3.1.

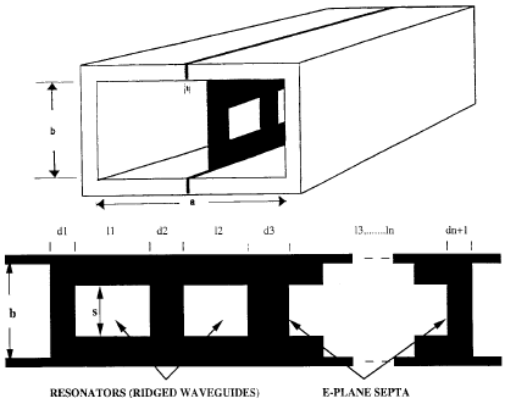

Figure 3.1 Configuration of an E-plane filter structure [3.1].

A standard configuration consists of a split block waveguide housing with all metal septa, acting as inductive obstacles, in the E-plane of the rectangular waveguide. The spacing of these septa are typically half wavelength apart. An advantage of these types of filters is that the metal inserts can be manufactured using standard photolithographic processes. One of the main disadvantages is that the stop-band characteristics are unsuitable for certain applications as spurious harmonic passbands occur at approximately 1.4 times the centre frequency of the waveguide. This has been recently improved upon by Goussetis

et al. in the design of a pair of parallel coupled resonators with selectively positioned transmission zeros [3.2]. The topology of this E-plane filter is shown Figure 3.2.

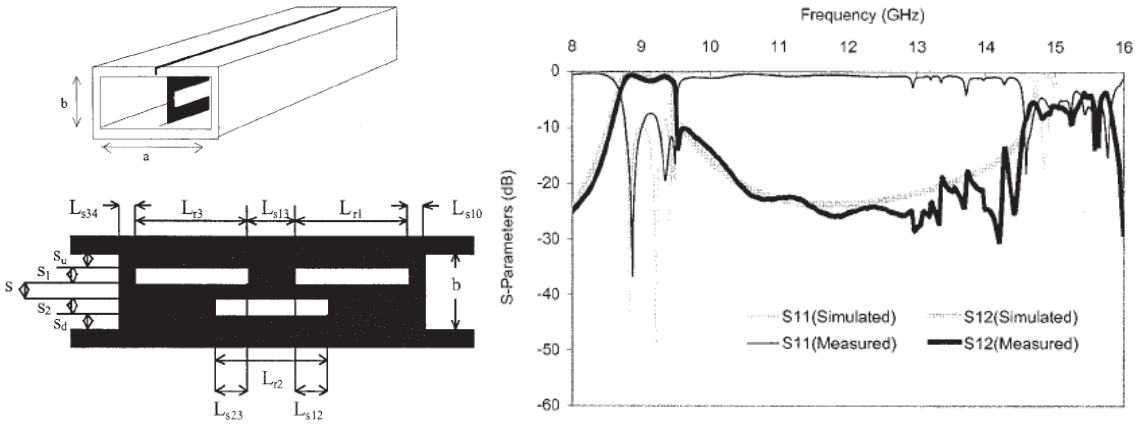

Figure 3.2 Ridge waveguide filter with S-parameter response [3.2].

A ridge waveguide has been incorporated into the metal insert without increasing the manufacturing complexity leading to improved band rejection. The waveguide sections are resonant at a single fundament frequency, and provided that the gap between the ridges differs, there will not be simultaneous higher order resonant frequencies. This results in the spurious harmonic resonances being shifted to even higher frequencies and therefore greatly improving the stop-band rejection. The advantage of this type of configuration over the configuration of the previous figure is that transmission zeros occur at finite frequencies.

There are two paths that the propagating wave can take, which will either be added in phase or out of phase. Thus given this topology the transmission response creates a transmission zero near the passband of the filter.

3.3 E-plane filter structures

Various configurations of E-plane filter design are shown in Figure 3.3.

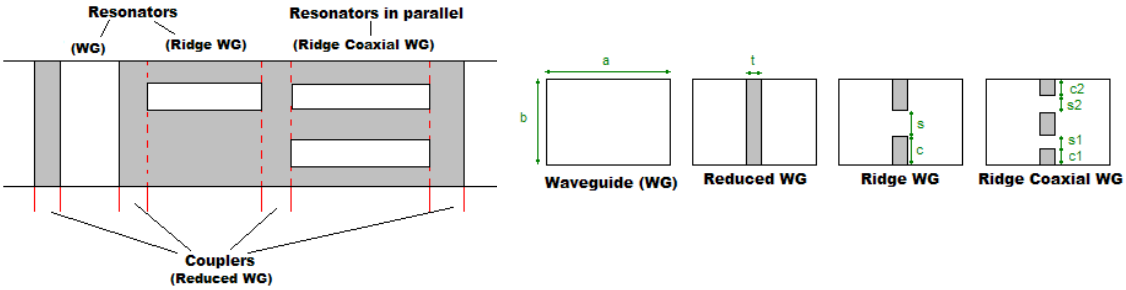

Figure 3.3 E-plane filter configurations a) view from the E-plane b) cross-section of the waveguide

An E-plane filter consists of various elements using inductive couplers and resonators. The metal blocks act as inductive couplers and are essentially reduced waveguide sections. There are also different types of resonators: waveguide (WG), ridge waveguide, and ridge coaxial waveguide. The ridge coaxial waveguide behaves as two resonators in parallel. By using these types of configurations various E-plane filters can be designed.

To calculate the overall filter response it is necessary to solve two different problems. The first is to study the modes that exist in each section of the waveguide. For the nominal waveguide and the reduced waveguide this is done analytically. However, for the ridge waveguide and the coaxial ridge waveguide, numerical methods such as Transverse Resonance and Field Matching are required. These methods are explained in many microwave books and journals as indicated in [3.3]. The second problem is to solve the full wave modelling of the ridge waveguide type E-plane filter. In the example above Figure 3.3(a), it is necessary to solve the discontinuities between the various waveguide (WG) sections – from WG to reduced WG, Ridge WG to Reduced WG and, Ridge WG to Ridge Coaxial WG. The full wave analysis of the waveguide to reduced waveguide has been presented by Bornemann and Arndt [3.4]. The higher order modes of the ridge coaxial waveguide have been studied by Ruiz-Bernal *et al.* [3.5]. Maria Valverde Navarro presents the scattering matrix of the Ridge WG to Reduced WG using the Mode Matching Method [3.6]. This method analyses the fields at the junction of the two waveguides with dissimilar cross-sections. Once all the scattering matrices are obtained for each of the discontinuities then the overall matrix can be obtained by cascading the matrices.

3.4 Wave Propagation in E-Plane Filters

The E-plane filter in this project will be used in an X-band waveguide due to the limitations in manufacturing availability and range of test equipment. The waveguide will be excited to the first TE mode, TE_{10}. The field distribution of the TE_{10} mode is shown in Figure 3.4.

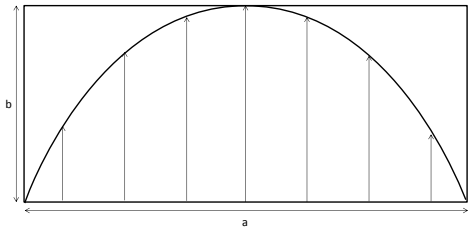

Figure 3.4 Rectangular waveguide TE_{10} mode field distribution.

This mode can only propagate if the frequency is above the cut-off frequency. The cut-off frequency is defined as:

$$f_c = \frac{c_0}{2}\sqrt{\left(\frac{m}{a}\right)^2 + \left(\frac{n}{b}\right)^2} \qquad \textbf{(3.1)}$$

Where c_0 is the speed of light, m and n are the integer mode numbers, and a and b are the width and height of the waveguide. For the first TE mode, TE_{10}, of an X-band waveguide (where a=22.86 mm) the cut-off frequency is 6.56 GHz. The propagation in a waveguide can also be determined by the propagation constant:

$$\beta = \sqrt{k_0^2 - k_c^2} \qquad \textbf{(3.2)}$$

For $k_0 > k_c$, the propagation constant β is real and the mode is propagating with the field distribution along the z-direction of $e^{-j\beta z}$. If $k_0 < k_c$, β is imaginary and therefore the mode is evanescent. The field distribution in a ridge coaxial waveguide is shown in Figure 3.5.

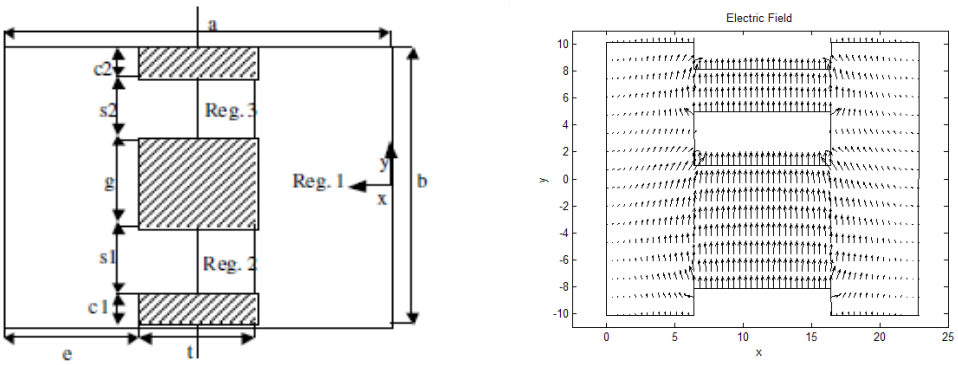

Figure 3.5 Cross-section of the ridge coaxial waveguide with the first TE mode field distribution. [3.5]

The propagated modes in the ridge coaxial waveguide are TEM and the first TE mode. The TEM mode has no cut-off frequency and is the fundamental quasi-static mode in the ridge coaxial waveguide. With reference to Figure 3.3 the field distribution in each of the sections is shown in Figure 3.6.

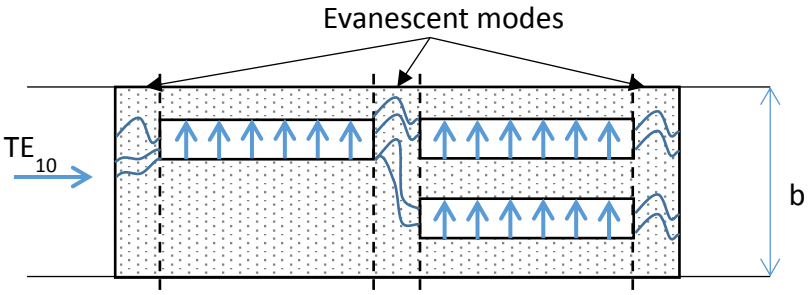

Figure 3.6 Field propagating through an E-plane filter.

As the TE_{10} wave reaches the reduced waveguide the mode becomes evanescent, rapid attenuation of the wave occurs. If the length of the reduced waveguide is too long then there is no more propagation through the waveguide and the amplitude is reduced to zero. If the evanescent mode reached the ridge waveguide the wave is transformed into the first TE mode. The following section is another reduced waveguide where again the wave is in the evanescent mode. This evanescent mode then reaches the ridge coaxial waveguide where the propagation as explained above occurs.

3.5 Parallel Coupled Resonator for Sensing

G. Goussetis *et al.* presented an E-plane ridge waveguide filter that allows for transmission zeros at finite frequencies and can achieve sharp attenuation slopes [3.2]. These features are advantageous as a sensing device as it will make for a highly selective sensor. R. Lopez-Villarroya [3.7] produced the concept design of a perturbed parallel coupled resonator producing narrow band transmission and a sharp roll off feature as shown in Figure 3.7.

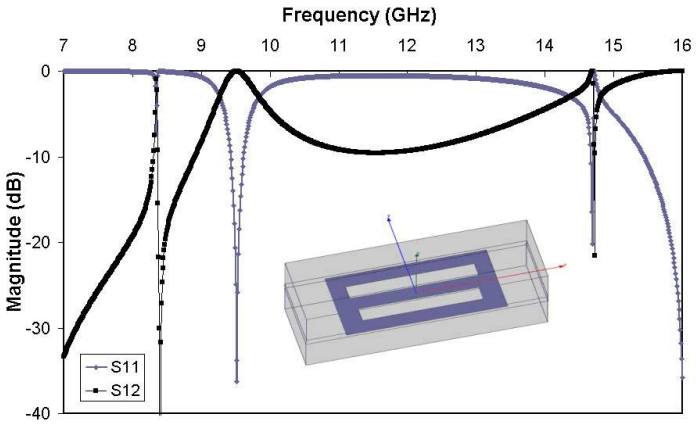

Figure 3.7 S-parameter behaviour of perturbed parallel coupled E-plane filter [3.7].

This design was based on a bandpass filter produced in Chapter 4 of Lopez-Villarroya work [3.7] and [3.2], shown in Figure 3.8. The dimensions of the new parallel coupled filter were based on that of the bandpass filter mentioned and detailed in the table below, Table 3.1.

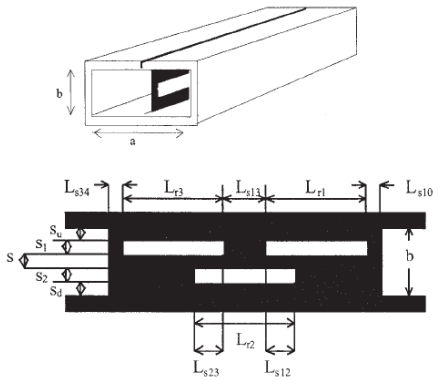

Figure 3.8 Schematic of two parallel coupled resonators. [3.7]

Table 3.1 Dimensions (in mm) of the Lower and Upper resonators for the above prototype (Figure 3.8). [3.2, 3.7]

Prototype	L_{r1}	L_{r2}	s_1	s_2	s	L_{s12}	L_{s10}	L_{s23}
Lower TZ	16	16	2.1	2.1	1.5	11.4	1	1
Upper TZ	16	16	2.1	2.1	1.7	8.4	1	1

In this case of two parallel resonators the dimensions Ls12=Lr1=Lr2. The lower resonator was then reduced to 15 mm to create an asymmetric ridge waveguide part to the waveguide filter. By reducing the length of one resonator, two distinct resonances are distinguishable. In addition, since the two resonances are coupled, at a certain frequency they exactly cancel one another out producing a transmission zero. This narrowband feature can then be exploited in sensing. Integrating a microfluidic capillary to run parallel to the resonators where the near field is at a maximum allows for characterisation of micro-litre fluids. A minute change in dielectric constant of the fluid creates a shift in the resonant frequency of the E-plane filter response.

3.6 HFSS optimization of E-plane filter

The design and simulation of the prototype sensor was carried out in finite element method software package called Ansys HFSS, which is an industry-standard simulation tool for 3-D full-wave electromagnetic field simulation [3.8]. A key benefit of HFSS is its automatic adaptive meshing techniques where only the specify geometry, material properties and the desired output are required as presented schematically in Figure 3.9.

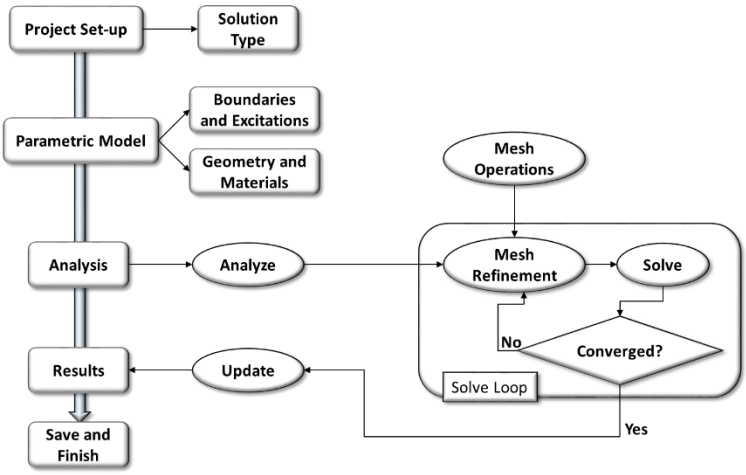

Figure 3.9 HFSS design flow

A schematic diagram of the waveguide E-plane resonator device is shown in Figure 3.10. The lengths of the resonators we reduced to L_r = 13 mm from the Lopez-Villarroya prototype to increase the resonant frequency of the narrowband feature to around 10 GHz. The lower resonator length was reduced from 13 mm to 12.25 mm to create the asymmetric ridge waveguide section to produce the narrowband bandpass. The device was drawn as a 3D structure using the graphical user interface using various 2D and 3D drawing objects. The material properties for these objects were then defined under the property database within HFSS.

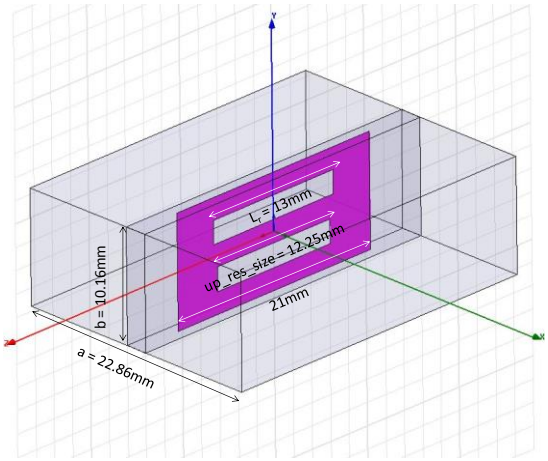

Figure 3.10 3D model of the waveguide E-plane resonator with dimensions.

The boundary conditions for the resonator as a PEC and radiation boundaries of the waveguide are assigned using the boundary assigning tool. Waveports are then assigned to the ends of the waveguide structure. Ports are the boundary conditions in HFSS that allow energy to flow into and out of the structure. Ports are assigned to any 2D object or face. It is necessary to determine the excitation field pattern at each port before the full three-dimensional electromagnetic field inside the structure can be calculated. HFSS uses an arbitrary port solver to calculate the natural field patterns and modes that can exist inside a transmission structure with the same cross-section as the port. A schematic of the waveport for the E-plane resonator is shown in Figure 3.11.

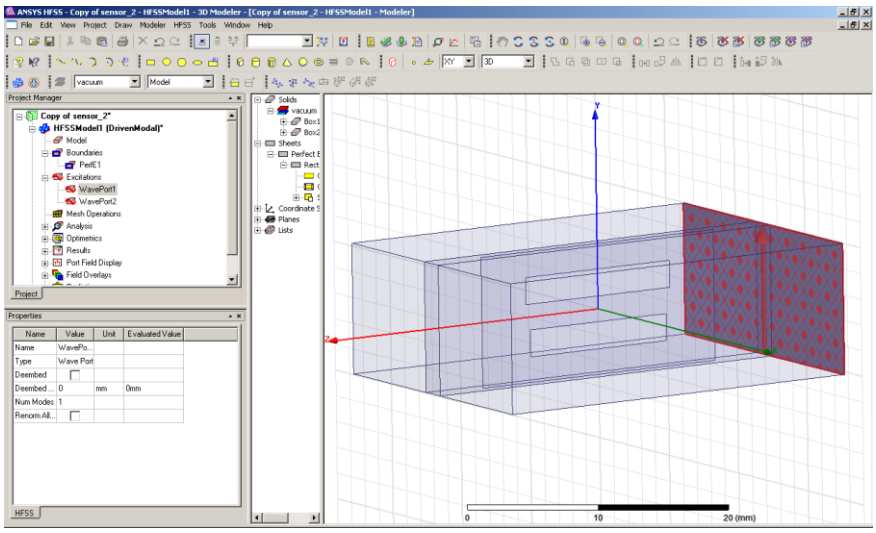

Figure 3.11 Waveport assignment in HFSS for E-plane resonator

A duplicate waveport is also assigned to the opposite end of the waveguide cavity. The perfect E boundary represents a perfect electric boundary where the E-field is forced to be normal to the assigned boundary. The E-plane filter insert was assigned a perfect E boundary as shown in Figure 3.12.

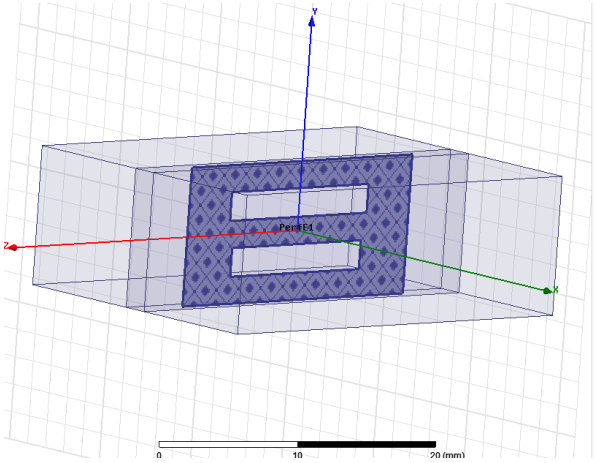

Figure 3.12 Perfect E boundary for E-plane resonator.

A solution set-up is required in order to perform an analysis of the structure. By defining frequency sweep parameters (in driven mode) HFSS obtains the field solutions by solving the boundary value problem of Maxwell's equations. Shown below, Figure 3.13, are the settings used for a driven modal solution for the E-plane resonator.

Solution Setup

Solution Frequency	10.2	GHz
Max. number of passes	10	
Max. delta S	0.02	

Frequency Sweep Setup

Sweep Type	Fast	
Frequency Setup Type	LinearStep	
Start	8	GHz
Stop	12	GHz
Step Size	0.01	GHz

Figure 3.13 Driven modal solution set-up

Once the model was created and ports and boundaries assigned a validation check was performed. The validation check by HFSS ensures that there are no errors associated with the design or settings that could lead to failure of the numerical simulations. Once it has passed the validation check the 3D electromagnetic field analysis is carried out on the structure to obtain its characteristics. HFSS will generate a finite element mesh consisting of tetrahedra elements. These elements are small regions of the overall solution that HFSS uses to analyse the device. There is a trade-off between the size of the mesh, the desired level of accuracy and the amount of computing resources required by HFSS. The mesh generated by HFSS for the E-plane resonator is shown below, Figure 3.14.

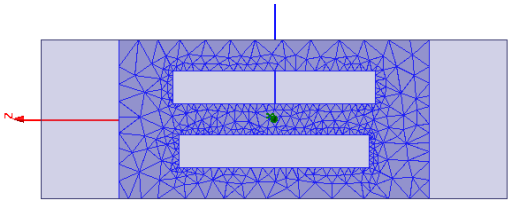

Figure 3.14 E-plane resonator HFSS generated mesh.

Adaptive meshing is used by HFSS to produce the optimal mesh for the more accurate solution. Finer mesh regions appear where there are critical regions of higher error density. HFSS will then use the mesh to perform the frequency sweep for the driven mode and obtain the field solutions at the required frequencies. Once the simulation is complete the user can view various reports and plots. The reflection scattering parameters of the E-plane resonator are shown in Figure 3.15.

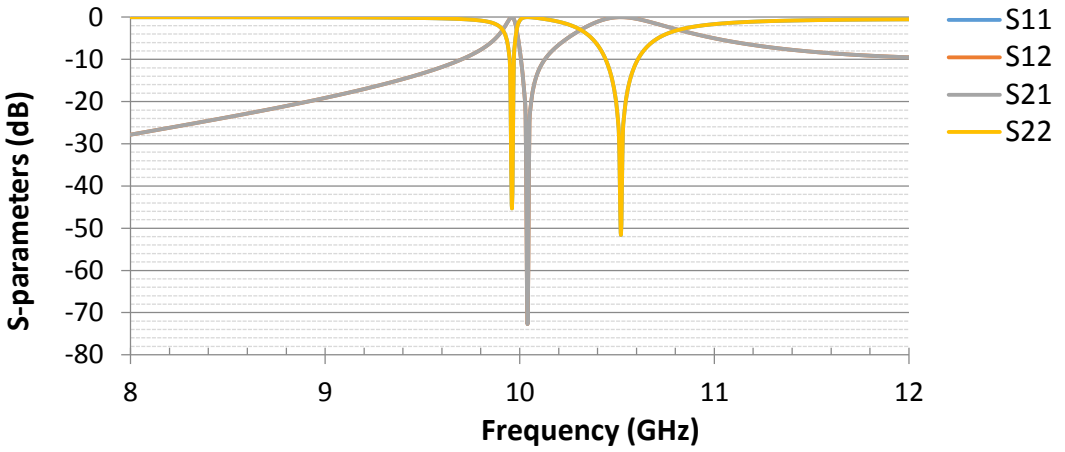

Figure 3.15 Simulated S-parameters of the E-plane resonator by HFSS

The distinct narrow band feature with a sharp roll off is present due to the coupling of the two resonators. By perturbing one of the resonators the two resonances become distinguishable as well as at a certain frequency they exactly cancel out producing a transmission zero. The effect of the lower resonator length differing from the upper resonator is cause for investigation. Simulations in HFSS were carried out to determine the effect of changing the length of the lower resonator with respect to the upper resonator. The length of the lower resonator is varied from 12 mm to 13 mm in steps of 0.25 mm. The upper resonator remained at a length of 13 mm. the effect of this change in length is shown in the following S-parameter plot in Figure 3.16.

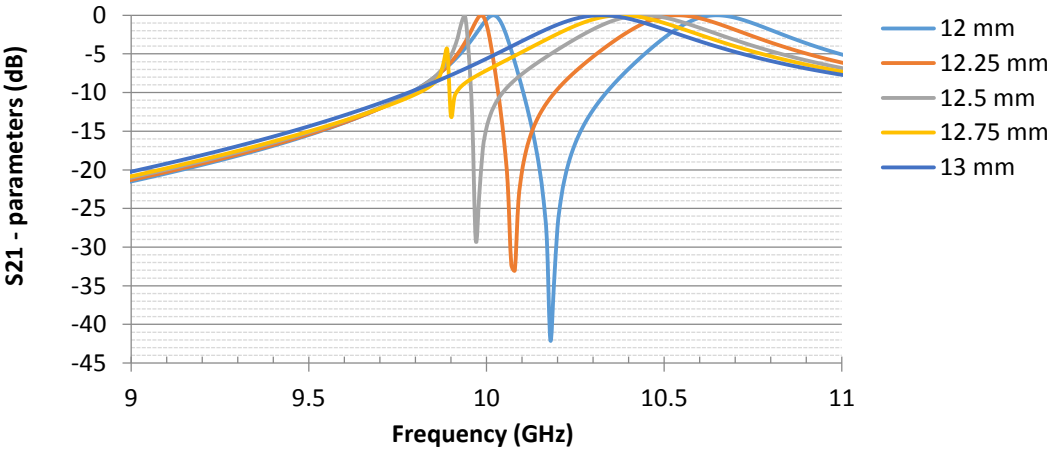

Figure 3.16 S_{21}-parameters of the lower resonator length simulation study.

As a trade-off between the sharpness of the transmission response and the absorption losses the optimal length for the lower resonator was chosen to be 12.25 mm. The resulting transmission pole is at approximately 9.99 GHz with -0.091 dB and the

transmission bandwidth of approximately 60 MHz with sharp roll-off. As the physical device was to be made of a copper sheet a study was carried out on the relative thickness of the sheet and the S-parameter responses observed. The PEC resonator was changed to a copper structure with a thickness initially of 0.1 mm as presented in Figure 3.17.

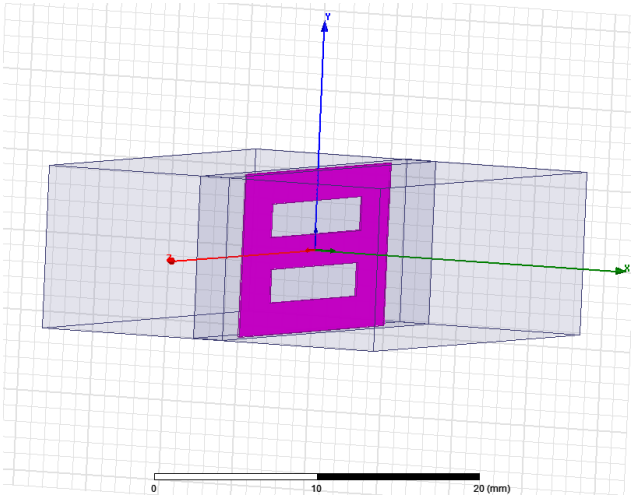

Figure 3.17 HFSS 3D model of the copper E-plane resonator and a 0.1 mm thickness.

An optimetric analysis was then carried out on the resonator thickness from 0.1 mm to 1 mm. The S_{21} results of the optimetric analysis are shown below in Figure 3.18.

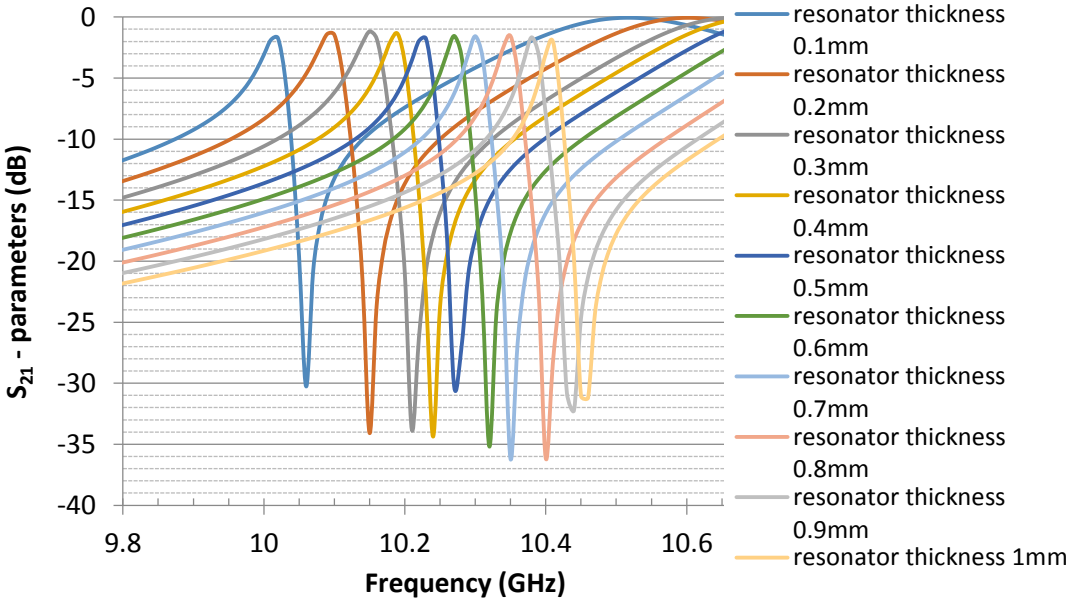

Figure 3.18 HFSS resonator thickness study.

As there is only a change in the resonant frequency and due to the ease of manufacturing capabilities the resonator was chosen to be 0.1 mm thick. As the simulation shows this thickness does not require extreme accuracy as it will not affect the resonator response dramatically. Now that the dimensions of the E-plane filter have been determined the next step was to introduce the capillaries with the sample fluid. As will be discussed in Chapter 4, Design and Fabrication of E-plane Sensor, the carrier for these capillaries will be made from Polymethyl methacrylate (PMMA). The modified HFSS model of the E-plane filter with the PMMA microfluidic capillaries are shown below in Figure 3.19.

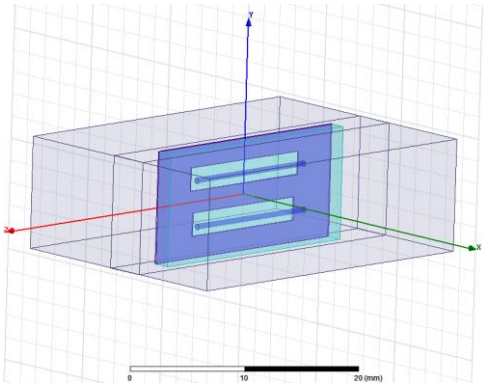

Figure 3.19 HFSS 3D model of E-plane filter with integrated PMMA microfluidic capillaries.

These capillaries were created using simple cylinders placed within the PMMA box that is placed on top of the E-plane filter as shown in Figure 3.20.

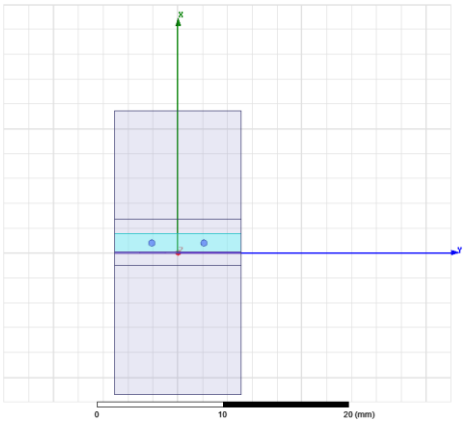

Figure 3.20 Side view of the capillaries within the PMMA holder on top of the E-plane filter.

The properties of the cylinders were one those known permittivities of materials. HFSS allows user materials to be created with known parameters such as relative permittivity, relative permeability, bulk conductivity, etc as indicated in Figure 3.21. The most important properties pertaining to this project are the relative permittivity, relative permeability and loss tangent.

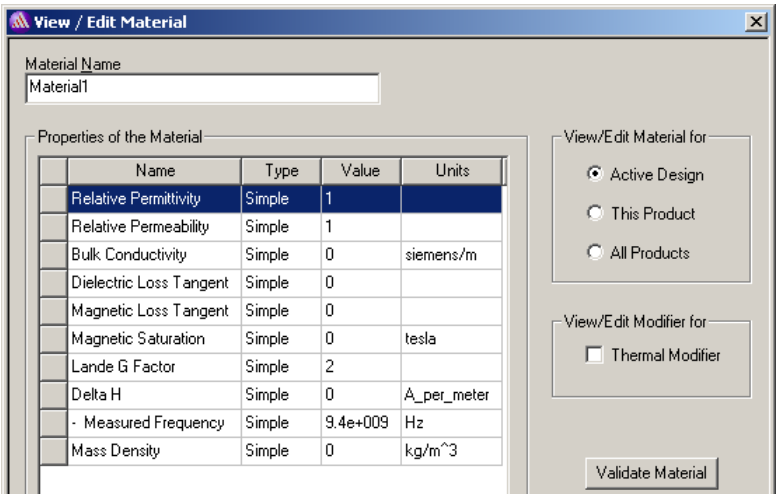

Figure 3.21 HFSS material property window

The relative permittivity was obtained for several materials are outlined in the HFSS window below, Figure 3.22.

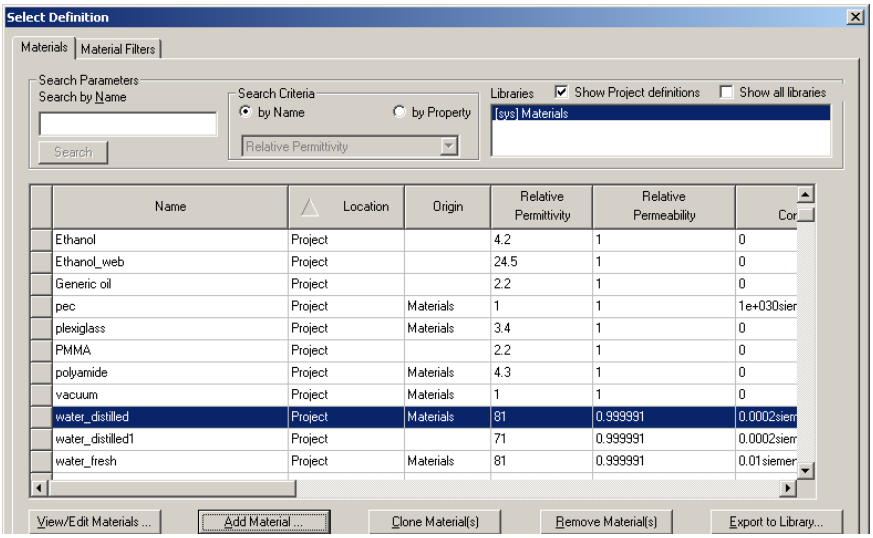

Figure 3.22 HFSS Material properties

The S-parameter results of the E-plane resonator with each of the fluids is shown below, Figure 3.23.

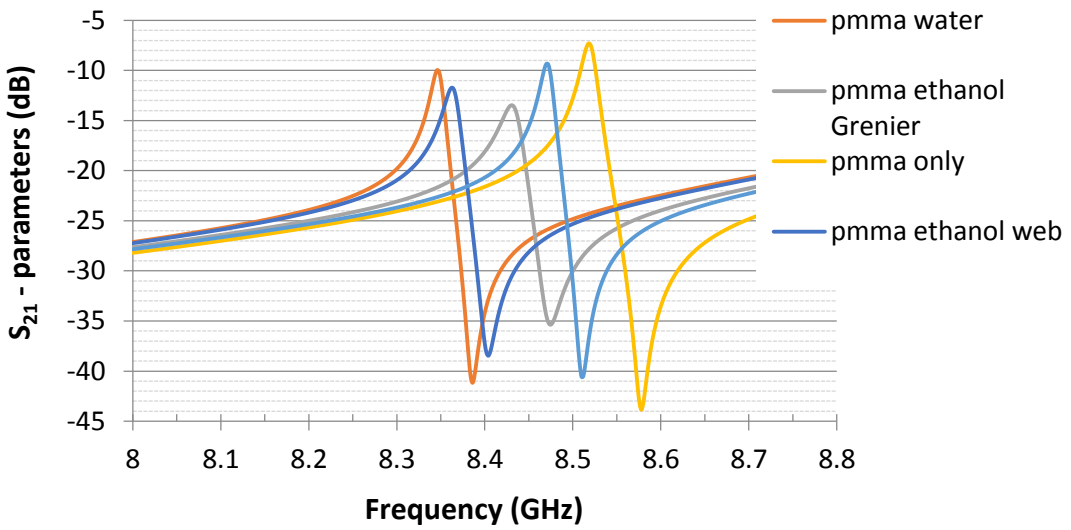

Figure 3.23 HFSS simulation results of S21 parameter of each of the fluids.

The resonant frequency is not only affected by the relative permittivity of each of the samples but also the permeability, loss tangent and bulk conductivity. The resonator response is also affected by the total volume of fluid within the capillaries. The following study, given in Figure 3.24, shows the response of the E-plane filter to the changing volume of capillaries filled with water.

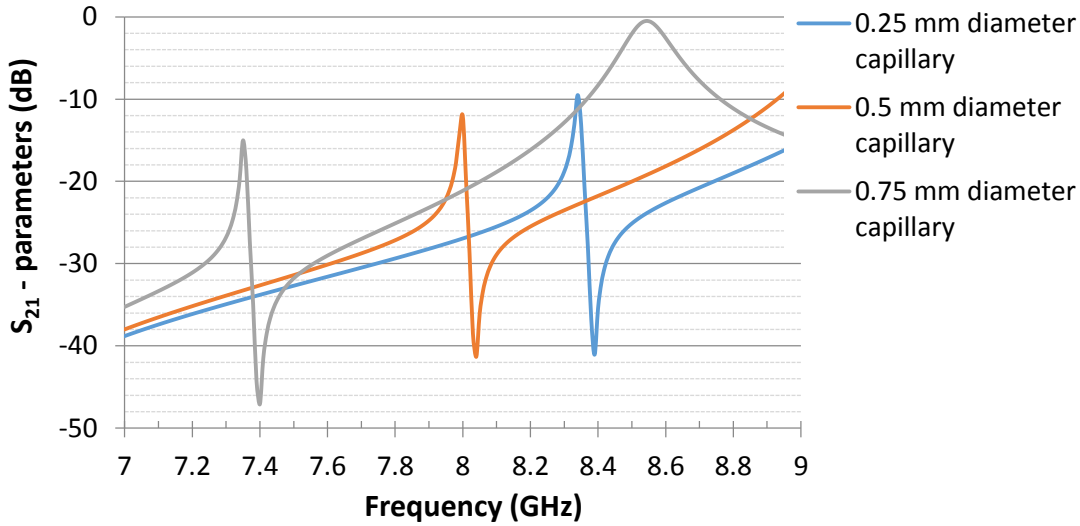

Figure 3.24 HFSS simulation study of diameter of the capillaries.

The higher the volume the lower the resonant frequency of the resonator and there are also higher losses.

3.7 Conclusion

The modelling and theory of the E-plane sensor have been presented. The E-plane filter response has been introduced and following on from various works a parallel coupled resonator was produced. From this characterisation of the filter to improve the overall selectivity was carried out in HFSS. Further modelling was carried out to investigate the effects of the insertion of a PMMA microfluidic channel chip. Various known fluids were then introduced to the model and the effect of volume in the capillaries investigated.

3.8 References

[3.1] D. Budimir, "Optimized E-plane bandpass filters with improved stopband performance," *Microwave Theory and Techniques, IEEE Transactions on,* vol. 45, pp. 212-220, 1997.

[3.2] G. Goussetis, A. P. Feresidis, D. Budimir, and J. C. Vardaxoglou, "A 3rd order ridge waveguide filter with parallel coupled resonators," in *Microwave Symposium Digest, 2004 IEEE MTT-S International*, 2004, pp. 595-597 Vol.2.

[3.3] T. Itoh, *Numerical techniques for microwave and millimeter-wave passive structures*: Wiley New York, 1989.

[3.4] J. Bornemann and F. Arndt, "Modal-S-Matrix Design of Optimum Stepped Ridged and Finned Waveguide Transformers," *Microwave Theory and Techniques, IEEE Transactions on,* vol. 35, pp. 561-567, 1987.

[3.5] M. A. Ruiz-Bernal, M. Valverde-Navarro, G. Goussetis, J. L. Gomez-Tornero, and A. P. Feresidis, "Higher order modes of the Ridged Coaxial Waveguide," in *Microwave Conference, 2006. 36th European*, 2006, pp. 1221-1224.

[3.6] M. Valverde-Navarro, "Análisis de discontinuidades de guía onda y filtros con resonadores guía onda con ridges asimétricos mediante el método mode matching," Escueal Técnica Superior de Ingeniería de Telecomunicación, Universidad Politecnica de Cartagena.

[3.7] R. Lopez-Villarroya, "E-plane parallel coupled resonators for waveguide bandpass filter applications," Engineering and Physical Sciences, Heriot Watt University, 2012.

[3.8] *Ansys HFSS 3D Full-wave Electromagnetic Field Simulation*. Available: http://www.ansys.com/Products/Simulation+Technology/Electronics/Signal+Integrity/ANSYS+HFSS

4. Design and Fabrication of E-Plane Sensor

This chapter describes the design and fabrication of the E-plane sensor. The sensor integrates a microfluidic capillary channel in a waveguide for sensing biological elements in the liquid flowing inside a microchannel. The first section discusses the various fabrication methods and materials used to manufacture microfluidic channels. The second section focuses on the design and fabrication of the electromagnetic waveguide, including methods of integrating the microfluidic channels within the general system.

4.1. Design and Fabrication of Microfluidic Channels

4.1.1. Theory of Microfluidic Channels

Microfluidics uses microscale devices to perform laboratory processes in micro-, nano-, and even pico-litre volumes. This technology has numerous advantages including reduced sample and expensive reagent volumes. At the micro-scale, where laminar flow behaviour is dominant, fluids behave very differently to the macro-scale. Laminar flow is characterised by the Reynolds number, *Re*, defined as the ratio of the inertial forces to the viscous forces acting on a fluid such that [4.1]:

$$Re = \frac{(\rho v D_h)}{\eta} \qquad \textbf{(4.1)}$$

Where η is the viscosity (mPa.s^{-1}); ρ is the density (kg.m^{-3}); v is the flow speed (m.s^{-1}) and D_h is the hydrodynamic diameter of the channel (m). D_h is given by the following relationship:

$$D_h = \frac{4A}{P} \qquad \textbf{(4.2)}$$

Where A is the cross-sectional area (m^2) and P is the wetted perimeter (m). In a microchannel with a circular cross-section D_h is equal to the diameter of the cross-section. The Reynolds number determines whether the flow of the fluid is turbulent (Re>2000) or laminar (Re<2000). In a laminar flow there is no turbulence and hence the very little mixing is by diffusion alone and not by convection. Air bubbles are common as there are high values of surface tension, which can lead to the blocking of the channels. Micronics

has developed the T-sensor to exploit this characteristic laminar flow in microchannels to analyse drugs, proteins, hormones etc. in the blood as well as environmental applications [4.2]. Capillary action is also driven by low Reynolds numbers in the laminar flow regime. Capillary action allows the flow of fluid without any external activation. The difference in pressure and shear forces allows a concave meniscus to form causing the fluid to move along the walls of the capillary. Zimmermann *et al.* used this phenomenon to create capillary pumps negating the need for external activation of fluid flow [4.3]. In this thesis the characteristic laminar flow and the use of capillary pumps provide a useful and automated configuration for the sensing device.

4.1.2. Fabrication of SU-8 Channels

The first microfluidic channels for this thesis work were fabricated using the negative chemically amplified photoresist SU-8 50 on a 50μm Kapton polyimide substrate. SU-8 is a high contrast, epoxy based photoresist designed for micromachining and other microelectronic applications. SU-8 is a chemically inert substance as it will not degrade or react with most chemicals such as alcohols [4.4]. It is also thermally stable once developed and will not change shape when there is a significant temperature change. The shrinkage was noted to be 1.16 times the baking temperature by Feng and Farris [4.5].

The fabrication process begins with the gluing of the polyimide substrate onto a glass carrier substrate for stability and support as shown in Figure 4.1(a). The SU-8 epoxy is then spin coated onto the substrate to produce an approximate thickness of 400 μm as shown in Figure 4.1(b). This is achieved by dispensing approximately 10 ml of SU-8, which then undergoes a spread cycle with a ramp to 500 rpm at 100 rpm/second acceleration. This speed is then held for 7 seconds to allow the resist to cover the entire surface. The speed is then ramped up to 1250 rpm at an acceleration of 300 rpm/second and held for 30 seconds. Once the SU-8 resist is coated it must be soft baked to evaporate the solvent and densify the film. The bake is performed on a level hot plate and is stepped in two stages. First the resist is baked at 65°C for 1 minute and then 12 minutes at 95°C followed by sufficient cooling and relaxation time intervals. The microfluidic structures are then patterned on the SU-8 using mask photolithography. SU-8 is optimized for near UV (350-400 nm) exposure and therefore an i-line filter exposure tool is used. The mask is aligned using a Tamarac mask aligner and the epoxy is exposed to 800 $mJ.cm^{-2}$ for 12seconds as illustrated in Figure 4.1(c).

Following the UV exposure, a post expose bake (PEB) must be performed to selectively cross-link the exposed portions of the film. The PEB is performed on a contact hot plate at a temperature of 55°C for 2 minutes. The structure is then developed in an ethyl lactate based solvent in an immersion process using a magnetic stirrer for 12 minutes. The substrate is then rinsed briefly with isopropyl alcohol (IPA), then dried with a gentle stream of nitrogen as indicated in Figure 4.1(d). The polyimide/SU-8 microchannel structure is then lifted from the glass substrate as illustrated in Figure 4.1(e).

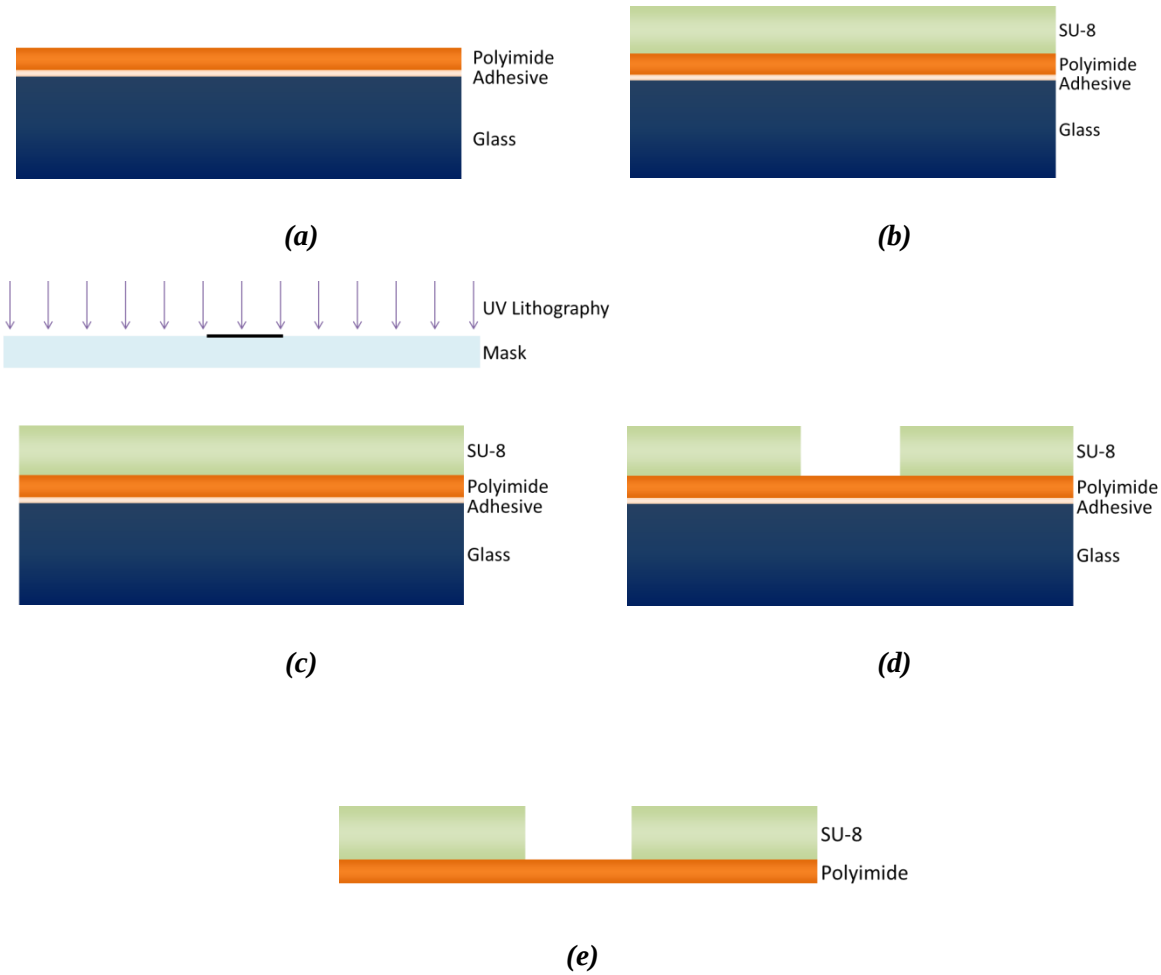

Figure 4.1 Fabrication of microfluidic channels in SU-8 – Glass/polyimide substrate with 100µm spin coated SU-8

The polyimide/SU-8 microchannel structure is shown in Figure 4.2. The design of the microfluidic channels was chosen so that the fluid filled channels were located in the region of high electromagnetic field. The microfluidic channels align with the slots on the E-plane filter as discussed in the previous chapter. Although this design offered advantages with respect to the stability of the channels in terms of measurements, and biocompatibility of the substrate, the fabrication process is very time consuming. Also, as the microfluidic channels were to be used only once, SU-8 proved to be inconsistent in terms of fabrication process. For these reasons, another suitable substrate was investigated for use in the microfluidic channels in the sensor design.

Figure 4.2 Polyimide/SU-8 microfluidic channel

4.1.3. Fabrication of PDMS Channels

Polydimethylsiloxane (PDMS) is the most widely used silicon-based organic polymer. PDMS is optically clear and in general is considered to be inert, non-toxic and non-flammable [4.6]. Figure 4.3 displays a flow diagram of the process steps in fabricating a microfluidic channel in PDMS.

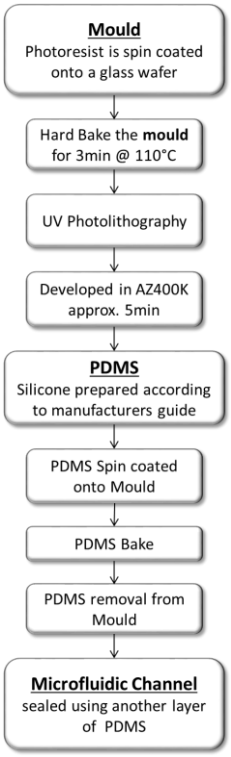

Figure 4.3 Overview of the process steps for fabricating a microfluidic channel in PDMS

These steps are then illustrated below in Figure 4.4.

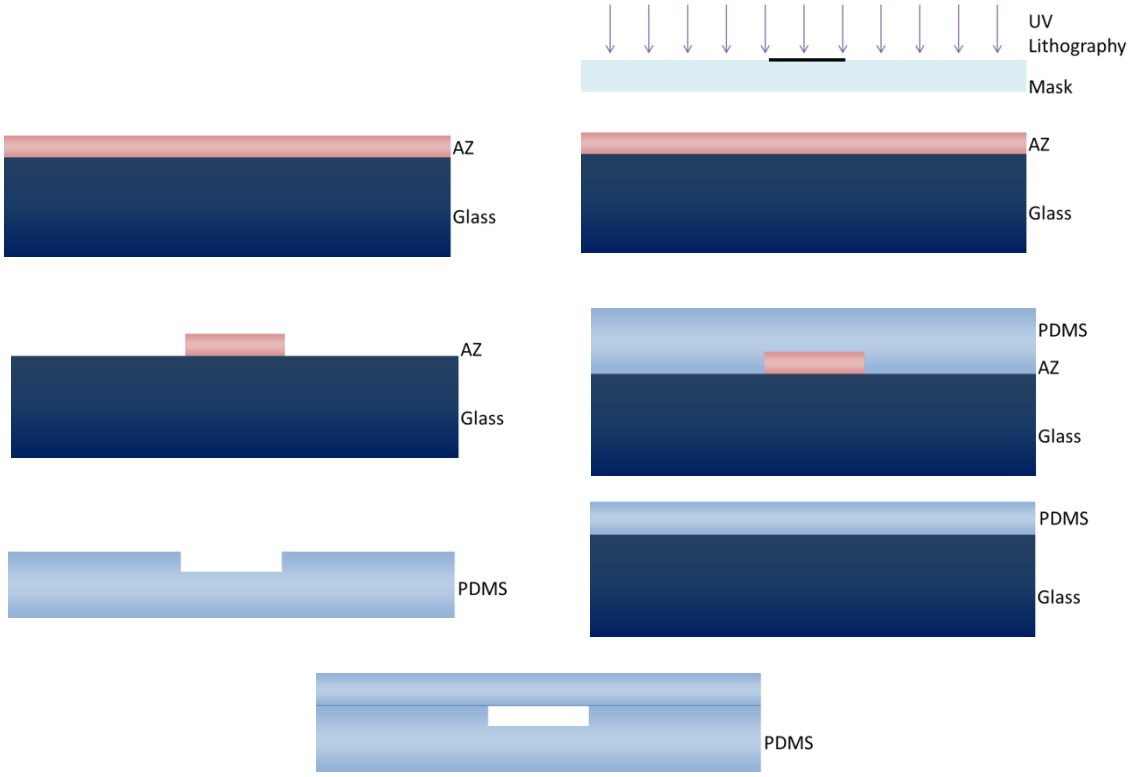

Figure 4.4 Microfluidic channel process steps for PDMS

The PDMS microfluidic channel is fabricated by what is known as soft lithography. With this technique a mould is created in the negative image of the channels to be manufactured and the material is then pressed onto the mould to form the structure. To fabricate the mould for the microfluidic channel a glass substrate is used for stability. This is then spin coated with a photoresist, AZ9260, using the parameters shown in Table 4.1.

Table 4.1 Spin coating parameters for AZ9260 on glass substrate

Steps	**30µm Thickness of AZ**
Distribution of the AZ	70rpm
	30 Rev/s
	20s
Spread Cycle for uniform wafer coverage	400rpm
	100 Rev/s
	20s
Cycle for final photoresist thickness	1000rpm
	200 Rev/s
	10s

Once the spin cycle is complete there is a rest period of 300 seconds prior to hard baking the photoresist to allow the layer to settle onto the substrate. AZ is then hard baked in two steps of 30 seconds at a temperature of 65°C and then 300 seconds at a temperature of 110°C followed by another 1 hour rest period. The baking is carried out in this way to minimise the effects of thermal shock. Thermal shock effects include contraction of the resist, retreat from the wafer perimeter due to a sudden elevation in temperature, resulting in an uneven distribution of photoresist. The delay facilitates the rehydration of the resist, which is important in the UV exposure process. The mould is then exposed to UV light using an acetate mask. The wafer is positioned in the Tamarack UV aligner and the hard contact between the wafer and photomask is maintained by a vacuum. AZ9260 photoresist is photosensitive to the i- and h-line. In this process the UV light is filtered so that the resist is exposed to the i-line (365 nm). The energy dose for exposure is set to 1200mJ for 40 seconds. After exposure, the wafer is developed using AZ developer, AZ400K [4.7], for approximately 3-5minutes and rinsed with deionised water. The wafer is then dried using pressurised nitrogen and the mould is ready for use and shown below in Figure 4.5.

Figure 4.5 AZ mould for PDMS microfluidic channel fabrication

The PDMS used in this fabrication was supplied by Dow Corning under the trade name Sylgard 184 Silicone Elastomer. It is supplied as a two-parts liquid component kit comprised of a base and curing agent that are mixed in a ratio by weight of 10 parts base to one part curing agent. After thoroughly mixing the base and curing agent, the solution is agitated gently to reduce the amount of air introduced. This solution is then spin coated onto the glass/AZ mould. The parameters for the spin coating were taken from F. Schneider et al. work on the use of polydimethylsiloxane (PDMS) for optical MEMS [4.8] as shown in Figure 4.6.

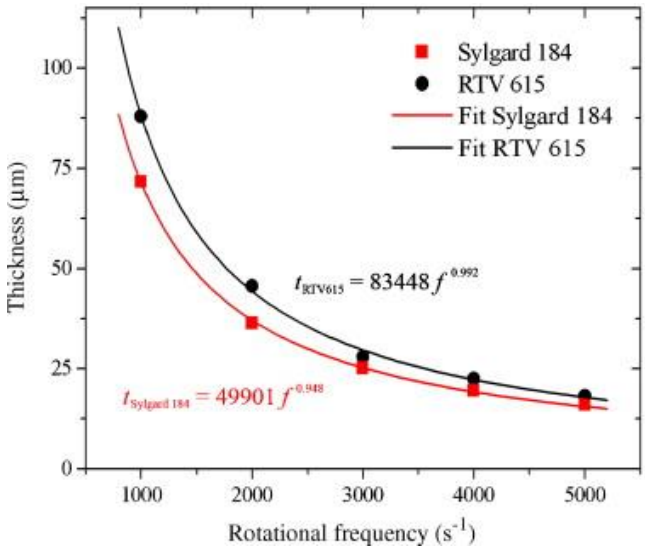

Figure 4.6 Spin curve of Sylgard 184, mean across the whole wafer area [4.8]

The PDMS structure is then cured on the mould at room temperature for 48 hours as prescribed by the manufacturer's guidelines [4.9]. The curing was not accelerated using

heat so as not to create thermal stresses due to thermal expansion mismatch in the moulding process. Once cured the PDMS is then carefully removed from the glass/AZ mould. To seal the microfluidic channel another layer of PDMS is spin coated onto a clean glass substrate and cured using the parameters as before. Holes are then punched for the inlet and outlet of the microfluidic channel. The sheet with the microfluidic channels is then bonded to the top layer using an oxygen plasma treatment using a hand-held corona treatment gun, model BD-20 Electo Technic Products Inc. [4.10]. This device works by using a high frequency generator to produce a high potential at the electrode that ionizes the surrounding air, creating a localised plasma or corona. Since the plasma treatment is carried out in air at atmospheric pressure, there is no requirement for vacuum chambers and/or gas cylinders and therefore bonding can be achieved on any non-conductive surface. The wire electrode is passed across the sample at approximately 1 cm above the surface for approximately 10 seconds. The treated surfaces are then bonded together and left to rest for approximately one hour for bonding to take effect. The corona treatment is safe and easy to use, however some precautions do need to be observed. First, the corona produces a significant amount of ozone, and should only be used in an area with good ventilation. Secondly, the unit produces radio frequency (RF) noise, which has the potential to affect other equipment. The unit must be used on a non-conducting surface and should be kept at least three feet away from digital devices. Once the corona treatment is applied the surfaces must be immediately bonded as hydrophobic recovery can take place [4.11].

Figure 4.7 Completed PDMS structure

The completed PDMS structure is shown in Figure 4.7 photographed against a dark background so that the microfluidic structures can be seen. The structures were very time

consuming to make. They were also difficult to handle as PDMS is not a hard material. For these reasons PDMS was not used in the final design for the microfluidic channels for the sensing device. An alternative material was investigated and is presented in the next section.

4.2. Fabrication of PMMA Channels

Polymethylmethacrylate (PMMA), also known as Plexiglass®, is a light, shatter-resistant alternative to glass. It is cheap, readily available and easy to manufacture into microfluidic channels. This section will outline the fabrication of the microfluidic channels using an Epilog CO_2 laser ablation machine.

The PMMA microfluidic channels were first designed using the software drawing package, CorelDraw Graphics Suite as shown in Figure 4.8.

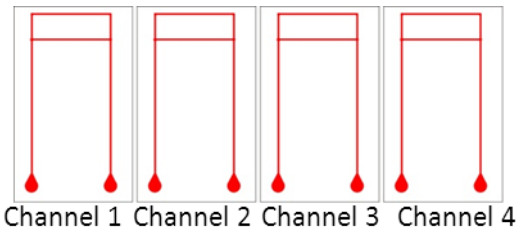

Figure 4.8 Four iterations of the original design transferred to CorelDraw for laser etch.

The resulting digital image of the channels is then sent to the Epilog CO_2 laser system [4.12], which utilises the ablation capabilities of the laser to engrave and cut a variety of materials. The laser system has two modes of operation, for which frequency, power and intensity of the CO_2 laser are parameters that can be adjusted for controlling the depth of ablation. In vector mode the laser moves along a straight line in the direction determined by the design. In raster mode the laser moves in a scanning pattern of parallel lines along the orientation of the digital design. These modes can be used individually or combined. Later in this chapter the effects of this type of engraving on the microfluidic channels were investigated. For the work presented here both modes are combined, the raster is used to form the channels and the vector is used to cut the channels into individual chips and create the holes for the inlet and outlet.

Two pieces of PMMA make up the channels with one piece containing the channels and the other used as a top cover with holes for the inlet and outlet. The PMMA is first placed into the Epilog laser system on the upper left corner of the printing table. The laser is then

manually focused using a manual focus gauge, shown in Figure 4.9, which determines the correct distance from the focus lens to the top of the material. The gauge is placed on the carriage, then the focus button on the laser is pressed and manually the table is moved up and down on the z-axis so that the tip of the gauge touches the top of the material.

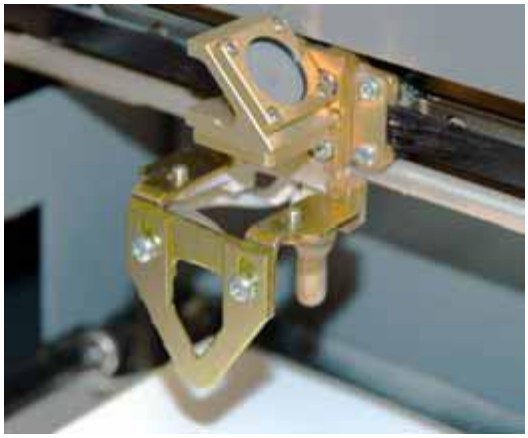

Figure 4.9 Focus gauge attached to lens and carriage system.

This focus distance is where the width of the laser beam waist is at its smallest. The carriage is then returned to its set point ready for printing. Parameters are then set for raster and vector modes on the Epilog dashboard as shown in Figure 4.10.

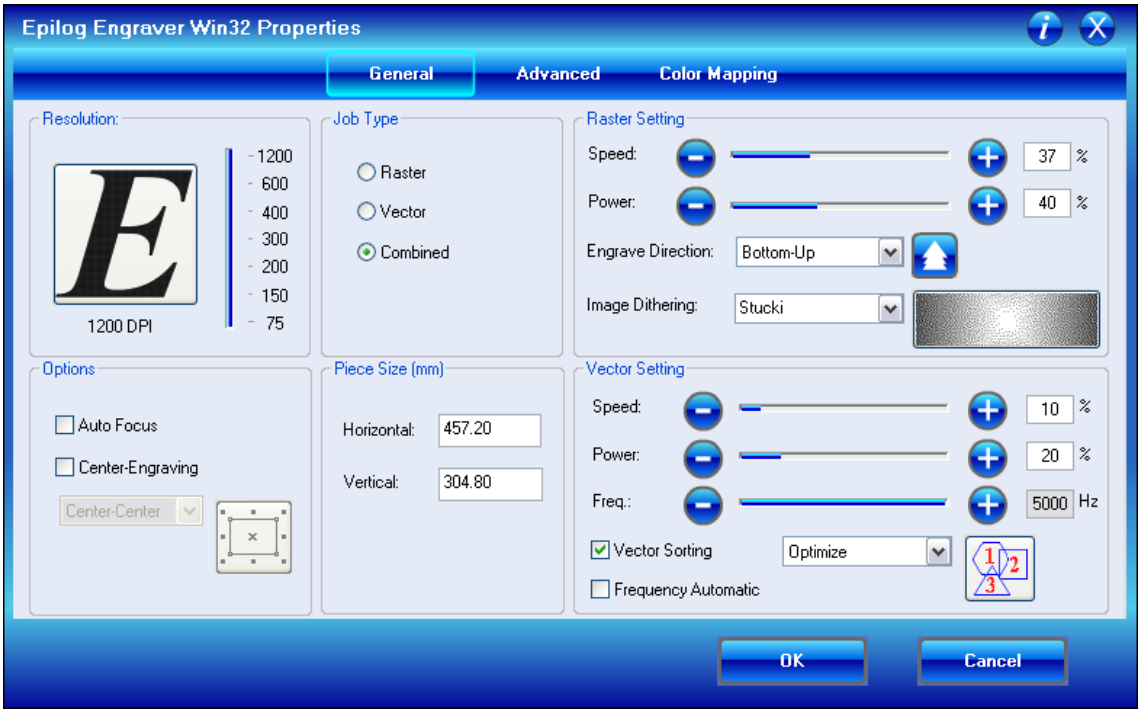

Figure 4.10 Epilog dashboard where settings are set for the laser ablation process.

The Epilog dashboard is the print driver that shows the setting of the laser functions from the computer and is the link that prints the data or image from the computer to the laser system. The resolution, or print quality, for all of the structures in this thesis was set to 1200 dots per inch (DPI). The raster and vector settings for each variation of chip design were chosen empirically based on the guidelines outlined in the operation manual. Once the pieces have been engraved and cut they are then cleaned and ready for bonding. The bonding technique used in this project is a heat and pressure treatment. The pieces are aligned manually and set between two glass slides; these are then inserted between two metal plates, which are pressed together. This set-up is then placed in an oven on a heat cycle from 0-160°C. A temperature of 160°C is then maintained for 40 min, and the temperature is then dropped down to 80°C and held for 30 min. The samples are then allowed to cool down to room temperature before removing them from the metal plates.

There were several designs of microfluidic channels using this PMMA process. The first design, used also in the SU-8 and PMDS fabrication processes, is illustrated in Figure 4.8. The microfluidic channels were fabricated on a 0.5 mm thick sheet of PMMA. The result of this design is shown below in Figure 4.11.

Figure 4.11 Initial design of PMMA microchannels based on the SU-8 design.

The microfluidic channels are then tested using an ink dyed water solution, to ensure there is no leaking. It was discovered that, in this design, the channels were too narrow and shallow to allow the fluid to flow. This was investigated using optical and scanning electron microscopy (SEM) techniques. The photographs in Figure 4.12 show the inlets of channels 1 and 2 and the ablation of the PMMA using the raster technique. There are defined grooves and steps as the laser moves from side to side and then up towards the straight channels.

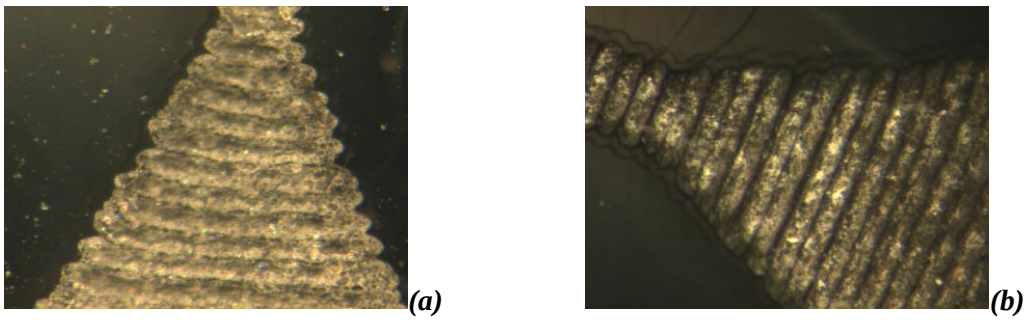

(a) *(b)*

Figure 4.12 (a) Optical micrograph of inlet of channel 1 (b) Optical micrograph of channel 2

Channel 1 was then put into the scanning electron microscope. Figure 4.13 shows the inlet of the channel at 100 and 300 times magnification.

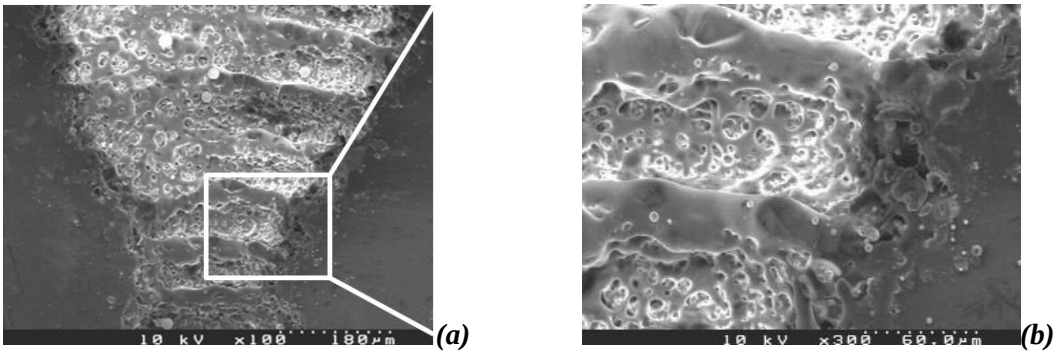

(a) *(b)*

Figure 4.13 Scanning electron micrograph of inlet of channel at (a)100 times (b) 300 times with white box indicating zone in (b)

The SEM photograph emphasises the ridges seen in the optical microscope. These ridges would hinder the flow of fluid from the inlet point. The following photographs shown in Figure 4.14 and Figure 4.15 present the microchannel spur.

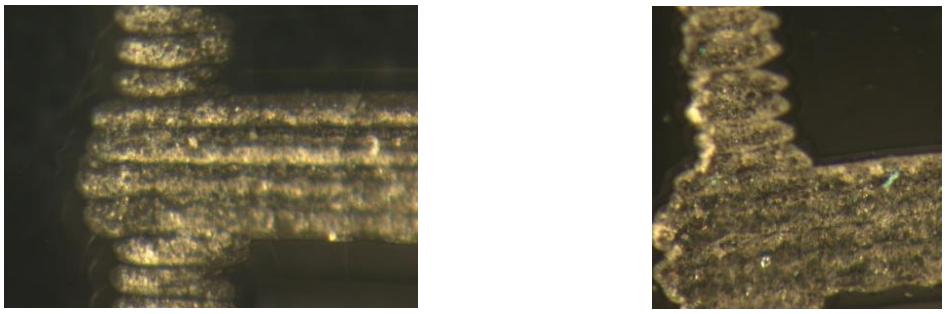

Figure 4.14 Optical micrographs of intersection of channel

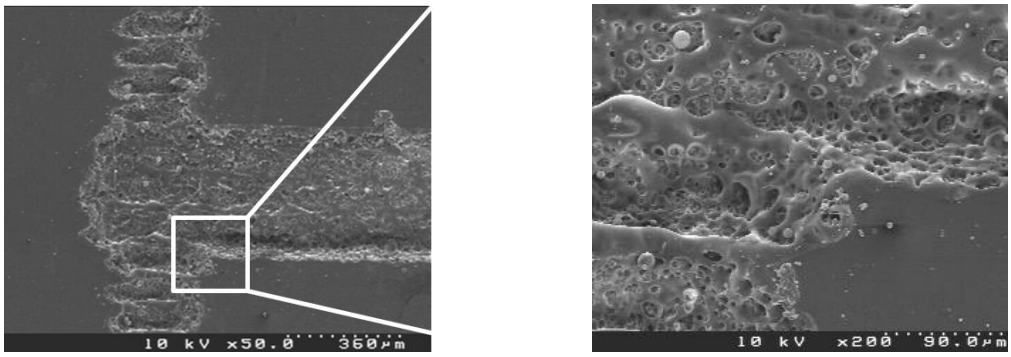

Figure 4.15 Scanning electron micrograph of intersection of channels at (a) 50 times and (b) 200 times with white box indicating the magnification area

Again detailed ridges are clearly seen in both the optical and SEM micrographs. The horizontal channel has less emphasis of these ridges due to the channel having a longer x dimension. This is also seen in the top corner of the channels as shown in the SEM image, Figure 4.16.

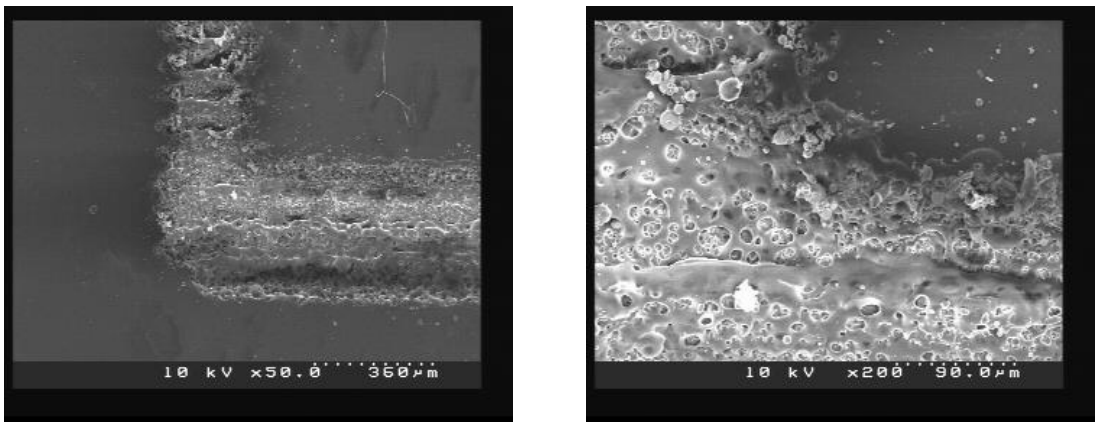

Figure 4.16 Scanning Electron Micrograph of top right corner of channel at (a) 50 times and (b) 200 times with white box indicating the magnification area.

These optical and SEM micrographs show the disadvantage of using PMMA laser ablation technique for small channels. In particular the raster technique that ablates the surface of the PMMA sheet causes deep ridges to be formed as the laser is moved in the y-direction. In addition, vapours can be trapped by the molten PMMA during resolidification resulting in randomly distributed micro bubble formations. Further examination of laser prototyping using PMMA has been described by M I Mohammed *et al [4.13]*.

As a result of the features obtained and shown by the SEM, the microfluidic channels were redesigned to accommodate for the roughness of the channel surfaces. In order to have automatic fluid flow, capillary pumps were also investigated.

The second microfluidic channel design incorporating a capillary pump is shown in Figure 4.17.

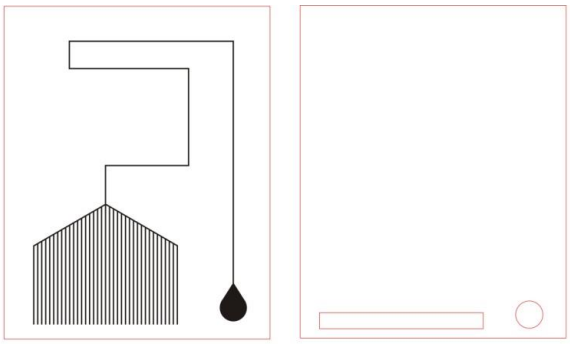

Figure 4.17 CorelDraw design of microfluidic channel design with multi-channel capillary pump and top cover

This design uses multiple channels as the pump. The principle behind this pump is to increase the specific area of the channels and multiply thereby the capillary effect to allow a passive way to circulate liquid in the main microchannel. The microfluidic channels have a width of approximately 300 μm. The Epilog laser parameters for this design are shown in the table below, Table 4.2.

Table 4.2 Epilog laser parameters for multi-channel capillary pump design [4.13]

Function	**Parameters**
Raster	Speed 20%
	Power 100%
Vector	Speed 10%
	Power 20%
	Frequency 5kHz

This design was printed on 0.8 mm thick PMMA and bonded using the heat and pressure technique. The microfluidic channels were first leakage tested by applying a water and dye solution and checking the surrounding area for any leaks. Once tested they were cleaned with water only and left to dry overnight. In testing this design it was found that the capillary pump was not efficient enough in delivering highly viscous samples and

took in excess of a day for complete saturation. For this reason another capillary pump design was chosen.

The third microfluidic channel design incorporated a capillary pump made with pillars as shown in Figure 4.18

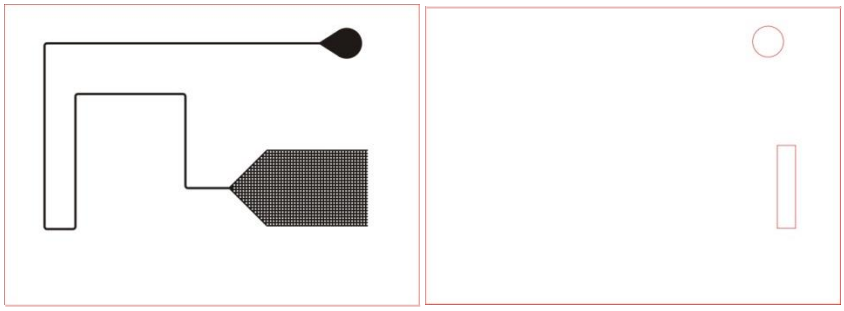

Figure 4.18 Pillar capillary pump microfluidic channel design in CorelDraw

This design uses the same principle as the multi-channel configuration, however horizontal channels cross the vertical ones to form a grid pattern, [4.13]. This allows a greater pressure difference between the inlet and outlet and therefore an increased flow speed. The channel was etched using the same parameters as the previous design and then bonded using the heat and pressure technique. Again the channels were leak tested using a water and dye solution. In testing the microfluidic channel design with the microwave resonant structure it was found that this design was impractical for this set-up. It was also discovered that the CorelDraw design did not take into account the over ablation of the laser and there was significant variation from chip to chip.

4.3. PMMA Laser Ablation Effects

4.3.1. Channel variations

Rapid prototyping using CO_2 laser system of PMMA results in large variations of channel width/depth and also deposits of melted PMMA. Using 5 different channels, measurements were taken slotting each individual channel into the waveguide slot. In the figure below, Figure 4.19, there is a clear, large variation between each of the channels. This could be due to the size of the individual channels, the bonding or more significantly misalignment of the microfluidic chip in the width of the slot within the microwave waveguide.

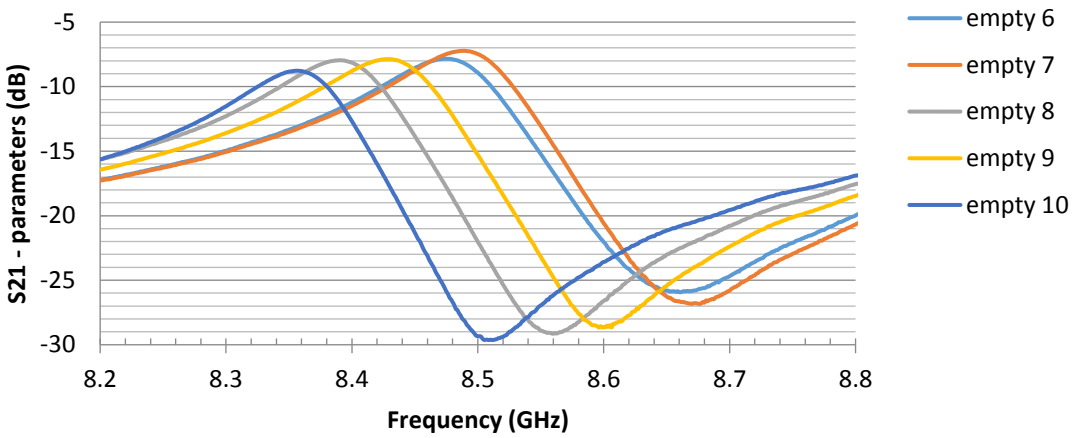

Figure 4.19 Variation between different channels

A study was performed in order to calculate the error associated with the variation with the microfluidic channel widths. Using a simple optical microscope with a backlight the variations in channel width are illustrated below in Figure 4.20. Four different points in the channel design were looked at to get a better representation of the channel width variation.

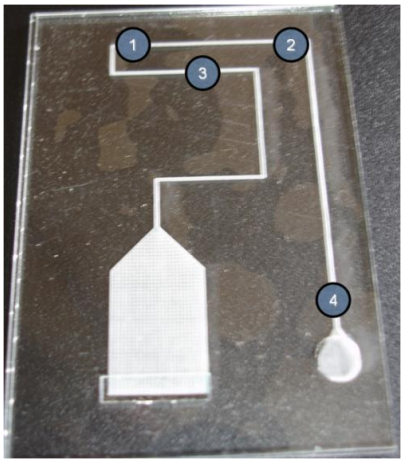

Figure 4.20 Positions of the measurements taken using the optical microscope

Points 1, 2, and 3 are of horizontal channels and point 4 is of a vertical channel. The optical images for a microfluidic chip are shown below in Figure 4.21.

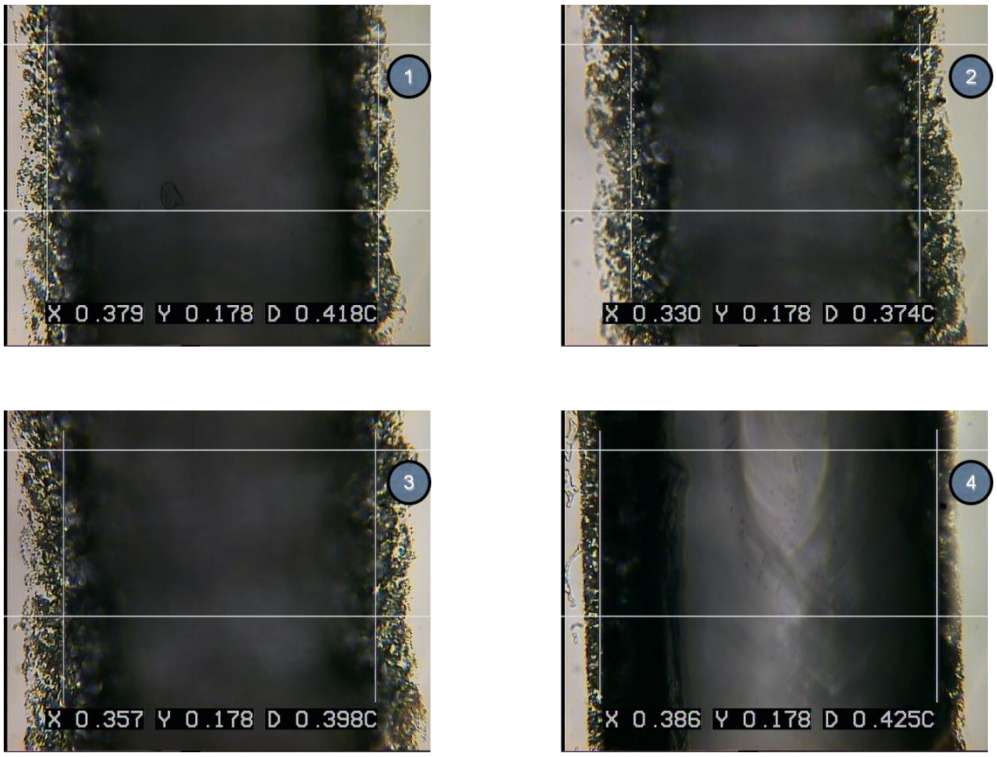

Figure 4.21 Optical measurements of the channel width, X, at various points along the channel

The optical microscope images quite clearly show a large variation ranging from 330 μm to 386 μm as far as the vertical and horizontal channel widths are concerned. This is due to the way the channels are fabricated using the CO_2 laser as illustrated in Figure 4.22.

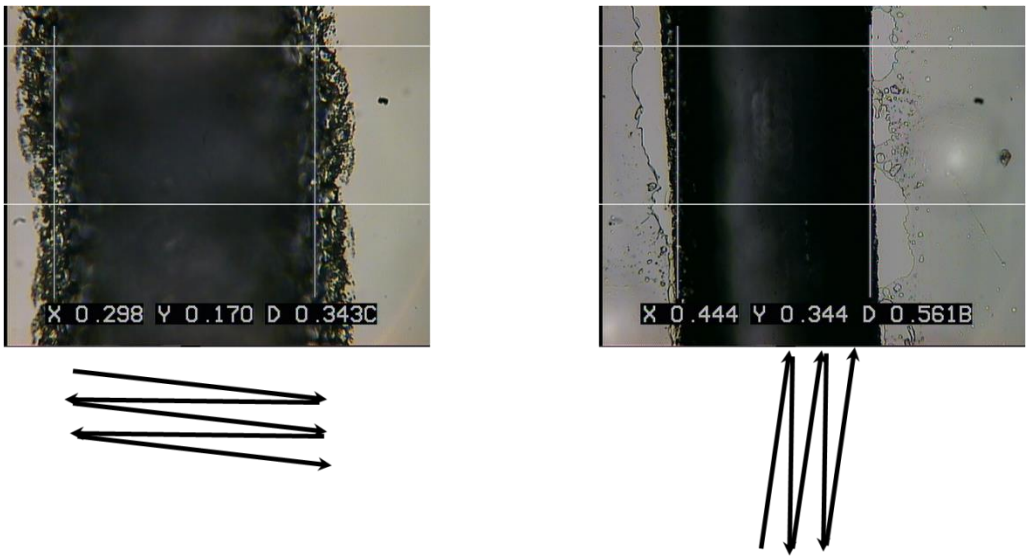

Figure 4.22 Direction of the laser ablation and its effect on the channel width

The arrows indicate the direction of the laser during the ablation of the channels; the vertical scanning of the laser beam causes the channels to be around 100 μm larger than

the horizontal channels. The channel widths for various channels (numbered 1 through 4) are shown in, Table 4.3, all sized in μm.

Table 4.3 Variation in channel width at various points on the channel with respect to the laser ablation

Channel	Size 1	Size 2	Size 3	Size 4	Average	Standard Deviation
1	379	330	357	386	363.00	21.85
2	325	337	352	444	364.50	46.89
3	298	279	325	417	329.75	52.96
4	340	341	331	400	353.00	27.41

As the results show there is significant variations in the various channels. The measurement setup was redesigned to make the system more reliable by incorporating pins to secure the microfluidic channel into the test structure. The microfluidic channels were also redesigned to eliminate variability in the pump rates and channel variation.

The fourth and final design used in the results is a non- capillary pump design shown in Figure 4.23.

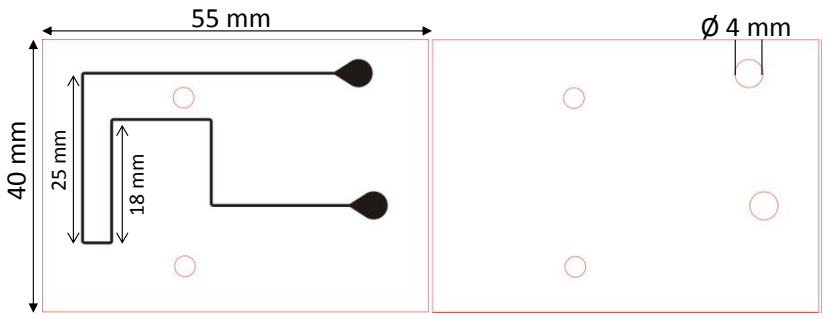

Figure 4.23 Microfluidic channel design with no pump. Fluid flow is provided mechanically.

The design shows the microfluidic channels with holes for the pins located in the waveguide. The microfluidic chips were again bonded using the same heat and pressure technique as the other channels. The laser parameters were also altered to accommodate for the over ablation of the channels by adjusting the power and speed of the laser, Table 4.4.

Table 4.4 Epilog laser parameters for microfluidic channel design with no pump

Function	Parameters
Raster	Speed 37%
	Power 40%
Vector	Speed 10%
	Power 20%
	Frequency 5kHz

Once the channels were sealed, nanoports that allow the connection to the mechanical pump, were glued onto one of the outlets of the channels as shown below in Figure 4.24.

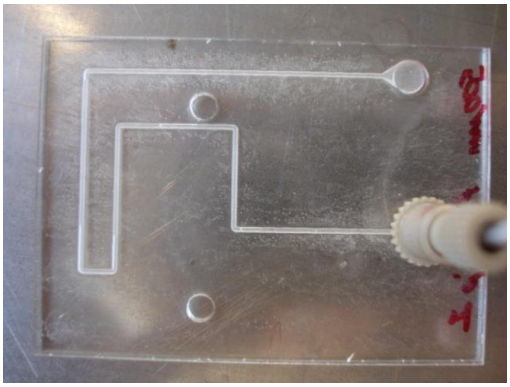

Figure 4.24 Microfluidic channels with a nanoport connection to mechanical pump

By attaching tubing the microfluidic channels can be filled using a syringe fixed to a mechanical pump device. This has the advantage of consistent fluid flow as well as no need to adjust the channels whilst inside the microwave waveguide. This was the final design used to capture the results in this project.

4.4. Design and fabrication of the microwave device

As discussed in Chapter 3 the E-plane filter was designed to have two apertures of different lengths. The material chosen for the E-plane filter was copper as it is a metal and therefore possesses a high conductivity. The material is also readily available and easily machined. The E-plane filter machined in copper, 1mm thick is shown in Figure 4.25.

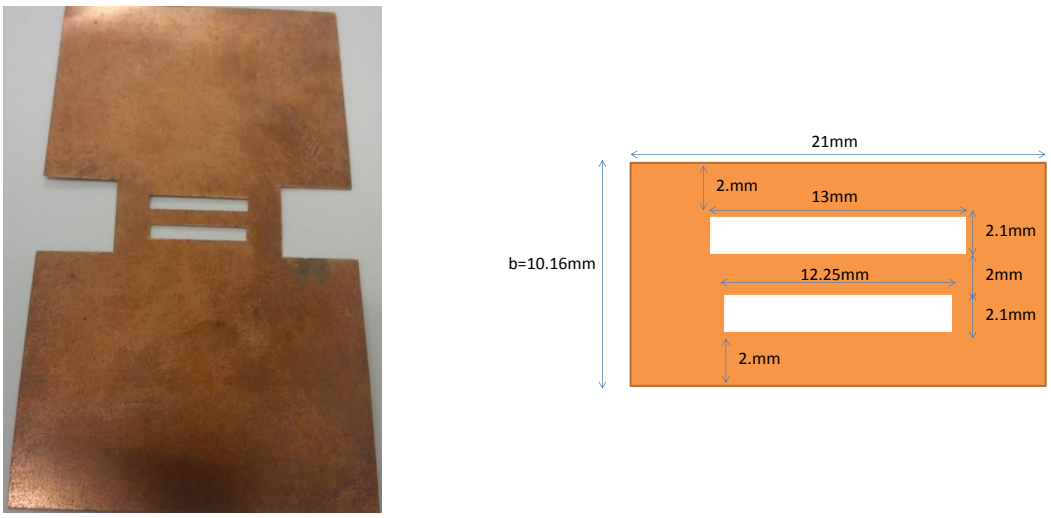

Figure 4.25 E-plane filter machined as designed in Chapter 3. Material is 1 mm thick copper.

The top aperture has a length of 13 mm and the bottom length has a length of 12.25 mm. The E-plane filter also has fins to enable the filter to be placed in the waveguide as will be shown later in this chapter. The waveguide was fabricated from a high conductivity material, in this case aluminium. Aluminium is a cheap, readily available material. The waveguide dimensions are that of the X-band standard, a= 10.16 mm and b= 22.86 mm.

As outlined in the previous section there were several problems with the liquid flow in the SU-8 microfluidic channels and thus a new thicker design was needed to accommodate the PMMA microfluidic channels. The higher slot was therefore necessary. The waveguide device is shown below.

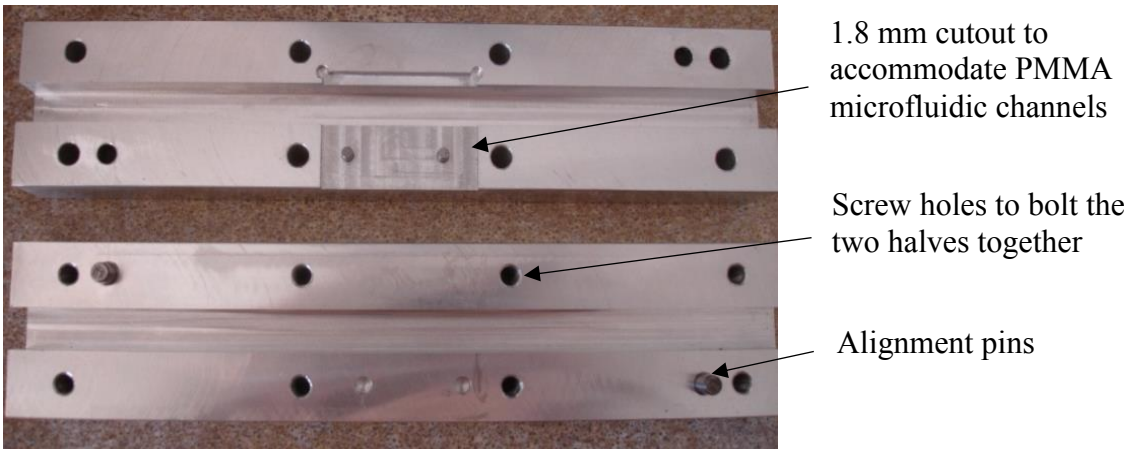

Figure 4.26 Microwave waveguide redesigned to incorporate PMMA channels

As the figure shows there was an aperture cut into on half of the waveguide device (upper half shown in the figure). This allowed the PMMA microfluidic channels to be incorporated into the sensing device. In order to prevent the microfluidic channels from

moving inside the waveguide, pins were also included. The complete waveguide setup, including the microwave filter and microfluidic channel is shown below in Figure 4.27.

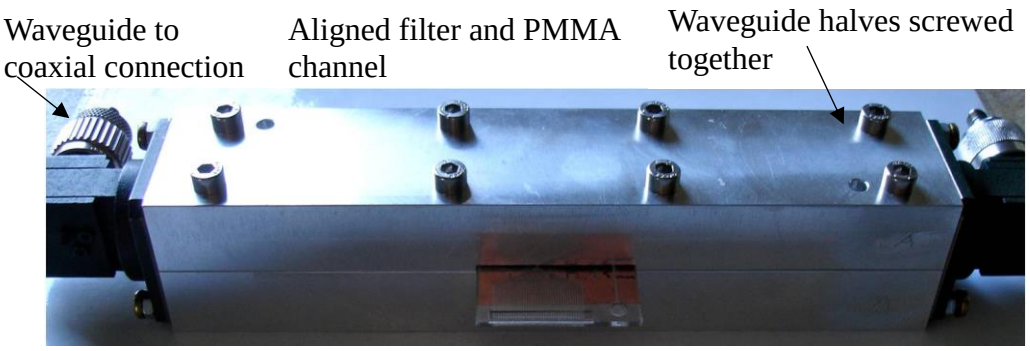

Figure 4.27 Waveguide with copper filter and PMMA microfluidic channel inserted.

4.5. Conclusions

Throughout this chapter different methods of fabrication of microfluidic channel devices were explored with the final selection of the PMMA material. This material is advantageous over SU-8 and PDMS as there is no requirement for a cleanroom facility, UV lithography or harsh chemicals. Compared to PDMS, PMMA is an easier material to manipulate as it is a rigid material and not a highly viscous substrate. PMMA is also biocompatible, easily machined and most importantly a low cost material. Using the CO_2 laser engraving system ensured high productivity and ease of manufacturing with high yield.

Table 4.5 Microfluidic Channel Material Comparison

Material	Fabrication	Advantages	Disadvantages	Thicknesses
SU-8	Clean room environment. Spin coating, UV Lithography, Hot plates/ovens for baking	High aspect ratio. Vertical side walls. Transparent	Laborious fabrication process requiring trained professionals.	1 - >200 µm
PDMS	2 part elastomer. Requires mixing, spin coating. Also requires a negative mould.	Once the mould is created, it can be used many times. Cheap.	Highly viscous making is difficult to work with.	5 - >200 µ
PMMA	CO2 laser ablation	Rigid material. Rapid prototyping with laser ablation	Rough side walls with CO2 laser ablation.	200 - >1000 µm

Also discussed was the fabrication of the microwave waveguide with e-plane filter. The waveguide had to be modified from the original design to accommodate the PMMA channels.

4.6. References

[4.1] O. Reynolds, "An experiemental investication of the circumstances which determine whether the motion of water shall be direct or sinuous, and of the law of resistance in parallel channels," *Philosophical Transactions of the Royal Society,* vol. 174, pp. 935-982.

[4.2] *Micronics Microfluidics, R & D Products, T-sensor*. Available: http://www.micronics.net/products/research-and-development/access-cards

[4.3] M. Zimmermann, H. Schmid, P. Hunziker, and E. Delamarche, "Capillary pumps for autonomous capillary systems," *Lab on a Chip,* vol. 7, pp. 119-125, 2007.

[4.4] *MicroChem Corp., Product SU-8 50-100, Data Sheet*. Available: http://microchem.com/Prod-SU82000.htm

[4.5] F. Ru and J. F. Richard, "Influence of processing conditions on the thermal and mechanical properties of SU8 negative photoresist coatings," *Journal of Micromechanics and Microengineering,* vol. 13, p. 80, 2003.

[4.6] J. C. Lötters, W. Olthuis, P. H. Veltink, and P. Bergveld, "The mechanical properties of the rubber elastic polymer polydimethylsiloxane for sensor applications," *Journal of Micromechanics and Microengineering,* vol. 7, p. 145, 1997.

[4.7] *AZ 400K Product Data Sheet*. Available: http://www.microchemicals.eu/micro/az_400k_developer.pdf

[4.8] F. Schneider, J. Draheim, R. Kamberger, and U. Wallrabe, "Process and material properties of polydimethylsiloxane (PDMS) for Optical MEMS," *Sensors and Actuators A: Physical,* vol. 151, pp. 95-99, 2009.

[4.9] *SYLGARD® 184 SILICONE ELASTOMER KIT Product Information.* Available: http://www.dowcorning.com/applications/search/products/default.aspx?R=131EN&country=GBR

[4.10] *Electro Technic Products Inc., BD-20 Corona Treater Manual*. Available: http://www.electrotechnicproduct.com/corona.html

[4.11] J. Kim, M. K. Chaudhury, and M. J. Owen, "Hydrophobic Recovery of Polydimethylsiloxane Elastomer Exposed to Partial Electrical Discharge," *Journal of Colloid and Interface Science,* vol. 226, pp. 231-236, 2000/06/15 2000.

[4.12] *Epilog Laser, Legend Series*. Available: http://www.epiloglaser.co.uk/legend_mini18.htm

[4.13] M. I. Mohammed, E. Abraham, and M. P. Y. Desmulliez, "Rapid laser prototyping of valves for microfluidic autonomous systems," *Journal of Micromechanics and Microengineering,* vol. 23, p. 035034, 2013.

5 E-plane Sensor: Experimental Results

The following section describes the results of the experimental work carried out on the sensing device. The results obtained are from the SU-8 and PMMA fabricated microfluidic channels with various sample solutions. The results from the PMMA experiments are then compared to the modelling results using HFFS software package as explained in Chapter 3. Samples include various alcohols, Ethanol and Methylated Spirit, and motor oils. Alcohols and Motor oils are freely available providing early data on the prototype device. Fast, reliable cell detection is required for medical diagnostics, therefore animal blood was also used to test the sensors ability to detect cells, namely Red Blood Cells (RBCs).

5.1 Sensor Results with SU-8 based Microfluidic Channel

The E-plane waveguide sensor and SU-8 microfluidic channels chip were aligned and set up as shown in Figure 5.1 below.

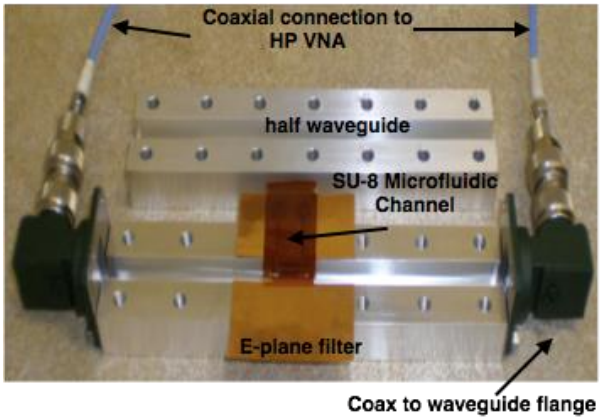

Figure 5.1 SU-8 microfluidic channel alignment with resonator and modified waveguide

The E-plane filter was placed into the custom designed half-waveguide. The SU-8 microfluidic channel was then aligned and placed on top of the E-plane filter. The other half of the waveguide was then screwed to the other half securing the filter and SU-8 microfluidic channels in place. The waveguide was then connected to a HP Vector Network Analyser (VNA) using coaxial to waveguide conversion flanges, as illustrated in Figure 5.1. The measurement system then needed to be calibrated before measurements could be taken. The calibration ensures that there are no additional losses due to the

measurement system, giving a true measurement of the waveguide sensor. The calibration process was carried out as follows:

- The frequency synthesizer was first switched on followed by the parameter test set and then the Vector Network Analyser (VNA). The frequency range for the test was chosen appropriately along with the number of test points within that range. For initial tests the frequency range was 7 to 12 GHz with 801 points. This was then narrowed to 1 GHz centred around the resonant frequency of the test with 801 points.
- The flanges from the test waveguide were connected to the parameter test set ports.
- On the VNA the CAL (Calibration) TRL368 (Through, Reflect, Line) option was chosen. This calibration uses a set of known standards for reducing the systematic effects of the measurement system, allowing a more accurate measurement of the device under test [5.1].
- For the first standard – 'Through' – the waveguide to coaxial flanges were connected together with no other transmission line. This sets the reference plane for the waveguide sensor measurements.
- The second standard – 'Reflect' – in turn each of the flanges were terminated with a reflection/short. This uses a different standard to also set the reference plane.
- The third standard – 'Line' – The flanges were connected to a short transmission line of know length. The S-parameters are measured and, together with the previous results, an error correction is applied.
- Once the calibration is complete it is validated by connecting the flanges together as the Through section of the calibration. There should be zero loss and no reflections.

Once the sensing device and the VNA were set up, an S-parameter measurement of the empty channel was taken. This is captured using the software Softplot®. This allowed communication between a PC and the HP VNA. Softplot® was able to capture the measurement data that can then be imported into Microsoft Excel®.

Results were also taken for the E-plane filter only. By measuring this, the effect of the microfabricated microfluidic channel can be observed.

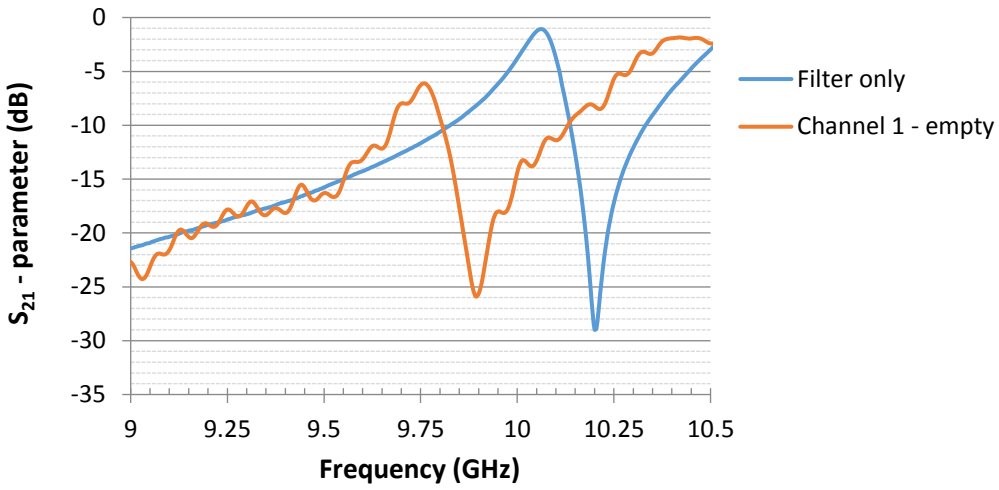

Figure 5.2 S_{21} parameter results of empty SU-8 microfluidic channel compared to the results of the E-plane filter only

As the results in Figure 5.2 show there is a significant difference between the resonant frequency of the filter only and that with the SU-8 microfluidic microchannel in place. This shift in resonant frequency can be used as an indicator that a change in dielectric constant is present. It is this phenomenon that will be exploited in this device once liquids are flowing through the microchannels. The shift in resonant frequency from the empty waveguide with just the E-plane filter is 302.5 MHz. An additional two empty SU-8 microfluidic channels were tested and the results are shown in Figure 5.3.

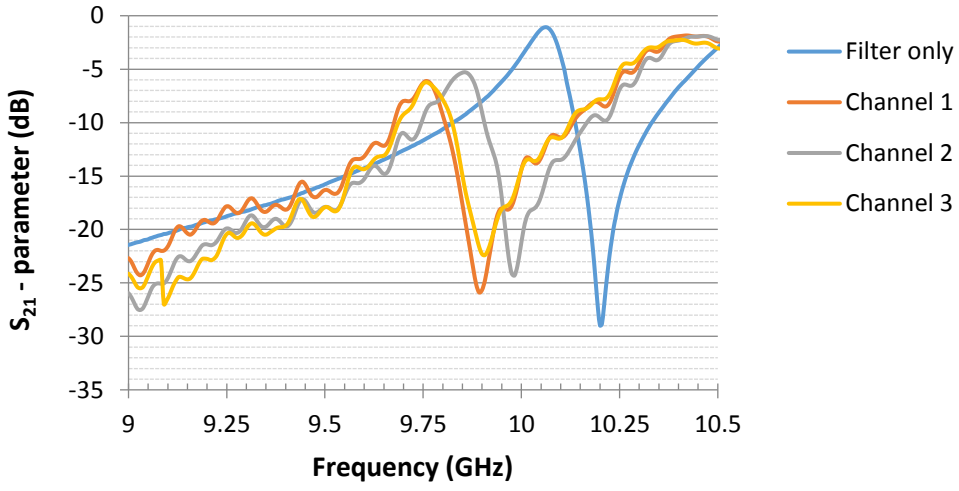

Figure 5.3 S_{21} parameter results of different empty SU-8 microfluidic channels. The signature of the E-plane filter only is given as a reference.

Although the general shape of the curves looks similar, there are discrepancies between the three SU-8 microfluidic channels. This could be attributed to the variations in the SU-8 mixture that is formulated in house as mentioned in Chapter 4. It could also be due to the placement of the microfluidic chip within the waveguide. All curves have however resonant frequencies distinct from that of the E-plane filter only. In order to investigate further, different liquid samples were introduced inside the microfluidic channels.

The first sample was a solution called phosphate buffer saline (PBS). This is an isotonic water based salt solution for suspending biological cells. The PBS sample was introduced by pipetting a small droplet onto the inlet of the SU-8 channels. Due to capillary forces at the interface of the microfluidic channel the fluid was able to circulate to the outlet of the device. The results for the PBS filled channels are shown in Figure 5.4.

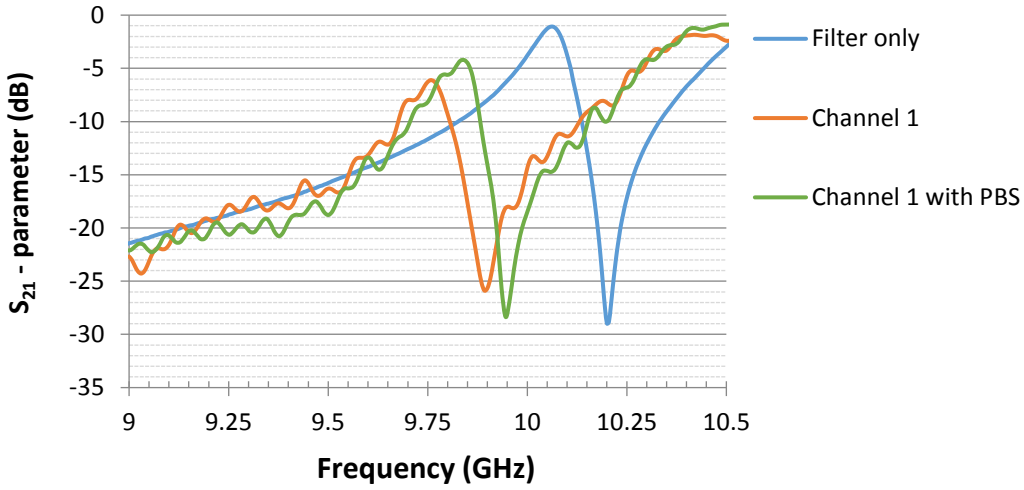

Figure 5.4 S_{21}-parameter results of SU-8 microfluidic channels, Channel 1 with PBS sample, compared to that of the empty channel and E-plane filter only

As the results in Figure 5.4 show, the resonant frequency has shifted compared to that of the empty channel. The shift is approximately 84.8 MHz. The microfluidic channel was then flushed with air using a syringe positioned at one of the inlets. The SU-8 microfluidic channel could not be adequately cleared of the initial solution therefore could not be used for more than one sample. As discussed in Chapter 4 the SU-8 microchannels were difficult to fabricate and as they could only be used once it was decided to investigate an alternative substrate for the microfluidic channels.

Polydimethylsiloxane (PDMS) was the next alternative, however as discussed in Chapter 4 Design and Fabrication of E-Plane Sensor the material did not yield suitable

microfluidic channels for this device. The final material for the microfluidic channels investigated for this device was Polymethylmethacrylate (PMMA). The results for this material are described below.

5.2 Sensor Results with Single Layer PMMA Microfluidic Channel

After discovering the difficulties in using SU-8 and PDMS, PMMA was then used to fabricate the microfluidic channels. This is described in the Chapter 4 Design and Fabrication of E-plane Sensor. PMMA, also known as Plexiglas®, is a plastic material that is cheap, readily available and easy to manufacture using a CO_2 laser system. Tests were carried out on the 0.5 mm thick PMMA to machine microfluidic channels. Due to the method of laser etching and the thickness of the PMMA, it was however difficult to obtain accurate measurements. The sample fluid did not flow as discussed in Chapter 4. The thickness of the channel did not allow the halved waveguide to completely close, causing a gap resulting in high losses. Therefore the PMMA channel design and waveguide were modified as discussed in Chapter 4 and the following sections.

5.3 Sensor Results with Capillary Pump PMMA Microfluidic Channel

As discussed in Chapter 4 the channels and original waveguide were modified to accommodate the extra thickness of the PMMA material as shown in Figure 5.5.

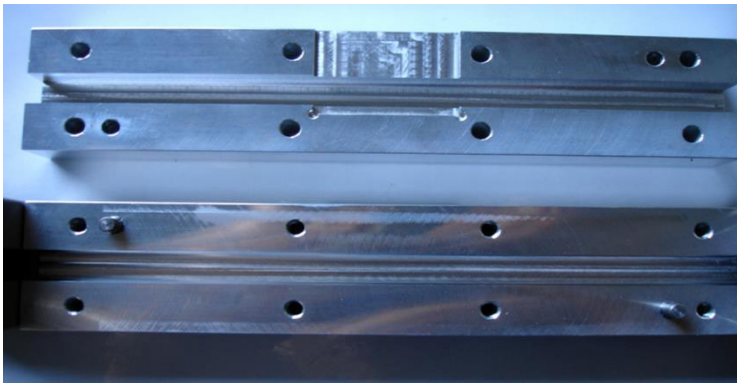

Figure 5.5 Picture of modified waveguide to accommodate the thickness of PMMA channels

The PMMA microfluidic channels with the capillary pump design, shown in Figure 5.6, were then inserted into the waveguide. The waveguide was then set-up and calibrated as described above. The test fluid was delivered using a syringe. A small droplet was placed at the inlet of the microfluidic channel. This fluid was then drawn into the rest of the

channel by capillary action. The fluid could be extracted using a vacuum suction technique and could therefore be used multiple times.

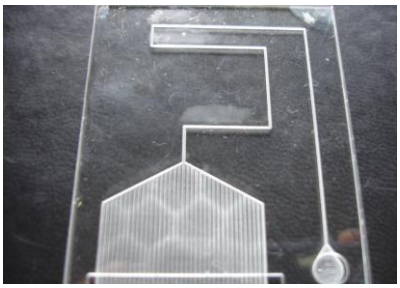

Figure 5.6 Microfluidic channel with capillary pump design

An initial experiment was carried out using the capillary pump design with concentrations of ethanol in water. The same microfluidic chip was used throughout the test. The first sample introduced to the microfluidic channel was 100% ethanol. This was then diluted in volumetric concentrations of 80%, 60%, 40%, and 20% with deionised (DI) water. The last sample was 100% DI water. After each solution the channels were manually flushed using the natural capillary forces of the microfluidic channel. The results of the tests with varying concentrations of ethanol in DI water are shown in Figure 5.7.

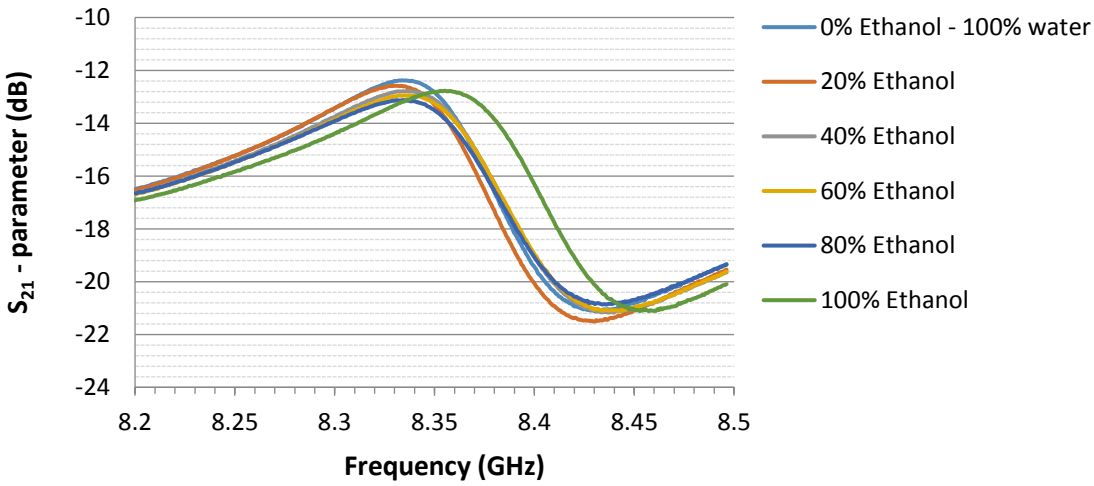

Figure 5.7 Results obtained with different concentrations of ethanol in water

As the results show, there is a significant shift in the resonant frequency between the 100% water and 100% ethanol. By introducing water into the ethanol, the resonant frequency is fairly constant. This suggests that water has a stronger effect on the dielectric constant of the solution than ethanol. As more and more water is introduced the losses associated with this solution lessen.

Blood comprises many components such as Red Blood Cells (RBCs), White Blood Cells (WBCs) and plasma. In order to test this device for possible clinical applications, animal blood was used which has been separated into the components of red blood cells and plasma. The red blood cells are diluted into different concentrations with phosphate buffer saline (PBS). Figure 5.8 shows the frequency variations of the return loss parameter, S_{21}, for red blood cells and plasma of mouse blood compared to empty channels (channels 1 and 2 on the graph). As these are blood samples, separate channels for each sample must be used to ensure that there is no cross contamination.

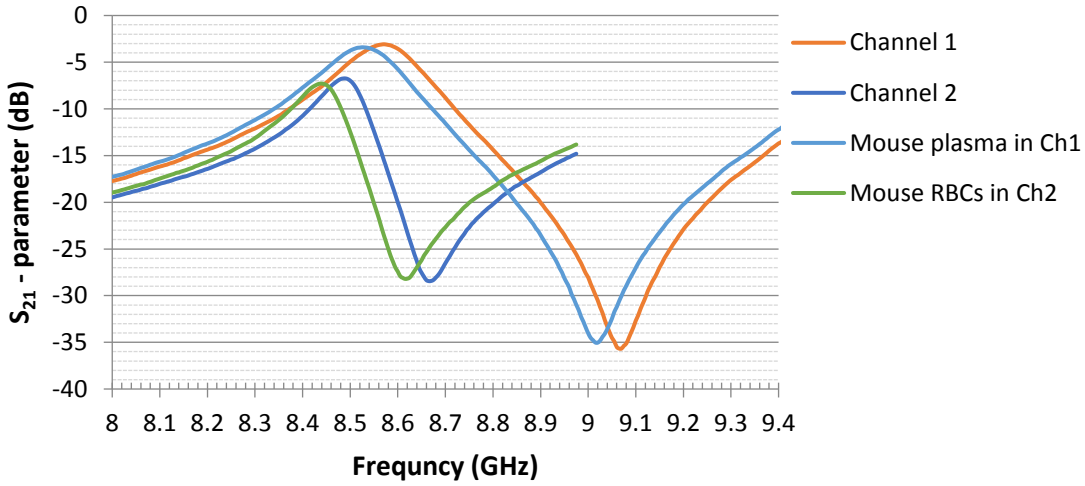

Figure 5.8 S_{21} parameter results of mouse blood samples in 2 separate channels. Channel 1 sample - mouse plasma. Channel 2 sample - mouse red blood cells suspended in PBS 500:1

The figure shows a shift in resonant frequency with each respective empty microfluidic channel and their sample. However it is also clear that there are inconsistencies in the placement or alignment of each of the different channels resulting in mismatched frequency responses. This was exacerbated through the use of the pipetting technique to deposit the samples disturbing the alignment of the microfluidic channels with the e-plane filter apertures. This is investigated in the next section. Also, the resonance frequency difference for each of the samples is relatively close meaning that this measurement is not capable of differentiating plasma from red blood cells.

5.3.1. Investigation into the reproducibility of the results with the capillary pump PMMA Microfluidic Channels

Problems with movement of the microfluidic channels in the cavity slot were investigated. Using different channels, comparisons were made of the air filled channel with the channel filled with phosphate buffer saline (PBS). Four microfluidic channels were fabricated and sealed using the techniques described in Chapter 4. The waveguide and VNA were set up as described before. Each of the microfluidic channels was inserted into the slot in turn. A measurement of the empty channel or air-filled and with a sample of PBS was taken for each channel and the results are shown below in Figure 5.9.

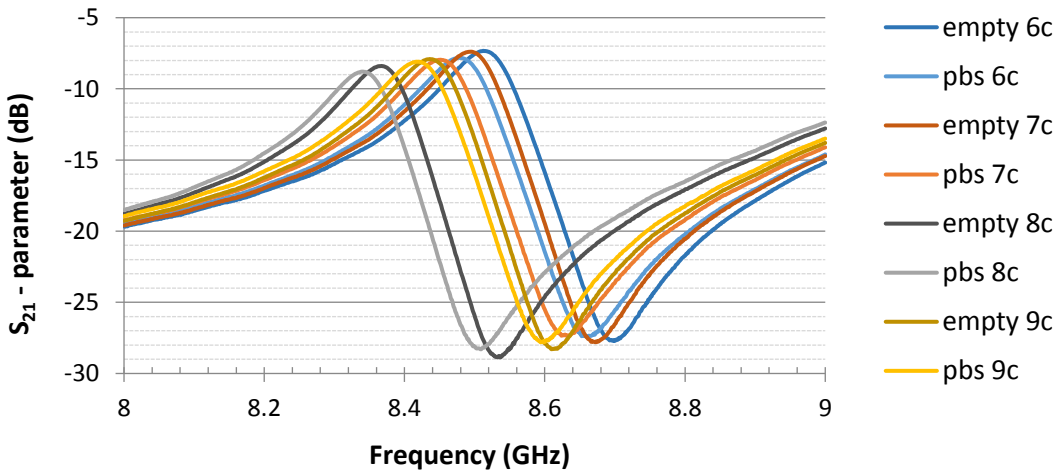

Figure 5.9 S_{21} parameter measurements of four microfluidic channels - air filled and PBS filled.

The results show a difference in resonant frequency compared to air and PBS. There is also a difference in each of the microfluidic channels due to instability when placed in the waveguide structure. Using one microfluidic channel, S_{21} parameter measurements were taken after inserting then removing the channel several times. The results are shown in Figure 5.10.

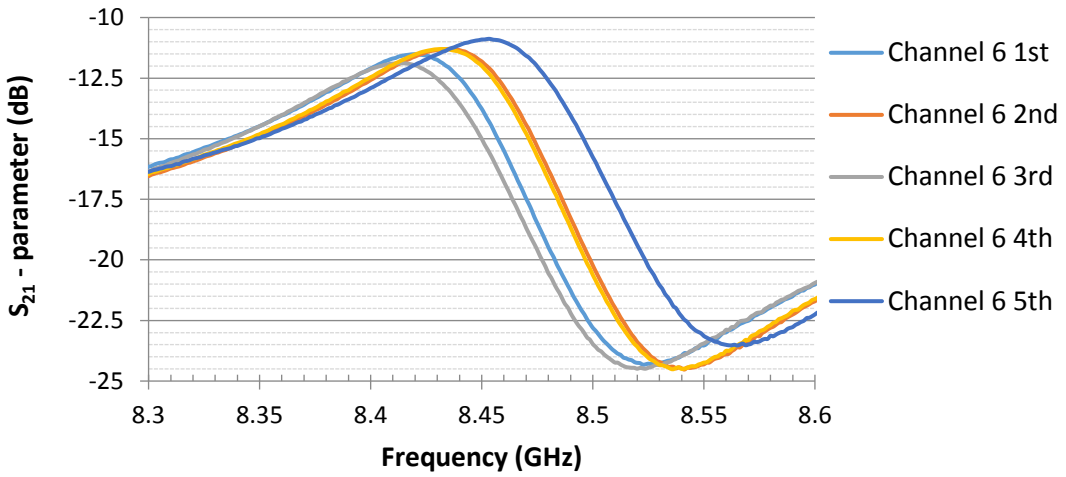

Figure 5.10 Repeatability test by removing and inserting the microfluidic channel several times

Variations of the order of 70 MHz for the minimum of S_{21} and 40 MHz for the maximum of S_{21} are obtained for the same channel. Considering that a change of around 30 MHz is obtained in the shift of the resonant frequency between a filled and empty channel, it is clear that the use of such devices proves to be difficult at times. This is due to the shift in alignment with the e-plane filter. S_{21} parameter measurements were then taken with the microfluidic channel kept in place. Three repeated measurements are shown in Figure 5.11.

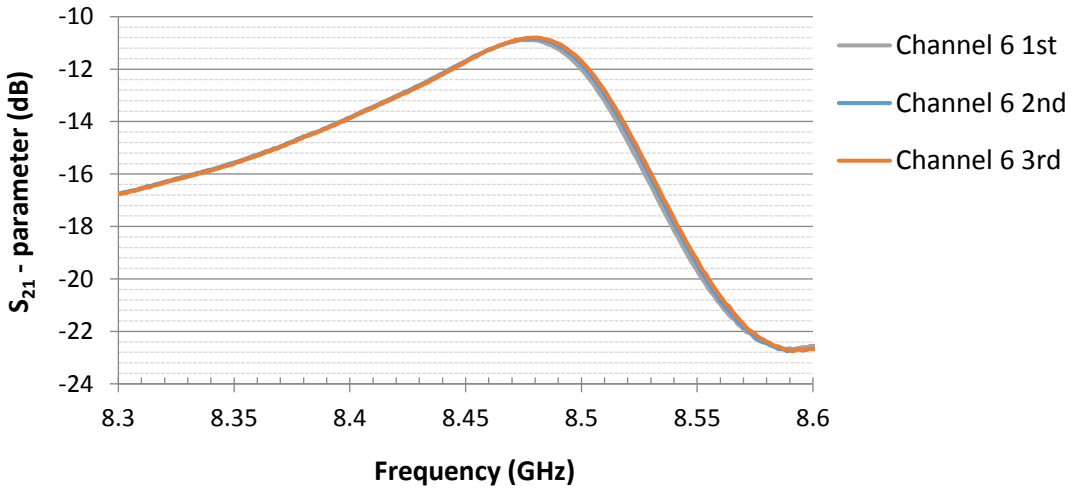

Figure 5.11 Repeatability test with a fixed channel

There is very little shift in the overall trace including the resonant frequency.

5.3.2. Oil Experiments

Before each experiment a through reflect line (TRL) waveguide calibration was carried out. An empty channel is then inserted into the waveguide and aligned with the resonator. For each of the experiments, six measurements were taken for each sample.

Motor Oil

Comparison between an air filled channel and Halfords 5w-40 motor oil was made in terms of S-parameter measurements. An average over the six measurements was made.

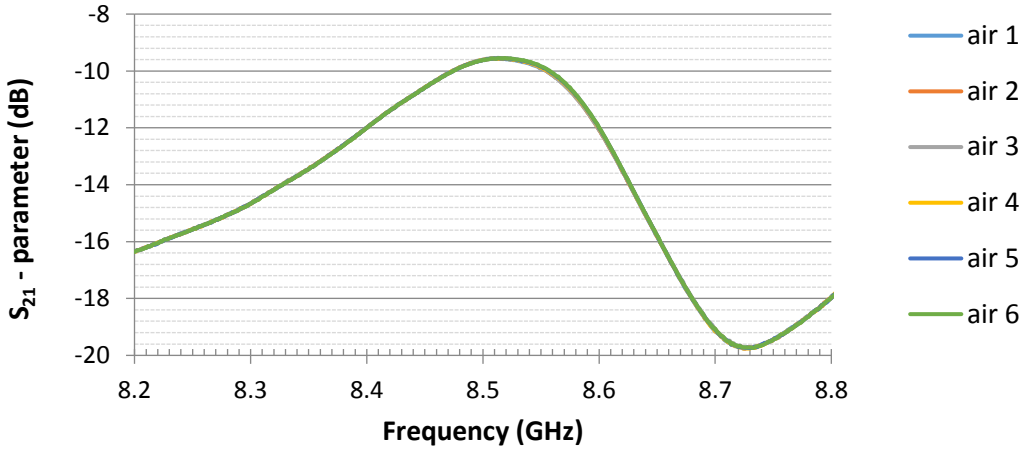

Figure 5.12 S_{21} parameter measurements of a single air filled channel

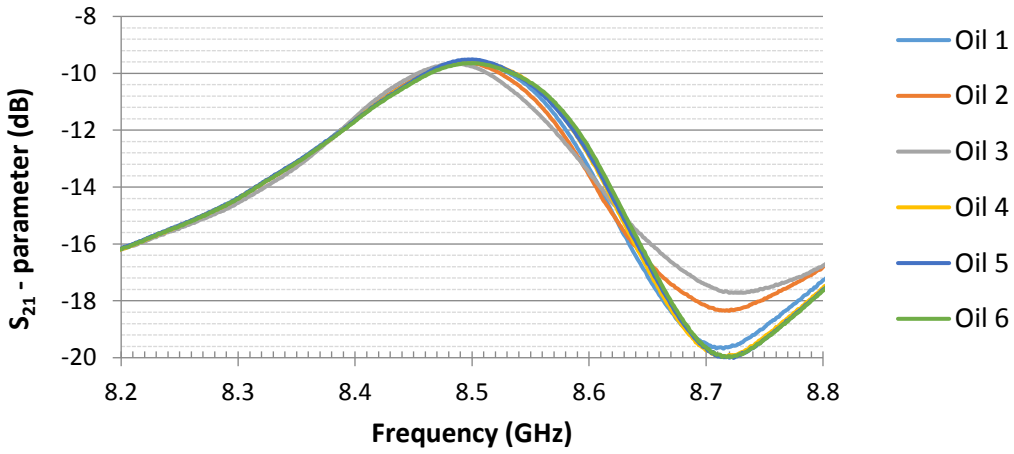

Figure 5.13 S_{21} parameter measurements of a single microfluidic channel filled with oil sample

The repeatability of the measurements for the air filled channel is very consistent. However the motor oil measurements show some discrepancy due to the movement of

the channel within the waveguide as the oil is syringed into the channel. Taking an average of these results can determine if a shift in resonant frequency is observed between the empty channel and the oil.

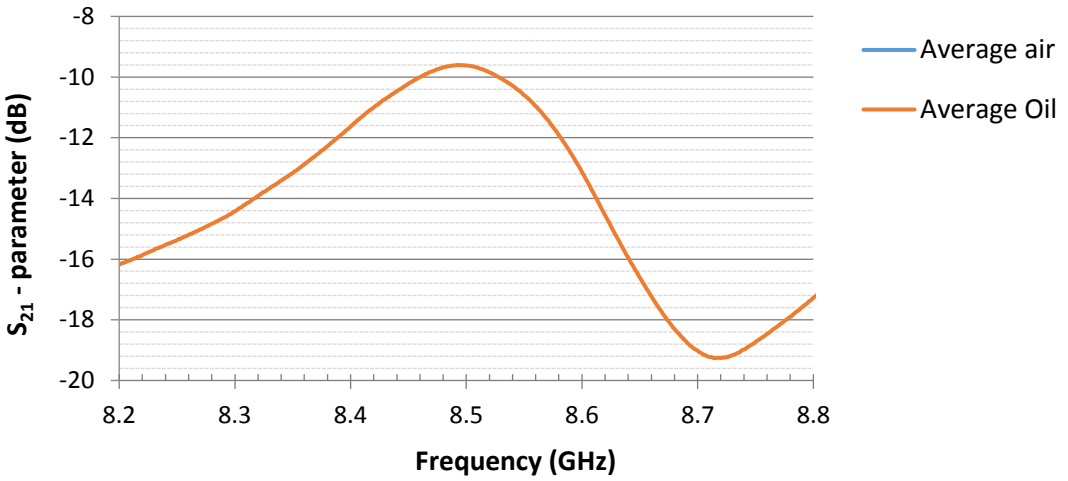

Figure 5.14 Comparison of average S_{21} parameter results of air and oil

As the results show we can see a slight shift in the resonant frequency of approximately 21 MHz.

Vacuum pump oil

In this experiment a repeatability test against an air filled channel was carried out using vacuum pump oil. Again six measurements of each of the samples were taken and the results are shown below.

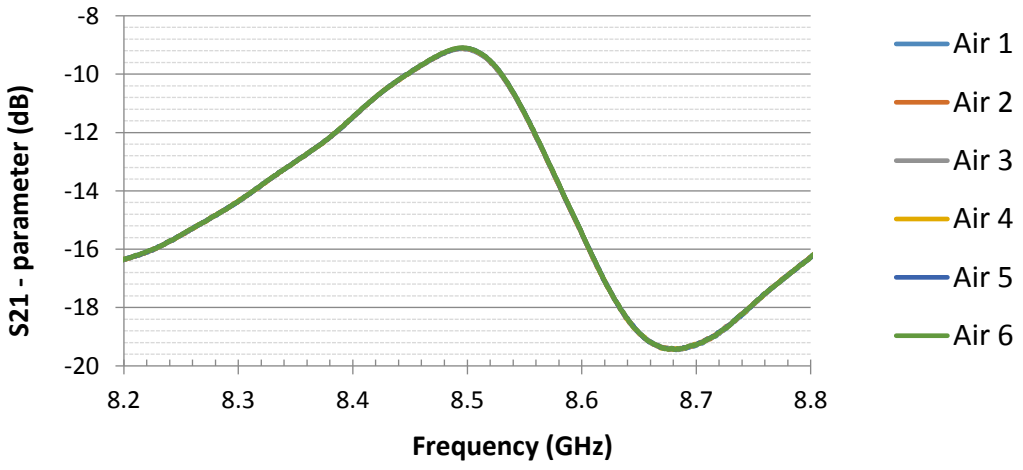

Figure 5.15 Repeatability of S_{21} parameter measurements of an air filled microfluidic channel

As the results show the repeatability of the vacuum pump oil is significantly better than that of the motor oil. This is due to the immobilisation of the channel with the waveguide by using pins. Another point to note is the change in bandwidth from the previous results; this is due to the movement of the E-plane resonator from this previous position when the waveguide was dismantled after the initial experiment. Therefore a way to fix the resonator to the waveguide is essential in maintaining repeatability. A graph comparing the average S_{21} parameter results of the air and vacuum pump oil are shown in Figure 5.16.

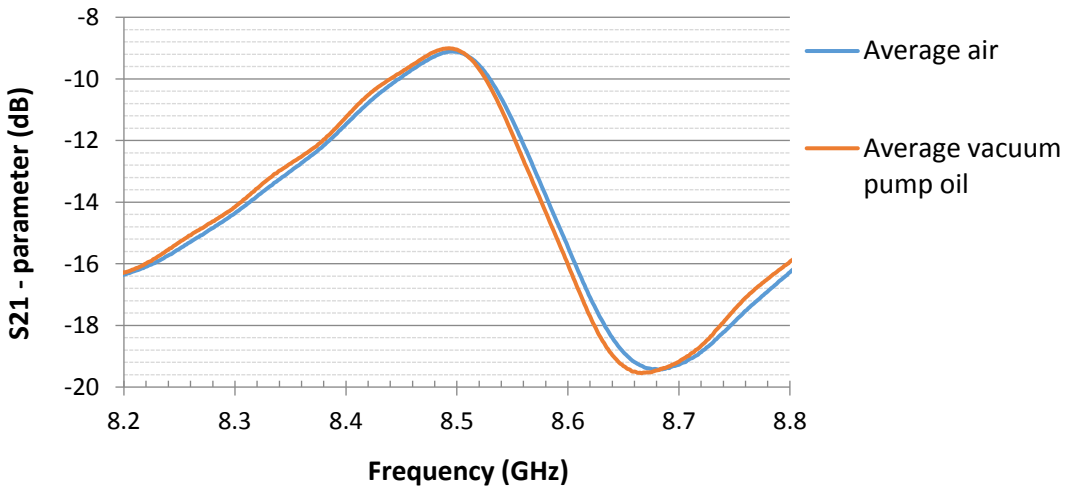

Figure 5.16 Average S_{21} parameter measurements of air and vacuum pump oil

The resonant frequency shift in these results is only 4 MHz; this could be due to air bubbles appearing in the channels as this is a highly viscous oil.

Evidently this is a very sensitive device. In order to stabilise the measurements the E-plane resonator need to be permanently fixed. The microfluidic channels must also be stabilised during the experiments. These were achieved by aligning the e-plane resonator in its optimum position and closing the waveguide by using all of the available screw terminals. The microfluidic channel was redesigned as discussed in Chapter 4 to include ports to secure the channel to a mechanical syringe pump. This ensures that the microfluidic channel is not disturbed when introducing the sample. The following section provides details of the new set-up to minimise disturbances as well as the results achieved using this set-up.

5.4 Results using mechanical pump design

In order to ensure the repeatability of the measurements a mechanical pump was introduced to avoid any movement of the microfluidic channel or surrounding equipment. The microfluidic channels were redesigned as discussed in Chapter 4, Figure 4.23. A nanoport is connected to the inlet of the channel to allow the connection of tubing that is then attached to a syringe. The syringe is operated by the mechanical pump allowing constant accurate flow of the test fluid. The measurement set up is shown in Figure 5.17 below.

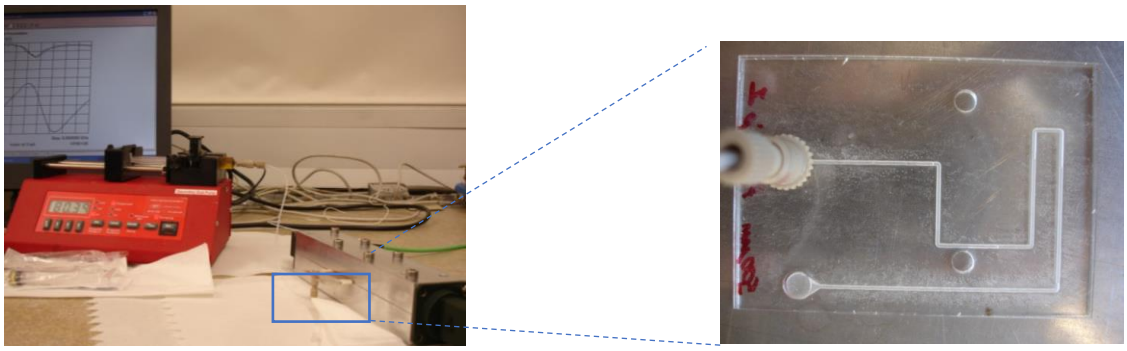

Figure 5.17 Mechanical pump measurement set-up and detail of the PMMA Microfluidic channel with nanoport connections to mechanical pump

The waveguide is connected to the HP Vector Network Analyser and calibrated as before. S-parameter measurements were then captured by the software package Softplot.

5.4.1. Oil with a contaminant

Motor oil 5W/40 was employed and contaminated with alumina particles of 3 μm diameter at a concentration of 1 M. The sample was compared to DI water and pure oil. The results are shown in Figure 5.18.

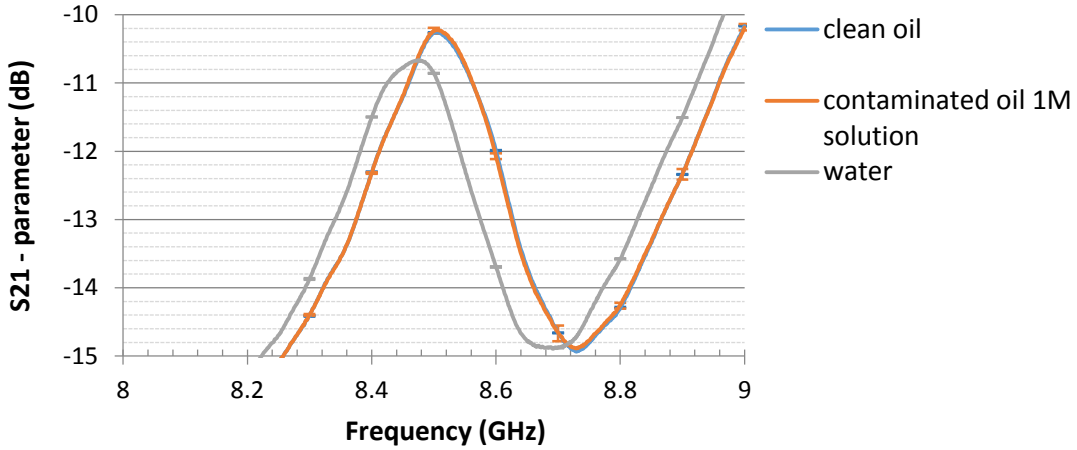

Figure 5.18 Average S_{21} parameter results of water and oil contaminated with alumina particles.

Taking an average of 5 measurements and measuring the y-error associated with the variability of the measurement, it is not possible to distinguish differences between clean and contaminated oil at this concentration. The dielectric constant for Alumina is given as 9.8 at 1 MHz [5.2]. The dielectric constant of oil is between 2.1 and 2.8 at 100 kHz [5.3]. The contamination is thought to be too small for the sensor to register a change in the dielectric constant of the solution. Repeat measurements with higher concentrations of alumina particles were not possible as the particles settled in the solution and in the microfluidic channel.

5.4.2. Different oils compared with water

The following measurements are of the same kind as those carried out using the capillary pump microfluidic device. In repeating these measurements comparisons can be made between the different characteristics of the different oils compared to that of water. Results are presented in Figure 5.19.

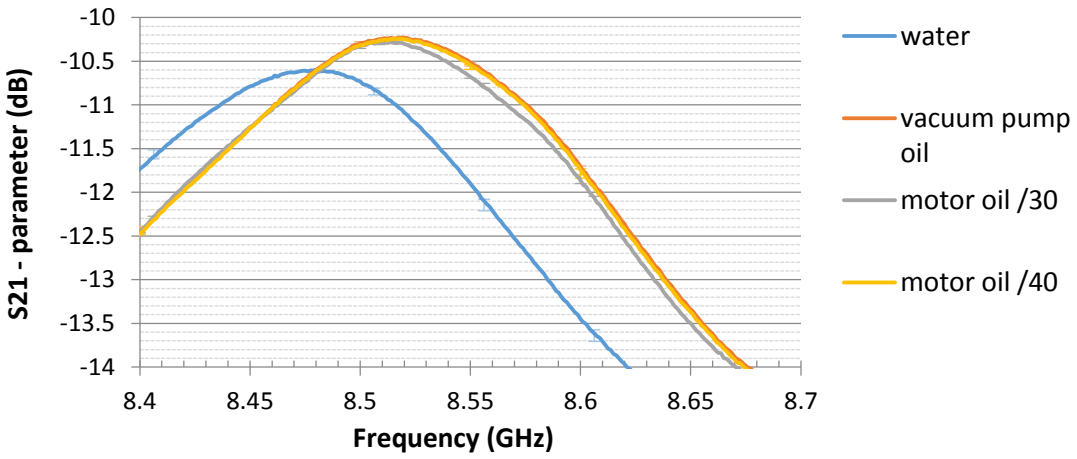

Figure 5.19 S_{21} parameter measurements of various oil samples compared to deionised water

It is clearly shown that there is a distinction between the oils and the water. The difference between the different oils is not apparent. Therefore a closer look at the resonant feature is necessary; the result is shown in, Figure 5.20. In the left figure the S_{21}-paramter y-axis error bars are displayed. In the right figure, the frequency x-axis error bars are shown for the different kinds of oils. The graphs show the resonant feature of the averaged results for the oils over 5 runs. The figure on the left displays the maximum deviation from the average of the S21-parameters around the resonant frequency. The figure on the right displays the maximum deviation from the average resonant frequency over the five tests. By observing the overlap in the errors associated with the vacuum pump oil and the motor oil /40, there can be no clear distinction in the sensors response. This suggests that the vacuum pump oil and the motor oil /40 have similar dielectric characteristics. However the errors associated with the motor oil /30 show no overlap with the other traces. Therefore the sensor can distinguish between the motor oil /30 and the motor oil /40.

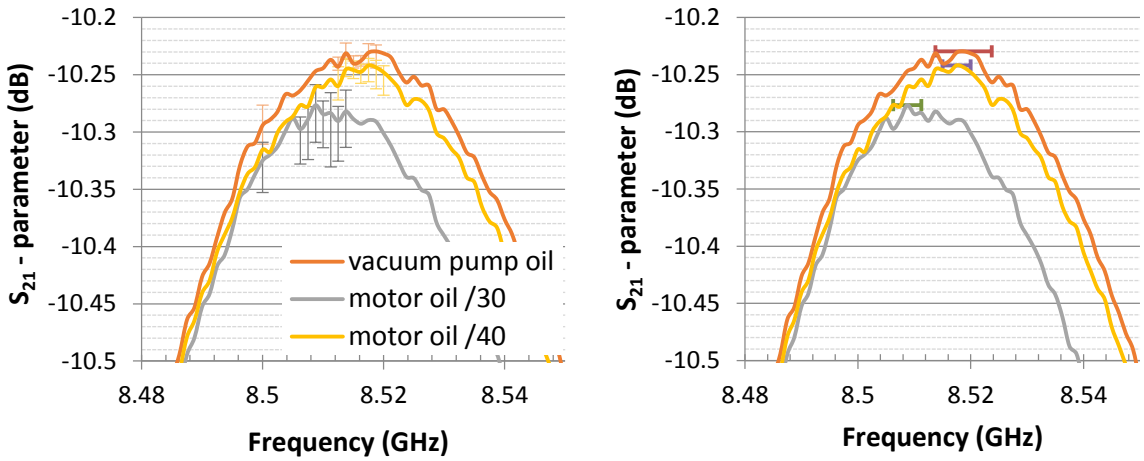

Figure 5.20 Left – Average return loss of various oil samples showing the error in the S_{21}. Right – Average return loss showing the error in the resonant frequency.

In order to further understand these results the resonant frequency of each sample is given in the table below, Table 5.1.

Table 5.1 Resonant frequency and S_{21}-parameters of samples

	Water	Vacuum pump oil	Motor oil /30	Motor oil /40
Resonant Frequency (GHz)	8.478	8.516	8.512	8.516
S_{21}-Parameters (dB)	-10.599	-10.223	-10.290	-10.242

As the results show the vacuum pump oil and the motor oil /40 resonant frequencies overlap. There is a resonant frequency difference between the motor oil /30 and motor oil /40 of 4 MHz.

5.4.3. Methylated spirit and water concentration measurements

In order to determine the sensitivity of the device, measurements were taken of various concentrations of methylated spirit with water. The average over 5 results was taken and plotted as shown in Figure 5.21.

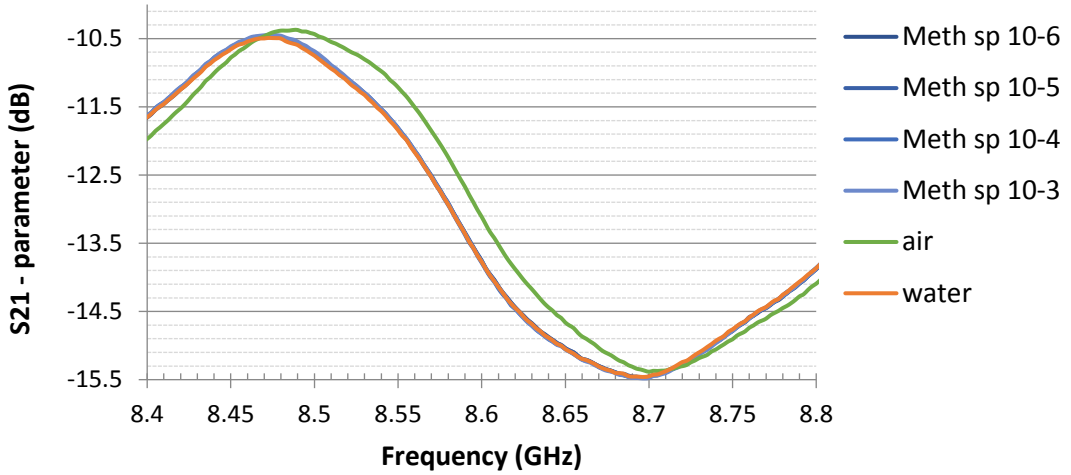

Figure 5.21 Average S_{21} parameter measurements of concentrations of methylated spirit and water

From the frequency range of 8.4 GHz to 8.8 GHz there is little difference between each of the curves when the channels are filled with liquids. A closer look at the resonant frequencies of each of the constituents is therefore needed as shown in Figure 5.22.

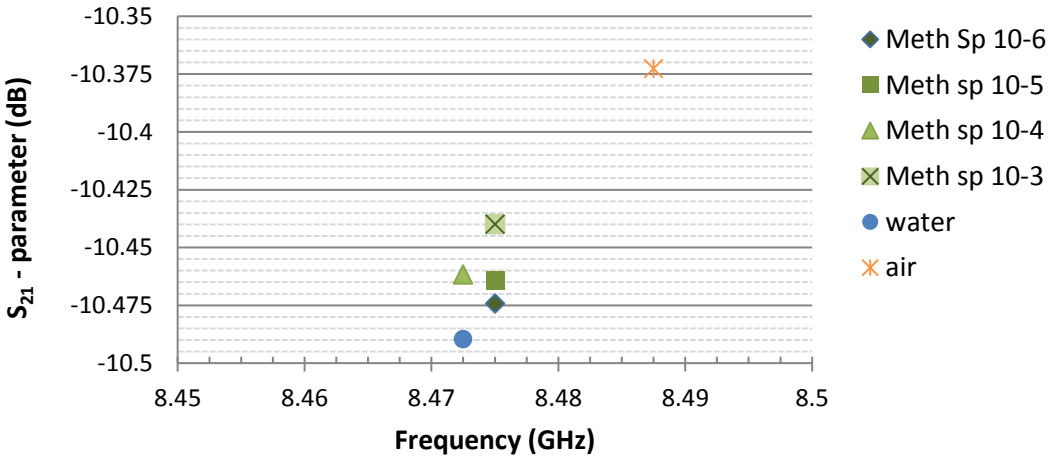

Figure 5.22 Resonant frequencies of various concentrations of methylated spirit and water

The difference in resonant frequency between each dilution is not significant enough to determine whether this is the true result. For example comparing blind samples of each solution there would not be enough information to determine which dilution is which from this result. However comparing the resultant return loss for each of the dilution, there is a trend towards increasing return loss and decreasing methylated spirit concentration. There is a need to perform more error analysis on these curves including looking at the insertion loss S_{11} and other data retrieved from the VNA.

In order to further evaluate the sensing capabilities of the device, larger concentrations of Methylated spirit and water were used in the following results, Figure 5.23.

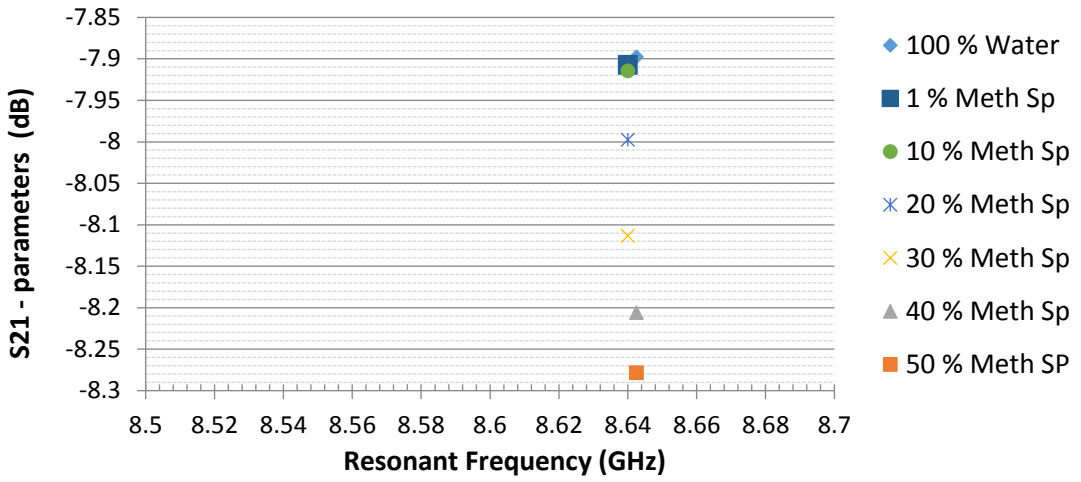

Figure 5.23 Resonant frequency of varying concentrations of methylated sprit and water

The resonant frequency of each of the concentrations are plotted against the corresponding S21-parameter. Although there is no change in the resonant frequency, there is a trend towards high insertion loss at greater concentrations of methylated spirit. However, concentrations less than 10 % are not distinguishable for the pure 100 % water sample.

5.4.4. Adjacent Averaging Technique

In order to better interpret the data and graphs an adjacent averaging technique was employed. Adjacent averaging involves taking the average across a specified set of data points around a data point and replacing that point with the new average value. Assuming there are enough data points collected that the result is not significantly altered. More than 400 data point were taken during the S-parameter measurements.

Taking the results from the methylated spirit concentrations and concentrating on the resonant frequency points the results obtained before and after the application of this technique are shown in Figure 5.24.

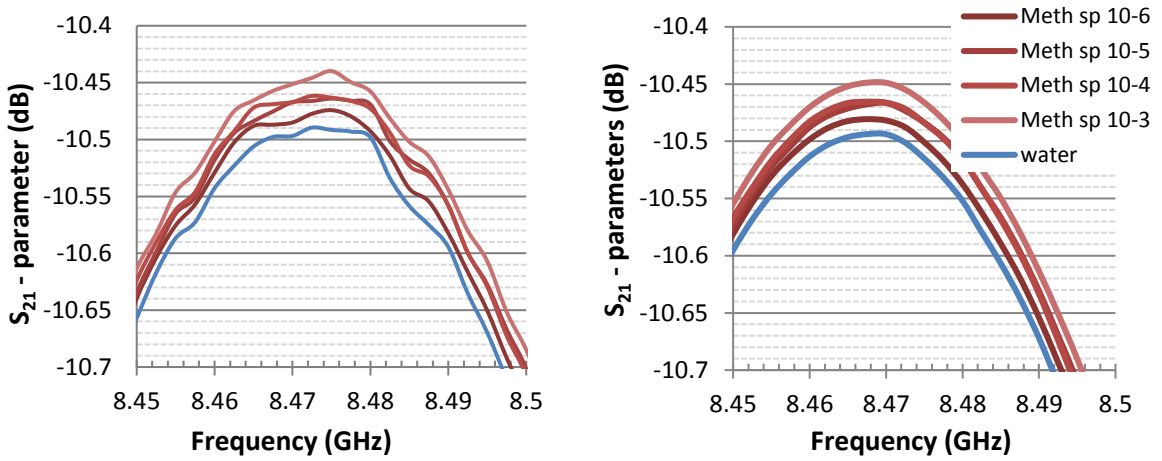

Figure 5.24 Effect of adjacent averaging technique on the smoothing of the data

The noise in the previous results is significantly reduced and each curve can be clearly distinguished. The same was applied to the different oil results and are shown in Figure 5.25.

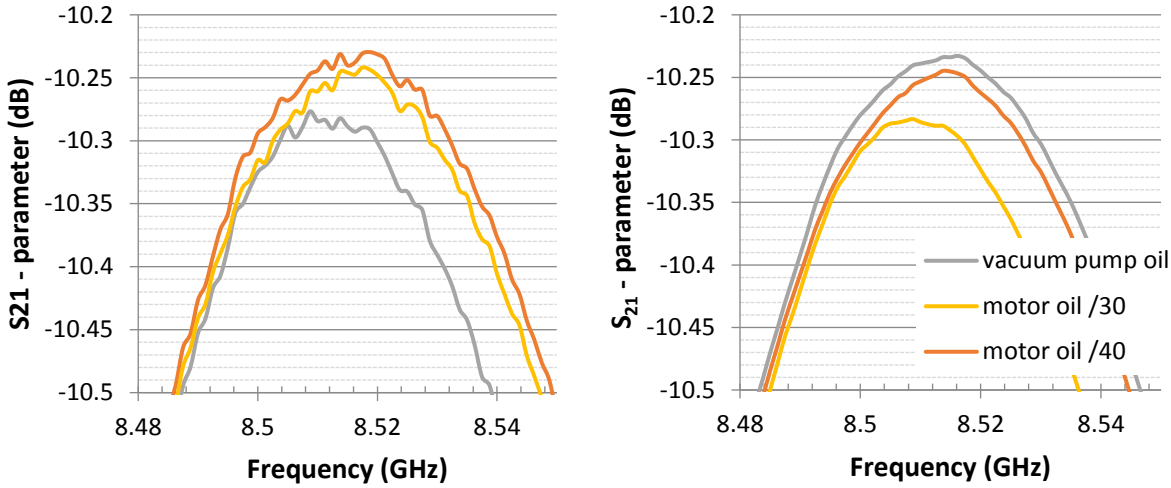

Figure 5.25 Effect of adjacent averaging technique on the water and oil S_{21} parameter measurements

Again the noise after the adjacent averaging technique has been applied is significantly reduced, allowing thereby a better interpretation of the results.

5.4.5. Animal blood samples

The animal bloods used in the following tests were from mice and geese. Goose blood was chosen as the red blood cells of birds contain a nucleus unlike mammalian red blood

cells. Nucleated red blood cells in humans can be an indicator of some infections/diseases or can be found in maternal blood (Foetal nucleated red blood cells, nRBCs). Foetal nRBCs can enter the blood stream of the mother during pregnancy. If these cells could be detected and analysed, the rich genetic heritage of these cells could be used to determine foetal congenital abnormalities very early on in the pregnancy using only a simple sample from the mother own blood circulatory system.

The blood separation was carried out in house using an Eppendorf mini centrifuge, using Eppendorf centrifuge tubes and Gillard pipettes. Firstly, 1 mL of the blood was put into the tubes and placed into the centrifuge. The centrifuge tubes were then distributed evenly in the centrifuge to keep it balanced. The whole blood was then centrifuged at 3500 rpm for 5min. The plasma was then removed from the top of the cells manually using a pipette and dispensed into a clean tube. The cells are then washed in phosphate buffer saline (PBS) and mixed. The centrifugation is then carried out again along with the removal of the supernatant by pipette; this is then discarded. The washing step is repeated once more. The separated red blood cells are then diluted into known concentrations with phosphate buffer saline (PBS). To improve the purity, i.e. cell free, of the extracted plasma, the sample is centrifuged again and the plasma pipetted off into a new tube. The samples are then loaded into syringes for input to the mechanical pump used in the measurement setup.

Mouse blood samples

The first experiment was carried out on mice blood. The RBCs and plasma were extracted using the technique described before. The RBCs were diluted by volume with Phosphate Buffer Saline (PBS) in concentrations of RBC 1:200 PBS, 1:250 and 1:500. The samples were then individually syringed into the microfluidic channel using the mechanical pump set-up. The samples were mechanically syringed into the microfluidic channel at a rate of 200 µL/hr. The first sample was the red blood cells, starting with the smallest dilution 1:500, then 1:250, then 1:200. Before a measurement was taken, sufficient time was left for the sample to fully fill the channel and make sure that any previous sample had been evacuated. Due to the nature of microfluidic capillaries the flow of fluids is in the laminar regime, therefore negligible mixing will occur between samples. Once the microwave measurements were taken for the red blood cell dilutions, the next sample was of the pure PBS. Again the sample was allowed to flow for a sufficient amount of time to ensure that parts of previous sample were not present. Once the microwave measurement was taken

for PBS, the mouse plasma sample was introduced followed using pure deionised (DI) water. The insertion loss results of these mammalian samples are displayed in Figure 5.26.

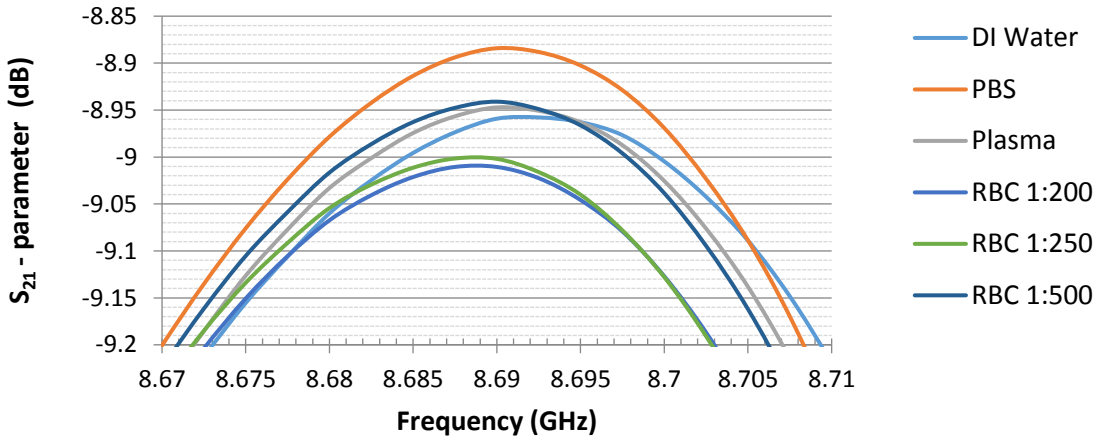

Figure 5.26 S_{21} parameter measurements of mouse blood components compared to pure PBS and water

As a preliminary observation the dilutions are in line with the expected outcome – the higher the dilution of phosphate buffer saline the closer the signal is to the pure sample. Also of note is that the plasma has a similar signal to that of water. In order to fully analyse these results the resonant frequency of each sample is plotted in Figure 5.27.

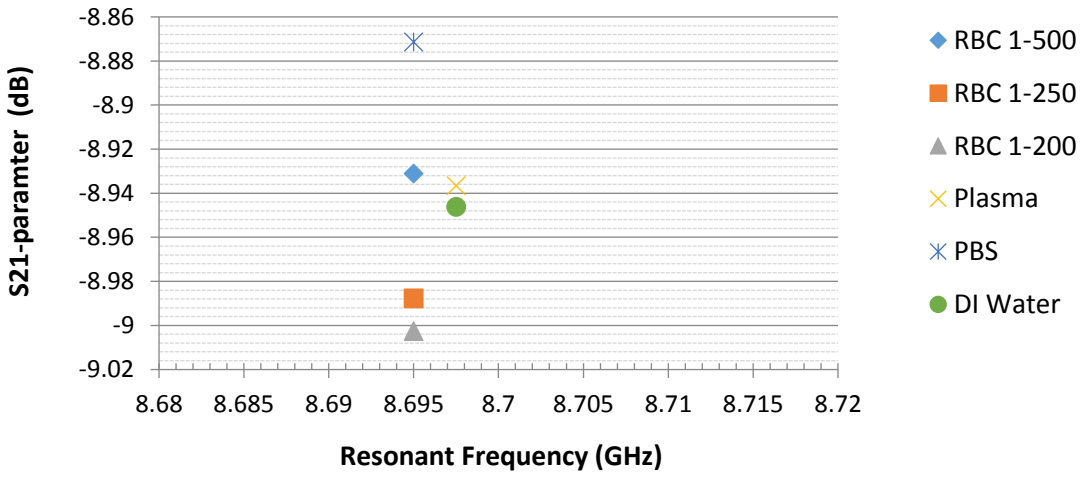

Figure 5.27 Resonant frequency points and insertion loss of the mouse blood sample

The results clearly show the effect of the different concentrations of the red blood cells and phosphate buffer saline. The less concentrated the blood cells are, the closer the resonant frequency gets to that of the pure PBS sample. The plasma results show that the

resonant frequency is the same as water but with a different transmission coefficient, which is explained by the fact that plasma is 90% water. This analysis illustrates the sensitivity of the device, and its ability to detect slight variations in sample concentrations.

Goose blood samples

As mentioned before geese blood was used as the red blood cells of the avian species have a nucleus, unlike mammalian cells. As the nucleus contains DNA and if the nucleated cells can be detected and extracted from the sample, DNA analysis can be carried out. This is particularly important for non-invasive pre-natal testing. Each sample was inserted into the microfluidic channel using the mechanical pump set-up. 5 repeat captures of the S-parameters were taken for each sample. These results were then averaged and the adjacent average technique was applied. The adjacent average resonant frequency v. S_{21}-parameter is shown in Figure 5.28.

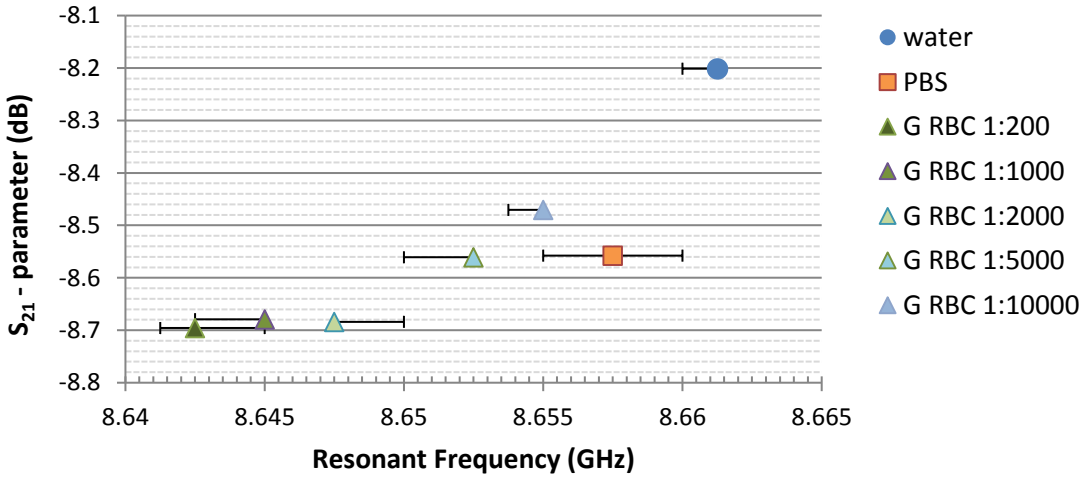

Figure 5.28 S_{21} – parameter resonant frequency of various goose red blood cell concentrations compared to that of PBS and water

The difference in resonant frequency is 2.5 MHz between the first three concentrations, 1:200, 1:1,000 and 1:2,000, and 5 MHz between 1:2000 and 1:5000 concentrations. There is also approximately 0.22 dB insertion loss difference between the highest and lowest concentrations. The 1:5,000 red blood cell concentration resonant frequency is also approximately 2.5 MHz away from the one at 1:10,000 concentration. This in turn is 2.5 MHz away from the pure PBS sample. The resolution of the VNA limits the number of points that can be obtained therefore the sampling was taken at 1.25 MHz intervals. The adjacent averaging technique allows usually a better interpretation of the results however, in this case, the method could distort the data. Therefore it is difficult to distinguish the

PBS sample and the very low concentration samples at 1:5,000 and 1:10,000. The error bars show the maximum deviation during the five repeat measurements taken. There is overlap between the upper and lower concentration samples suggesting that the sensitivity of the device is around 1 in 200. There is also an overlap of the PBS sample and the pure deionised water sample. As explained before PBS is a saline solution (salt water), which explains the relatively similar resonant frequency however the insertion loss is much lower in the PBS sample due to the salts.

5.5 Experimental results and HFSS simulations

Taking the simulation results from Chapter 3 related to modelling and theory of e-plane sensor, a comparison can be performed between the simulations and the experimental results. The model used was that of the waveguide with a Plexiglas® insert with cylindrical capillaries to represent the microfluidic channels, as shown in Figure 5.29.

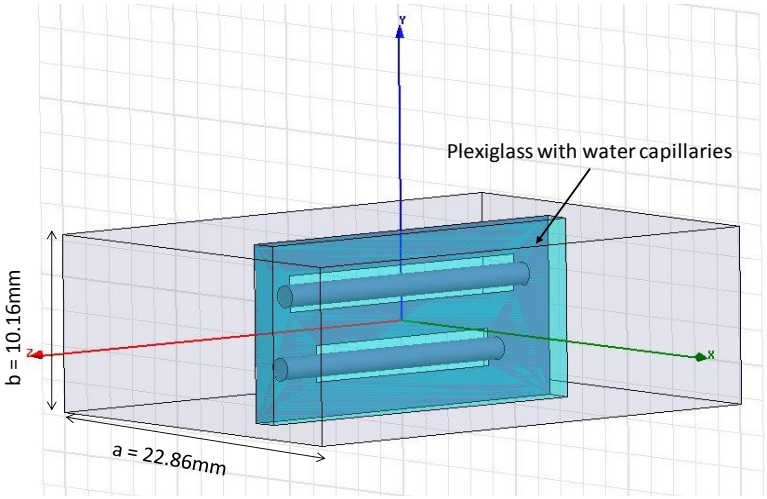

Figure 5.29 Ansoft HFSS 3D model of E-plane sensing device with Plexiglas and capillary insert

By changing the physical properties of the cylindrical capillaries in the model different materials can be analysed. The main property that would affect the sensor is the relative permittivity of the sample to be analysed. Water, air and generic oil from the Ansoft HFSS library of properties and compared to the experimental results. The S-parameters of each fluid are shown in Figure 5.30. The relative permittivities of each sample were: generic oil: 2.2, distilled water: 81 and air: 1.

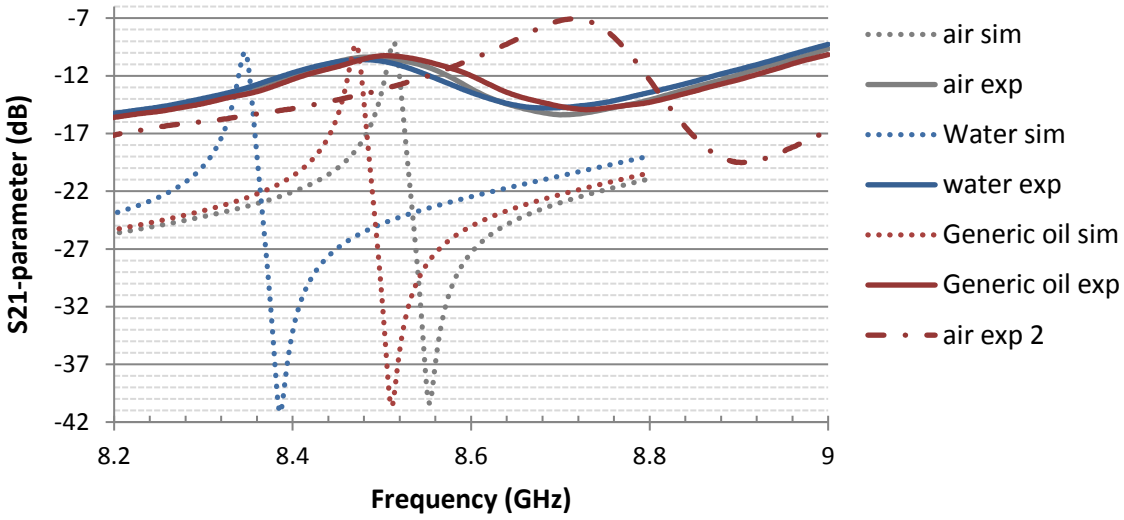

Figure 5.30 S_{21}-parameter comparison between simulations and experimental work

In Figure 5.30, the solid lines represent the experimental measurements and the dashed lines represent the outcome of the simulations. The simulations display a distinctive transmission null occurring at around -42 dB with a bandwidth of approximately 18 MHz. The dashed lines represent the experimental results of the Oil experiments in section *5.4.2 Different oils compared with water*. The transmission null for these experimental results occurs at approximately -16 dB with a bandwidth of 240 MHz. This is therefore a 222 MHz increase in bandwidth from the simulations versus the experimental results. The dash-dot line represents the average results of the empty PMMA channel in section *5.3.2 Oil Experiments*. This result has a larger transmission null at -20 dB with a bandwidth of approximately 120 MHz, half that of the other experimental results. As the simulated model is an ideal case, losses associated with the sensor materials as well as the gap produced by the microfluidic channels are not taken into account. Slight variations in the resonant frequency of between the simulations and experiments can be attributed to the alignment issues that have been mentioned throughout this thesis. The E-plane filter is fully centred in the simulation model however this is difficult to achieve in practice, the alignment of the channels with the apertures of the filter is also not known as it cannot be viewed. These simulation comparisons highlight the manufacturing issues associated with this device, but demonstrates however the sensitivity and operating principle that can be achieved for sensing.

5.6 Conclusions

The results from the experimental work carried out on the sensing device were presented in this chapter. The results obtained from the SU-8 and PMMA fabricated microfluidic channel with various sample solutions were discussed. The repeatability issues associated with the E-plane sensing device were highlighted. The movement and alignment of the E-plane filter was difficult to maintain and position effectively and reliably. A mechanical pump was finally chosen as the method of delivery of the sample to ensure minimal movement of the microfluidic channel and ensuring that the sample was injected into the channels without air entrainment. Methylated spirit concentration above 10 % were distinguishable using this setup. As well as preliminary animal red blood cells with concentrations down to 1:500 clearly distinguishable from the supporting media.

The results from the simulation work carried out in Chapter 3 Modelling and Theory of the E-Plane Sensor were then compared to that of the experimental work. The comparison highlighted the difficulty in achieving a real model as opposed to an ideal model. Larger bandwidths over 200 MHz were observable in the experimental work, whereas the simulations achieved less than 20 MHz. However the principle of the measurement seems valid in both cases.

By minimising the moving parts of this device a sensitive sensing device can be achieved.

5.7 References

[5.1] "Network Analysis Applying the 8510 TRL Calibration for Non-Coaxial Measurements," K. Technologies, Ed., ed, 2000.

[5.2] Accuratus. *99.5 % Alumina Material Properties*. Available: http://accuratus.com/alumox.html

[5.3] A. A. Carey, "The Dielectric Constant of Lubrication Oils," 1998.

6. Design, Modelling and Fabrication of a Bragg Sensor

6.1. Bragg reflector concept

Following the literature review in Chapter 2 and to improve the sensor performance and mitigate the challenges with alignment, a new resonator structure was investigated. The distributed Bragg reflector (DBR) confines most of the field energy of the resonant mode in an empty cavity and shields the walls of the metal enclosure using low-loss dielectric reflectors. The achievable Q-factor of the resulting devices can be in the hundreds of thousands. Such a high Q-factor allows these types of devices to be exploited in sensing applications, which require high sensitivity. By using the design concepts outlined by Flory, Tobar and Floch, the field can be designed to be concentrated at the top of the device where samples can be easily introduced [6.1]. As the presence of the sample perturbs the field, a shift in the resonant frequency will occur allowing this device to be exploited as a sensor. This Chapter also describes the fabrication process for the Distributed Bragg Reflector Sensor. Initial experimental results of the sensor are also presented and compared with the simulation work.

6.2. Bragg Theory

There are several approaches to determining the field distribution in a Distributed Bragg Resonator (DBR). The following sections outline these methods.

6.2.1. ABCD Matrices

Bale and Everard proposed a high Q X-band DBR utilizing an aperiodic Alumina plate arrangement [6.2]. The Bragg structure consists of periodic arrays of air/dielectric sections. To model this, each section is considered as an individual waveguide. These waveguide sections are analysed using 2-port network theory. These 2-port networks are then cascaded to represent the entire Bragg structure. In network analysis, ABCD matrices are used as the resulting network comprises of a simple multiplication of matrices. To illustrate this, a simple two 2-port networks are cascaded as shown in Figure 6.1.

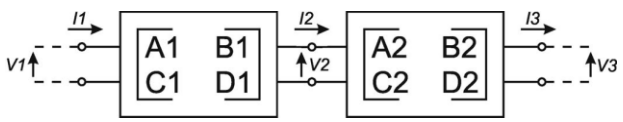

Figure 6.1 A cascade connection of two port ABCD matrices. [6.2]

The resulting matrix equation for the cascade connection above is

$$\begin{bmatrix} V_1 \\ I_1 \end{bmatrix} = \begin{bmatrix} A_1 & B_1 \\ C_1 & D_1 \end{bmatrix} \begin{bmatrix} A_2 & B_2 \\ C_2 & D_2 \end{bmatrix} \begin{bmatrix} V_3 \\ I_3 \end{bmatrix} \quad \textbf{(6.1)}$$

The ABCD matrix for a lossy transmission line of length l with complex propagation constant γ and characteristic impedance Z_0 is given by

$$\begin{bmatrix} V_1 \\ I_1 \end{bmatrix} = \begin{bmatrix} \cosh \gamma l & Z_0 \sinh \gamma l \\ \frac{1}{Z_0} \sinh \gamma l & \cosh \gamma l \end{bmatrix} \begin{bmatrix} V_2 \\ I_2 \end{bmatrix} \quad \textbf{(6.2)}$$

Where V_1, I_1 and V_2, I_2 are the voltages and currents at ports 1 and 2 respectively. Using this equation the matrix can be defined for each section by calculating the complex propagation constant and the wave impedance. For the air sections these are given as

$$(\alpha_c)_{mn}^{TE_z} = \frac{R_s}{a\eta \sqrt{1 - \left(\frac{f_c}{f}\right)^2}} \left[\left(\frac{f_c}{f}\right)^2 + \frac{m^2}{(\chi'_{mn})^2 - m^2} \right] \quad \textbf{(6.3)}$$

Where R_s is the surface loss resistance, f_c is the lower cut off frequency of the waveguide, f is the operating frequency, a is the radius of the waveguide, m and n are the circumferential and radial mode numbers respectively. η is the wave impedance for a plane wave inside an unbounded infinite medium with permittivity ε and permeability μ *[6.2]*.

$$\eta = \sqrt{\frac{\mu}{\varepsilon}} \quad \textbf{(6.4)}$$

χ'_{mn} represent the nth zero of the derivative of the Bessel function of the first order m. in the case of the TE_{01} mode, the value of $\chi'_{mn} \approx 3.8318$. The total loss in the dielectric sections is the sum of the losses associated with the conducting sidewalls that can be calculated using the above equation and the dielectric losses. The dielectric losses are given by

$$\alpha_d = \frac{\omega^2 \mu \varepsilon \tan \delta}{2 \sqrt{\omega^2 \mu \varepsilon - \left(\frac{\chi'_{mn}}{a}\right)^2}} \quad \textbf{(6.5)}$$

Where *tan* δ is the loss tangent, ω is the radial frequency and ε is the relative permittivity of the dielectric material.

6.2.2. Transfer Matrix Formulation

R. Baets [6.3] formulates a transfer matrix method for multilayer thin film systems. The layered medium consists of a stack of layers of thickness d_i and refractive indices n_i, separated by interface planes. A plane wave is incident on the stack as shown below in Figure 6.2.

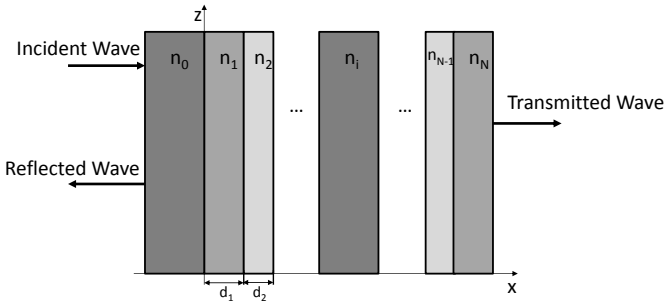

Figure 6.2 Reflection and transmission in a multilayer stack. (Modified from [6.3])

To begin the transfer matrix for wave propagation through an interface is obtained. Consider the interface between a layer *i* and a layer *j* as show in Figure 6.3.

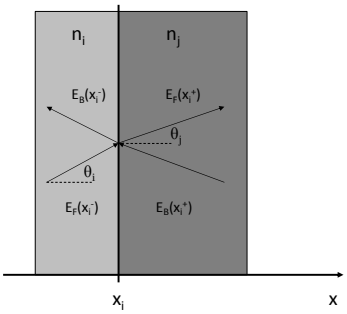

Figure 6.3 Electromagnetic field at the interface between two layers i and j.[6.3]

The amplitudes of the forward and backward propagating waves before and after the interface is given by:

$$\begin{bmatrix} E_F(x_i^+) \\ E_B(x_i^-) \end{bmatrix} = \begin{bmatrix} t_{ij} & r_{ji} \\ r_{ij} & t_{ji} \end{bmatrix} \begin{bmatrix} E_F(x_i^-) \\ E_B(x_i^+) \end{bmatrix} \qquad \textbf{(6.6)}$$

Where E_F, E_B are the forward and backward propagating electric fields for at the interface position x_i. The Fresnel coefficients r_{ij}, t_{ij}, t_{ji} *and* r_{ji} are used as only one wave is incident at the interface. In the case of TE polarisation the Fresnel coefficients are given by

$$r_{ij} = \frac{E_B(x_i^-)}{E_F(x_i^-)} = \frac{k_x^i - k_x^j}{k_x^i + k_x^j} \tag{6.7}$$

$$t_{ij} = \frac{E_F(x_i^+)}{E_F(x_i^-)} = 1 + r_{ij} = \frac{2k_x^i}{k_x^i + k_x^j} \tag{6.8}$$

Where k_x^i and k_x^j are the components of the wave vector k_i in layer i and j, respectively. The TM polarisation is given by

$$r_{ij} = \frac{E_B(x_i^-)}{E_F(x_i^-)} = \frac{n_i^2 k_x^i - n_j^2 k_x^j}{n_i^2 k_x^i + n_j^2 k_x^j} \tag{6.9}$$

$$t_{ij} = \frac{E_F(x_i^+)}{E_F(x_i^-)} = \frac{n_i}{n_j}(1 + r_{ij}) \tag{6.10}$$

When considering a lossless media and no total internal reflection, $k_{x,i}$ can be related to the angle of incidence θ_i by

$$k_{x,i} = n_i k_0 \cos\theta_i \tag{6.11}$$

Therefore the TE polarisations as a function of ray angle are:

$$r_{ij} = \frac{E_B(x_i^-)}{E_F(x_i^-)} = \frac{n_i \cos\theta_i - n_j \cos\theta_j}{n_i \cos\theta_i + n_j \cos\theta_j} \tag{6.12}$$

$$t_{ij} = \frac{E_F(x_i^+)}{E_F(x_i^-)} = 1 + r_{ij} = \frac{2n_i \cos\theta_i}{n_i \cos\theta_i + n_j \cos\theta_j} \tag{6.13}$$

Similarly for TM polarization

$$r_{ij} = \frac{E_B(x_i^-)}{E_F(x_i^-)} = \frac{n_j \cos\theta_i - n_i \cos\theta_j}{n_j \cos\theta_i + n_i \cos\theta_j} \tag{6.14}$$

$$t_{ij} = \frac{E_F(x_i^+)}{E_F(x_i^-)} = \frac{n_i}{n_j}(1 + r_{ij}) = \frac{2n_i \cos\theta_i}{n_i \cos\theta_i + n_j \cos\theta_j} \tag{6.15}$$

For an incidence wave perpendicular to the stack, there is no difference between the TE and TM case. Using the symmetry relations of the Fresnel coefficients

$$r_{ij} = -r_{ij} \tag{6.16}$$

$$t_{ij}t_{ji} - r_{ij}r_{ji} = 1 \tag{6.17}$$

Equation (6.6) can be written as

$$\begin{bmatrix} E_F(x_i^-) \\ E_B(x_i^-) \end{bmatrix} = \frac{1}{t_{ij}} \begin{bmatrix} 1 & r_{ij} \\ r_{ij} & 1 \end{bmatrix} \begin{bmatrix} E_F(x_i^+) \\ E_B(x_i^+) \end{bmatrix} \quad \textbf{(6.18)}$$

Thus the transfer matrix $\mathbf{T}_{ij}$ for wave propagation through the interface between layers *i* and *j* is:

$$T_{ij} = \frac{1}{t_{ij}} \begin{bmatrix} 1 & r_{ij} \\ r_{ij} & 1 \end{bmatrix} \quad \textbf{(6.19)}$$

Consider now the wave propagation through the layer *i*. The amplitudes of the forward and backward propagating waves before and just after the interfaces of the adjacent layers is given by:

$$E_F(x_i^-) = E_F(x_{i-1}^+) e^{-jk_{x,i}d_i} \quad \textbf{(6.20)}$$

$$E_B(x_{i-1}^+) = E_B(x_i^-) e^{-jk_{x,i}d_i} \quad \textbf{(6.21)}$$

Where d_i is the thickness of the layer *i*. The transfer matrix, $\mathbf{T}_i$, for wave propagation through the layer *i* is therefore given by

$$\boldsymbol{T}_i = \begin{bmatrix} e^{j\Phi_i} & 0 \\ 0 & e^{j\Phi_i} \end{bmatrix} \quad \textbf{(6.22)}$$

In a lossless media and in the absence of total internal reflection the phase change Φ is equal to

$$\Phi_i = k_{x,i}d_i = \frac{2\pi}{\lambda_0} n_i d_i \cos\theta_i \quad \textbf{(6.23)}$$

As the amplitude E_f and E_b are described at a constant z-direction, Φ corresponds to the distance between the two phasefronts as described in Figure 6.4.

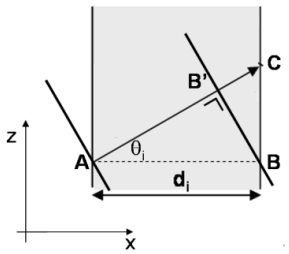

Figure 6.4 Analysis of Equation (6.23). The phase change Φ corresponds to the path length |AB'| and not to the path length |AC|.[6.3]

The complete transfer matrix for wave propagation through a multilayer stack is the multiplication of each of the individual transfer matrices as given by

$$\begin{bmatrix} E_F(x_0^-) \\ E_B(x_0^-) \end{bmatrix} = \boldsymbol{T}_{0N} \begin{bmatrix} E_F(x_{N-1}^+) \\ E_B(x_{N-1}^+) \end{bmatrix} = \begin{bmatrix} T_{11}^{0N} & T_{12}^{0N} \\ T_{21}^{0N} & T_{22}^{0N} \end{bmatrix} \begin{bmatrix} E_F(x_{N-1}^+) \\ E_B(x_{N-1}^+) \end{bmatrix} \quad \textbf{(6.24)}$$

Where

$$\boldsymbol{T}_{0N} = \boldsymbol{T}_{01}\boldsymbol{T}_1\boldsymbol{T}_{12}\boldsymbol{T}_2 \ldots \boldsymbol{T}_{(N-1)}\boldsymbol{T}_{(N-1)N} \quad \textbf{(6.25)}$$

The design for the Bragg sensor incorporates the concepts of a Fabry-Perot cavity combined with Bragg reflectors. The structure is similar to that of Flory and Taber [6.4], having three DBR pairs. Instead of a cylindrical cavity, a rectangular cavity was investigated in this thesis as it allows to reduce the complexity in manufacturing the reflectors as shown Figure 6.4.

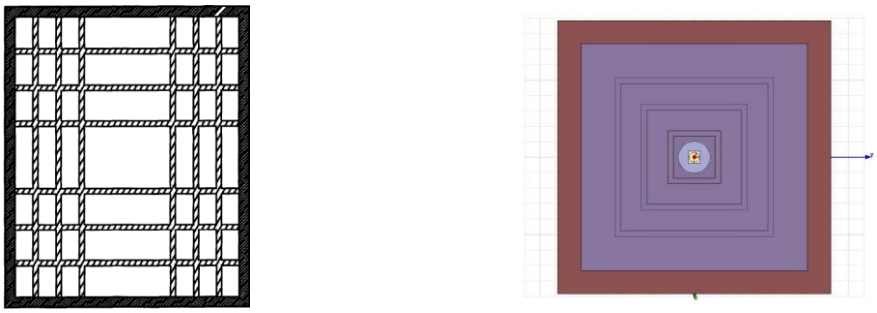

(a) (b)

Figure 6.4 (a) Side cut-away view of the Flory cylindrical dielectric DBR structure inside the metal structure [6.4] (b) Top view of the rectangular cavity with DBR structure

The structure can be broken down into manageable sections. First consider a rectangular cavity with the Bragg reflectors as represented in Figure 6.5.

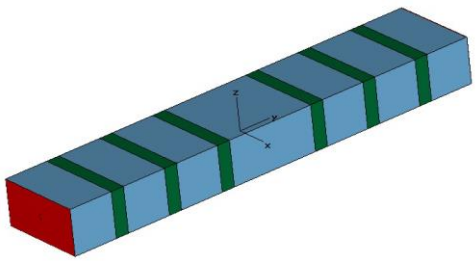

Figure 6.5 Fabry-Perot with Bragg reflectors in a rectangular waveguide [6.5]

An empty rectangular waveguide has a cut-off frequency, f_c, at the TE_{10} mode given by

$$f_c = \frac{c}{2a} \tag{6.26}$$

Where a is the length of the waveguide along the x-axis. The propagation constant, k_y, along the y-axis along the rectangular waveguide is given by

$$k_y^2 = k_0^2 - k_c^2 \quad \text{where } k_0 = \frac{\omega}{c} \tag{6.27}$$

And for the TE_{10} mode

$$k_c = \frac{\pi}{a} \tag{6.28}$$

From this equation the wavelength in the direction of propagation is given by

$$\lambda_y = \frac{2\pi}{k_y} \tag{6.29}$$

The centre layer of the rectangular structure shown above can be chosen such that the fundamental Fabry-Perot resonance is also the centre of the Bragg bandgap

$$l_{cen} = \frac{\lambda_y}{2} \tag{6.30}$$

The structure was simulated in CST by M. Lorente Crespo [6.5] and the results are shown below

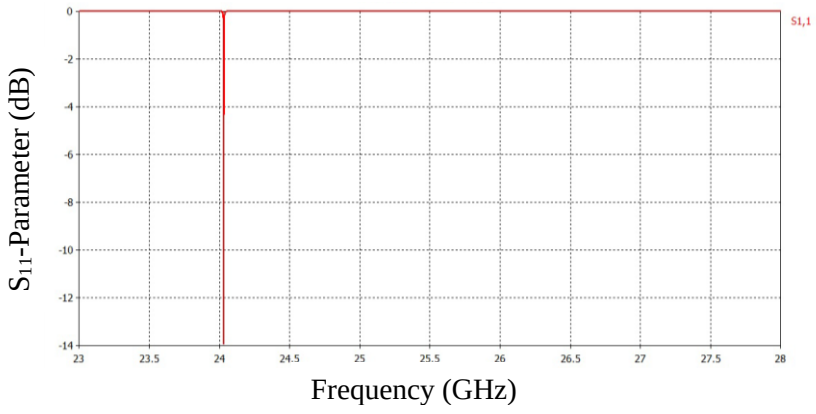

Figure 6.6 Simulated reflection coefficient of the λ = 17 mm 6 pairs DBR with central defect [6.5]

The next stage is to consider two of these structures together at 90° to each other. The structure is then enclosed in a copper cavity and the feed line is in the middle of the cross structure at the Fabry-Perot cavity as shown in Figure 6.7.

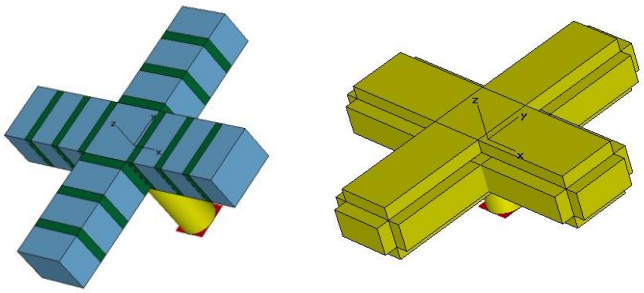

Figure 6.7 6-pair cross DBR with half wavelength central cavity.[6.5]

The length of the Fabry-Perot cavity is square and the length dimension given by

$$\frac{\lambda_y}{2} = a \tag{6.31}$$

From equation (6.27) we have

$$k_y^2 = \left(\frac{2\pi}{\lambda_y}\right)^2 = \left(\frac{2\pi f_{op}}{c}\right)^2 - \left(\frac{\pi}{a}\right)^2 \tag{6.32}$$

Therefore

$$a = \frac{2f_{op}}{\sqrt{2}c} \tag{6.33}$$

Together with equation (6.26) the operating frequency is given as

$$f_{op} = f_c\sqrt{2} \tag{6.34}$$

The cross shape system can no longer be excited by waveguide ports, therefore a coaxial feed is required. The simulated reflection coefficient is shown in Figure 6.8.

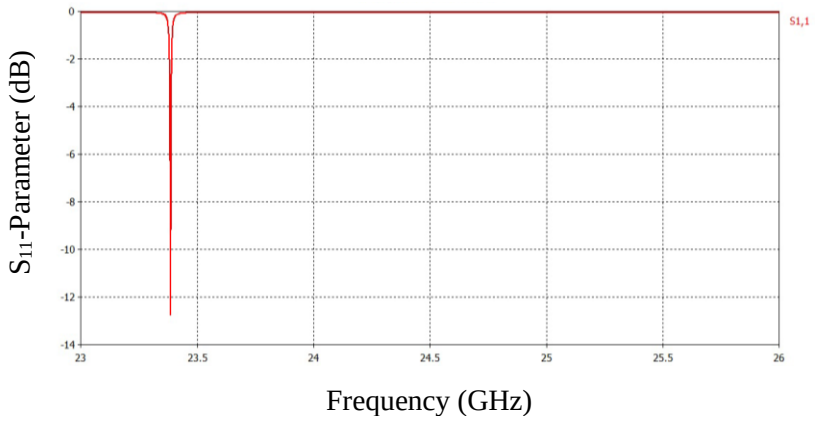

Figure 6.8 simulated reflection coefficient of cross DBR[6.5]

The Q-factor is 2783 and the mode is well confined to the central cavity. This cross is then centralised is a square copper cavity as shown below, Figure 6.9.

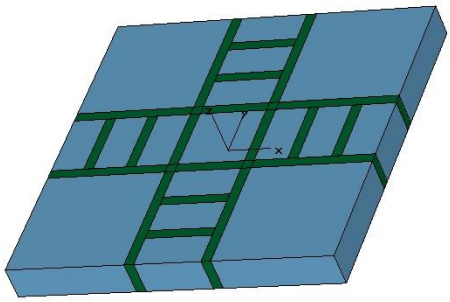

Figure 6.9 DBR cross structure within a square copper cavity[6.5]

The simulated reflection coefficients shown in Figure 6.10 have a resonance at 23.3 GHz with 1942 Q-factor.

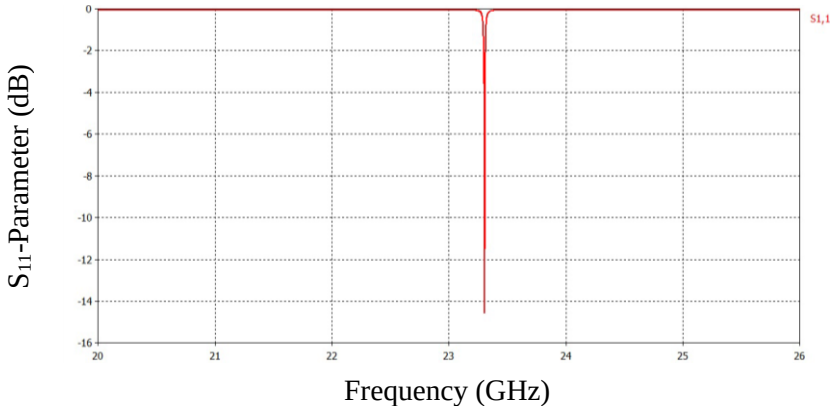

Figure 6.10 simulated reflection coefficient of cross DBR in square cavity[6.5]

Finally the sapphire layers are extended towards the copper walls to form the complete device as shown in Figure 6.11.

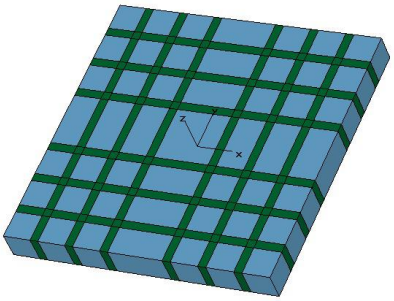

Figure 6.11 Sapphire/air DBR square device[6.5]

The simulated reflection coefficient is shown in Figure 6.12, the resonant frequency and Q-factor are the same as before.

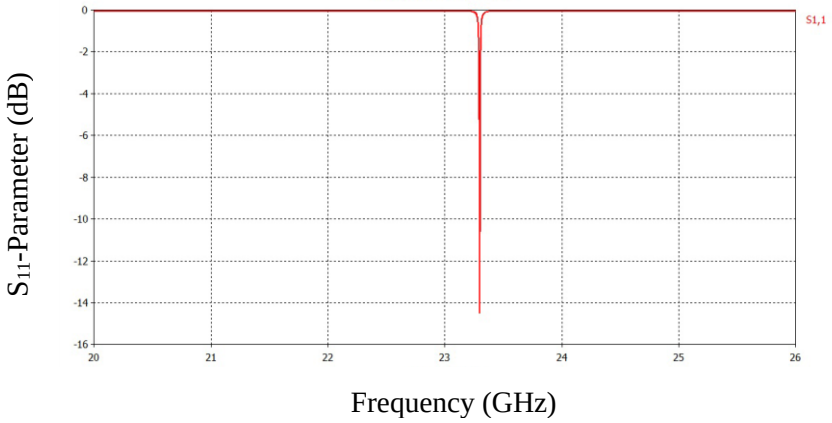

Figure 6.12 Simulated reflection coefficient of complete device [6.5]

However, the E-field distribution is higher from the previous cross design as shown in Figure 6.13.

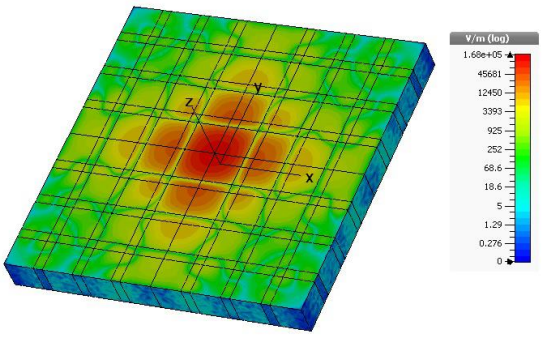

Figure 6.13 Magnitude of the E-field at the resonant frequency 23.3 GHz[6.5]

The Q-factor could be improved by adding more DBR pairs and/or using sapphire in the z-direction to minimise the losses.

6.3. Ansys HFSS Modelling of Bragg Sensor

The design and modelling of the Distributed Bragg Reflector (DBR) device was carried out using a Finite Element Modelling software, Ansys HFSS. Adaptive meshing techniques used in this software allow the user to only specify the geometry, material properties and the desired output. The full design process is described in Chapter 3; a brief outline of this process is shown in the flowchart in Figure 6.14.

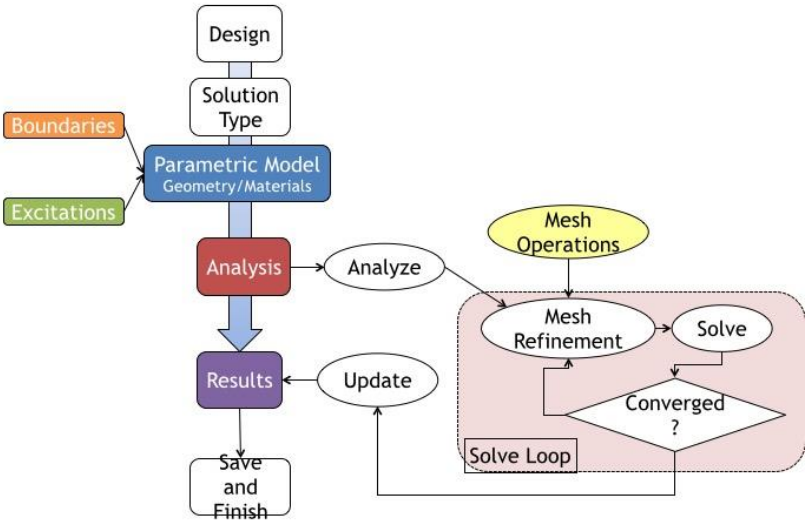

Figure 6.14 HFSS design process flowchart

The initial design created in HFSS is shown in Figure 6.15.

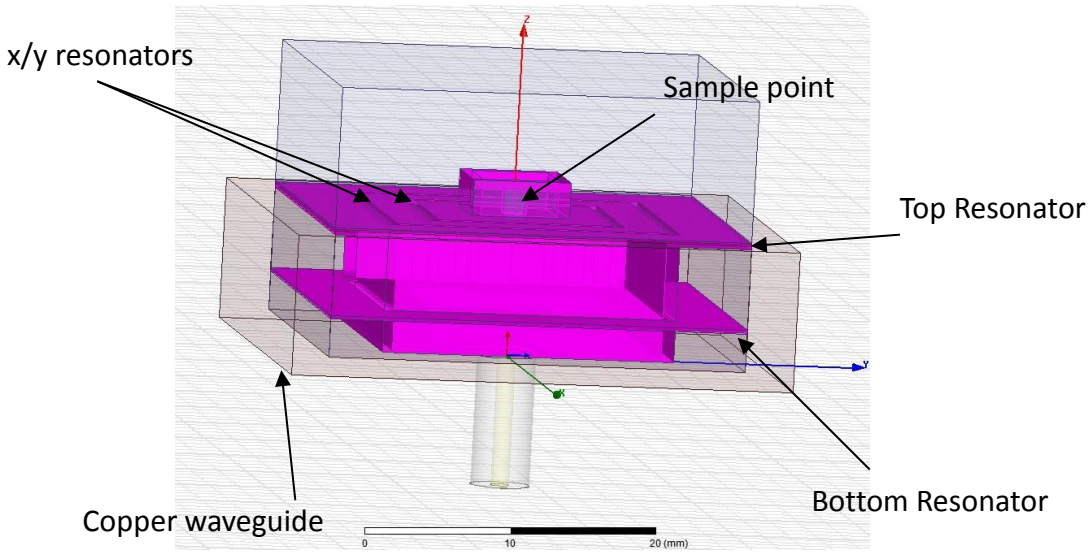

Figure 6.15 3D HFSS Model of Distributed Bragg Reflector sensor

A copper waveguide encases the sapphire x/y plane DBR resonators. The top and bottom resonators are also made from sapphire. The thickness of the top resonator was adjusted using the parametric optimisation tool available in HFSS. This allows several simulations to be done over varying model dimensions. The results from this optimization are shown below in Table 6.1.

Table 6.1 Optimetric analysis of upper resonator

Lower Reflector (mm)	Upper Reflector (mm)	Resonant Frequency (GHz)	'3 dB' bandwidth (GHz)
0.86	-0.15	20.85451	0.00144
0.25	0.05	20.56021	0.00072
0.25	0.1	20.73737	0.00096
0.25	0.15	20.97502	0.00048
0.25	-0.15	21.13225	0.00048
0.25	0.2	21.19394	0.00096

The negative thicknesses refer to the position of the reflector with respect to its original coordinates. The thickness of 0.15 mm for the upper reflector gives a narrower bandwidth optimal for sensing. The results are also represented graphically in Figure 6.16.

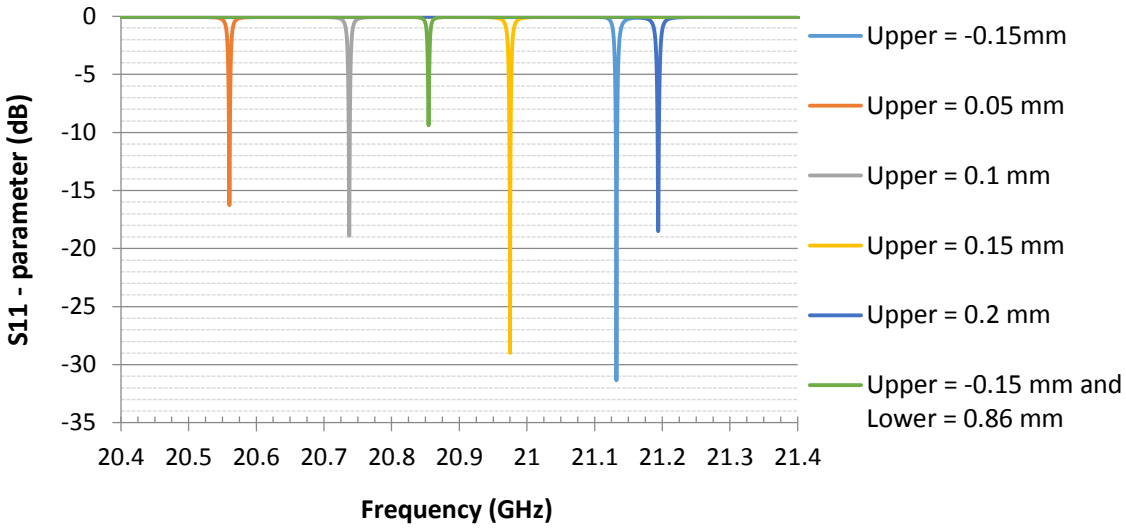

Figure 6.16 Upper resonator optimization results from HFSS

The optimum thickness of the upper resonator is 0.15 mm, the position of the resonator at this thickness changes the resonant frequency by approximately 157 MHz. Therefore the upper sapphire resonator is best placed in a slight recess in the copper cavity.

6.4. Fabrication

The device was fabricated in copper, sapphire and ceramic using the Low Temperature Co-fired Ceramic (LTCC) technology. Dimensions of the inside of the copper walls and the sapphire square ring resonators are shown in Figure 6.17.

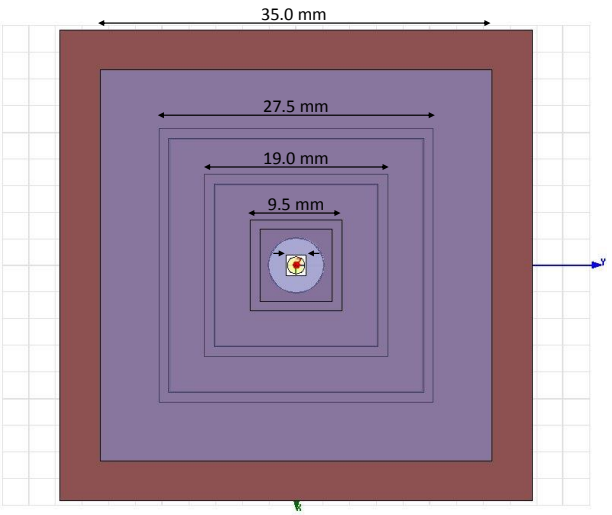

Figure 6.17 Dimensions of the copper casing (35 mm) and sapphire inserts. Thickness of the layers is indicated in the main body of the text.

3 mm thick copper sheets were used for the four side walls, as indicated in Figure 6.17, as well as the bottom wall of the waveguide. 1 mm slots were machined to allow the sapphire Bragg resonators to be inserted into the hollow structure. A coaxial RF connector, SMA connector, was fitted to the underside of the device to interface with the Vector Network Analyser (VNA). The connector is represented in the figure above by the two circles centred in the middle of the copper casing. The small 1.5 mm square in the middle of the figure represents the well of the LTCC top plate, which accommodates the liquid samples. The LTCC top plate has the same square dimensions as the inside of the copper walls, 35 mm.

The sapphire was obtained from the company Saint-Gobain Crystals [6.6]. A single crystal sapphire sheet was grown using the Edge defined Film fed Growth (EFG) method. This process yields grown to shape material. Other growth processes only allow standard sizes to be grown, which then must be cut to shape by highly skilled workers using expensive diamond impregnated tooling. A diagram of the EFG method is shown in Figure 6.18.

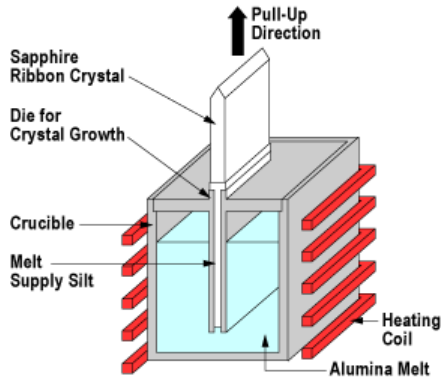

Figure 6.18 Schematic showing the Edge defined Film fed Growth (EFG) method [6.7].

A crucible contains commercially available aluminium oxide (Al_2O_3) melted to a temperature moderately above the melting point, ~ 2200°C. A sapphire seed of specific crystallinity is dipped into the melt on top of the die and drawn out, solidifying into sapphire in the shape of the die. This process allows for tight control over crystal orientation. For the sensing device the single crystal sapphire sheet needed to be cut into smaller pieces to create the Bragg resonators. As sapphire has a value of 9 on the Mohs scale of hardness, only special laser techniques and diamond saws can be used to cut it.

6.4.1. Diamond disc cutting

Diamond disc cutting is a machining technique where diamond particles are impregnated into a holding material, usually steel. Shown in Figure 6.19 is a picture of a typical diamond rimmed saw blade.

Figure 6.19 Thin rimmed diamond saw [6.8].

The sapphire sheet was cut using the diamond blade technique into ~20 mm by ~35 mm rectangles as shown in Figure 6.20 (a). A notch was cut so that the resonators could slot together to form the pattern shown in Figure 6.20 (b).

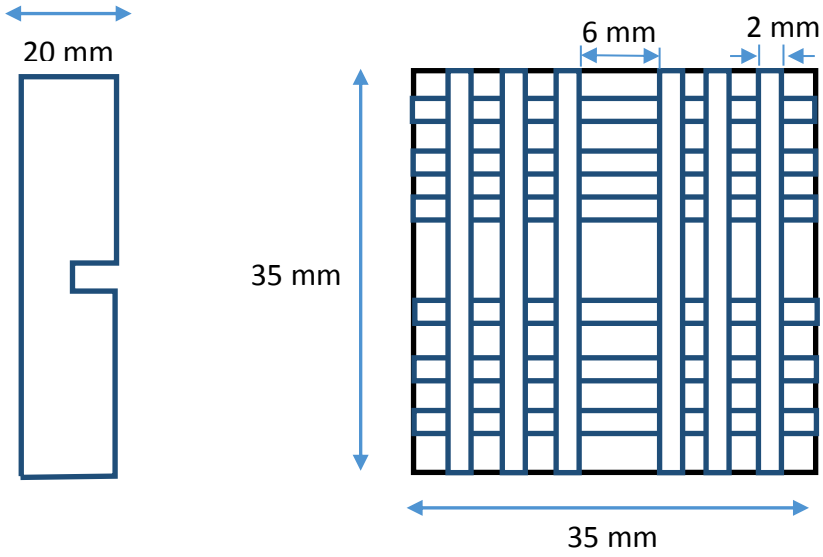

(a) ***(b)***

Figure 6.20 (a) individual cut sapphire pieces. (b) Construction pattern used to create the Distributed Bragg Resonator pattern.

One square sheet of approximately 35 mm by 35 mm was used as the z-plane resonator. The copper and sapphire structure is shown in Figure 6.21.

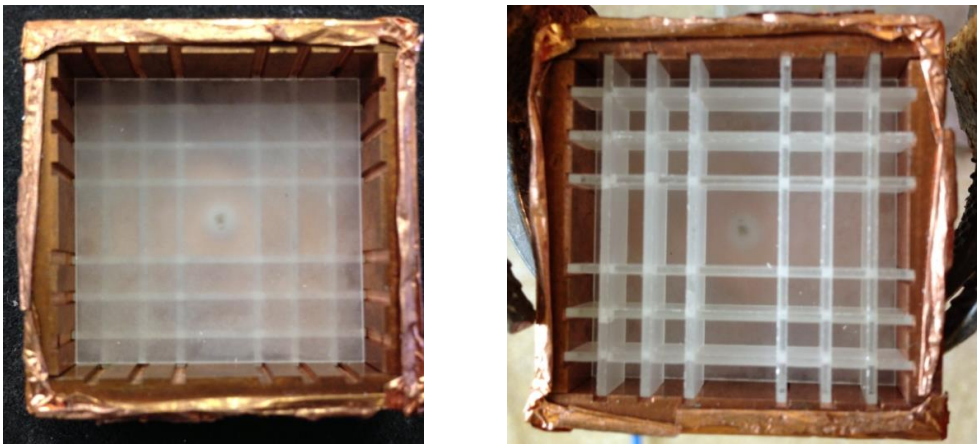

Figure 6.21 Left – bottom x, y pattern resonator with z-plane resonator on top. Right – Second x, y plane resonator pattern. Copper walls show the grooves which the sapphire resonators slot into.

6.4.2. Stealth Laser Dicing

Stealth laser dicing is a wafer dicing process that was developed through the use of silicon permeable infrared nanosecond pulsed laser technology. Kumagai *et al.* first presented the technique in 2006 as an alternative method to harsher techniques such as the diamond blade and laser ablation techniques [6.9]. These techniques have the disadvantages of introducing undesirable heat, mechanical vibration and stress. Stealth dicing (SD) has the advantages of high speed, no debris contaminants and is a completely dry process. The process has two steps: laser processing and the wafer separation.

Laser Processing

The laser beam is designed to be focused into the interior of the wafer. The laser beam power is set to meet such a condition that the power density of the focal point is higher than the processing threshold but the power density at the surface is lower than the threshold. The layers formed within the material during this process as called SD layers. A schematic of the laser processing is shown in the figure below Figure 6.22.

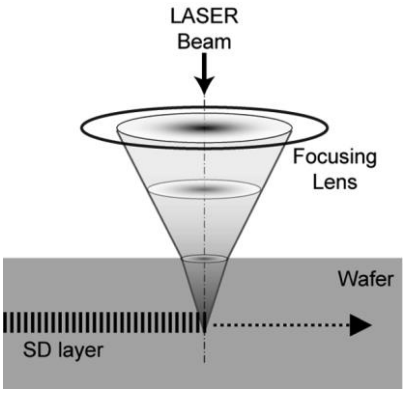

Figure 6.22 Laser beam design of SD method and formation of the SD layer. The laser beam is designed to be focused into the interior of the wafer. [6.9]

The SD layers act as crack initiation sites and guides for the separation.

Wafer Separation

Once the SD layers are formed, the wafer undergoes wafer separation. The wafer is placed on a dicing tape that fixed on a dicing frame. The cylindrical stage is then pushed up onto the dicing tape and wafer separating each chip along the SD layer. A schematic of the process is shown in the figure below, Figure 6.23.

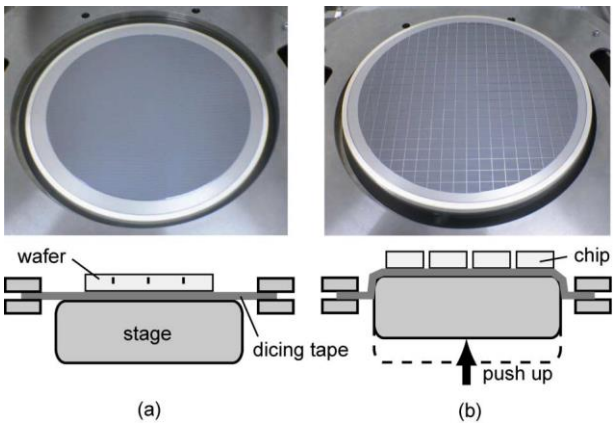

Figure 6.23 Wafer separation process. a) Wafer is placed onto the dicing tape on the stage. b) The stage is then pushed up separating each chip. [6.9]

Figure 6.24 below shows scanning electron microscopy images of a divided silicon wafer with 50 μm thickness by stealth dicing. There are is no chipping and less meandering of the divided line. There is also no debris contaminant.

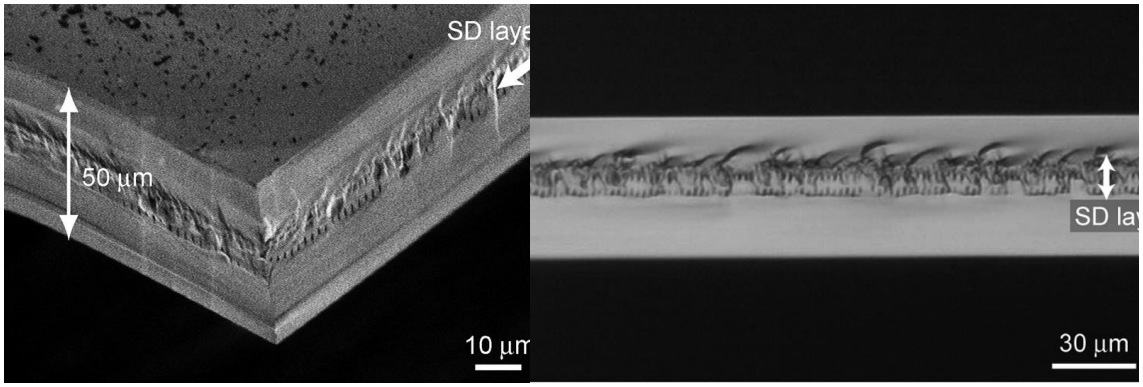

Figure 6.24 SEM images of a divided silicon wager with 50 μm thickness by stealth dicing method. [6.9]

The final piece is the Low Temperature Co-fired Ceramic top plate that has the sensing well. The LTCC was machined using a CO_2 Epilog laser system. A small cavity was etched into one of the layers to incorporate the sample. This was done by first machining a hole into the LTCC substrate. To undergo the lamination process the cavity must be filled with a sacrificial material to insure that the cavity does not collapse under the lamination procedure. In this case alumina particles were packed into the cavity and then compressed using a standard vice. The LTCC structure then underwent the lamination process at 10 MPa at 70 °C for approximately 8 minutes. The alumina sacrificial material was then removed and the LTCC structure was then co-fired at a temperature profile as shown in Figure 6.25.

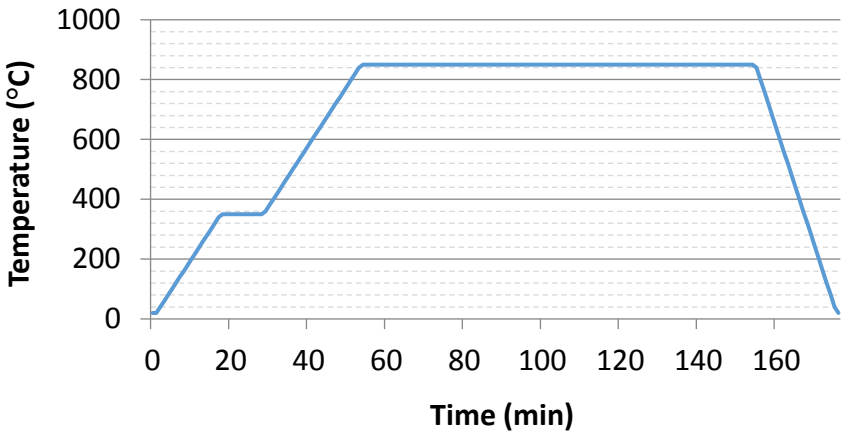

Figure 6.25 Temperature profile for sintering the low temperature co-fired ceramic.

Beginning at room temperature the oven is heated to ~ 350°C and remains at this temperature for about 10 minutes. The temperature is then ramped to 850°C for 150 minutes. The oven is then left to cool down to room temperature before the LTCC samples are removed. The LTCC structure was then slotted into the cavity along with the sapphire. The completed device is shown in Figure 6.26.

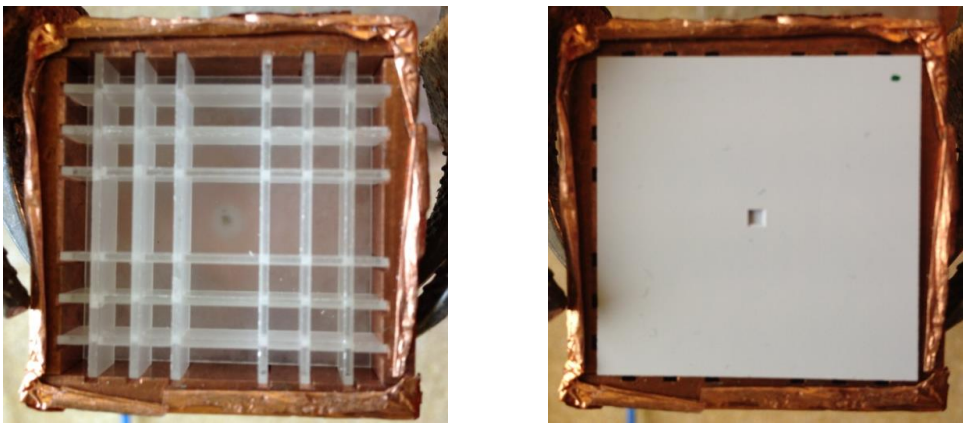

Figure 6.26 Completed DBR sensor.

6.5. Experimental Results

Once the individual components were fabricated the device was assembled and set up for testing. An Agilent N5225A Vector Network Analyser (VNA) was used to measure the response. The VNA requires calibration before the device under test (DUT) can be measured. This was carried out using the Agilent N4691 Electronic Calibration (ECal) Module. This ECal module is connected to the VNA via a USB cable, Figure 6.27. The VNA automatically recognises the type of module, frequency range, and connector type.

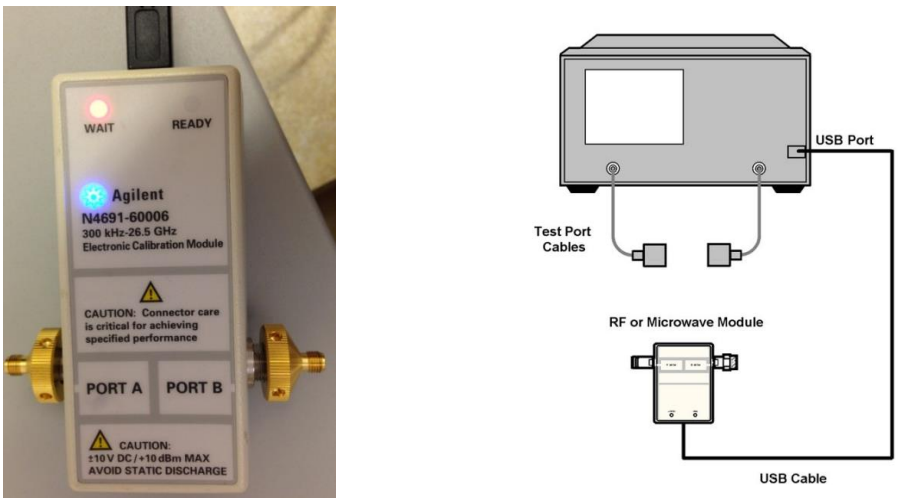

Figure 6.27 Electronic Calibration Module connected to the Vector Network Analyser

The ECal module is then left to warm up for approximately 15 minutes, once complete the ready light on the module will illuminate. The DUT is then connected to the test port cable via a coaxial cable as shown in Figure 6.28.

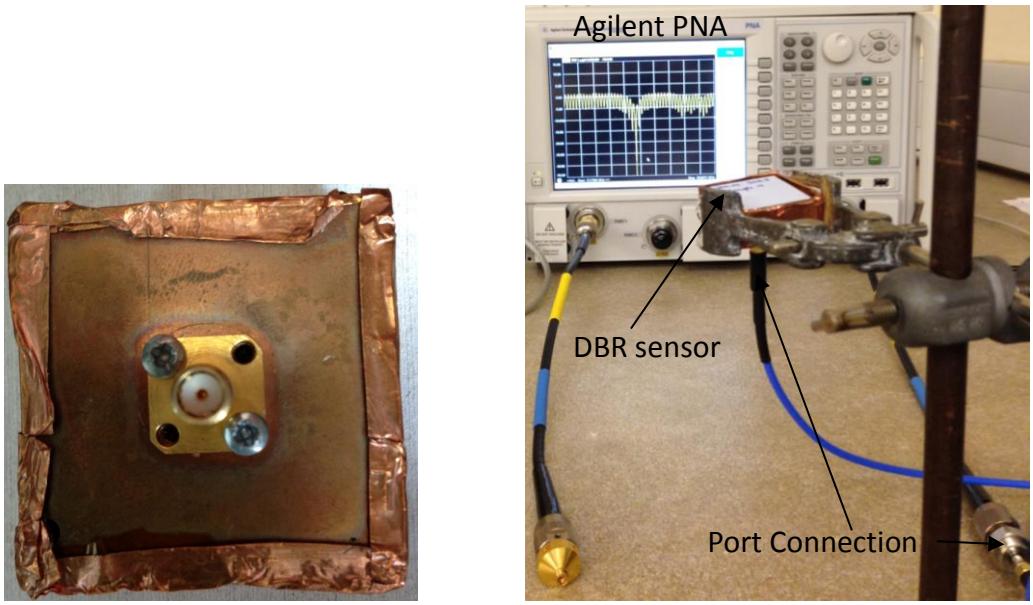

a) b)

Figure 6.28 a) Bottom of the DBR showing the SMA connector. b) Connected to port1 of the Agilent PNA.

Samples of water and oil were collected in Eppendorf tubes. The tubes were then inserted manually into the centre of the cavity. The S_{11} responses of the distributed Bragg resonator with the various samples are shown in Figure 6.29.

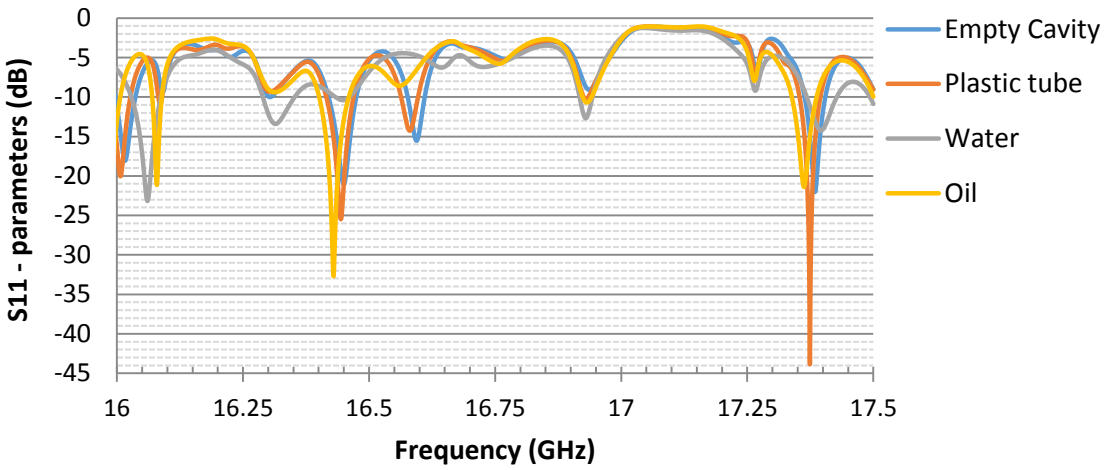

Figure 6.29 S_{11}-parameter response of Bragg cavity with various samples

There are several strong resonances associated with the different modes of the resonator. The reflection response at around 17.3 GHz is selected for further inspection. The S11-parameter results are shown below in Figure 6.30. The resonant frequencies of the various samples are shown in Table 6.2.

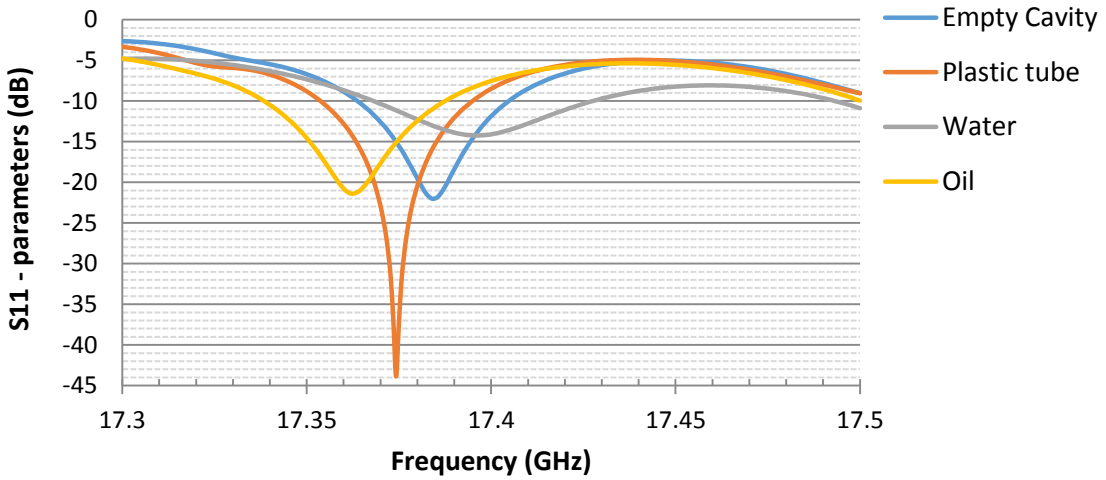

Figure 6.30 S11 response of Bragg sensor at 16 GHz

Table 6.2 Resonant frequencies of various samples

	Empty Cavity	Empty Eppendorf tube	Tube with oil	Tube with water
Resonant Frequency (GHz)	17.384	17.374	17.363	17.397

The empty Eppendorf tube exhibits approximately 10 MHz decrease in resonant frequency from the empty cavity. The oil filled tube shows a decrease in resonant

frequency of approximately 21 MHz from the empty cavity. The water filled tube displays an increased resonant frequency and indeed a higher reflection from that of the empty cavity. This can be attributed to the fact that water is a slightly conductive material.

6.6. HFSS Modelling

Further to the modelling in the previous chapters, a new model was created to simulate the device that has been fabricated. Figure 6.31shows the layout of the design

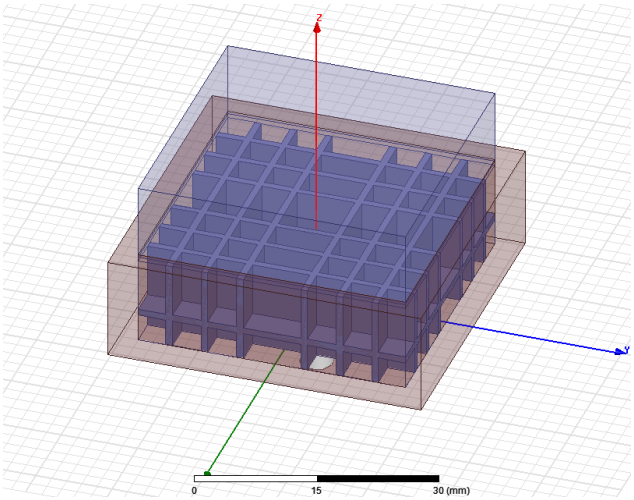

Figure 6.31 HFSS model of the fabricated device.

The sapphire DBR resonators were created in the grid pattern as described above in the fabrication. The simulation does not include a top plate and therefore the microwaves are exposed to the air cavity above the device. The S_{11} parameters of the simulated and experimental cavities are shown in Figure 6.32.

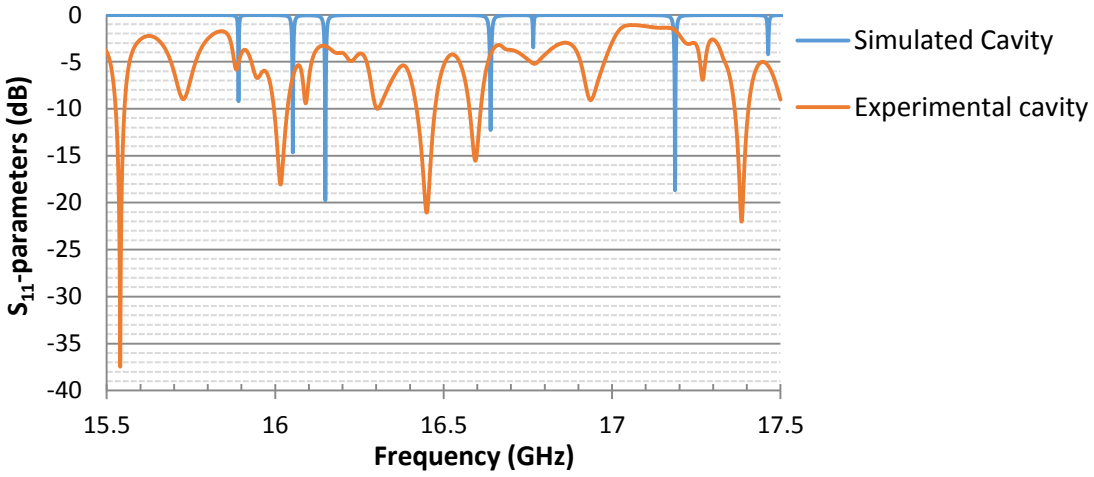

Figure 6.32 S_{22}-parameter of HFSS DBR model as fabricated

There are some spurious resonances that appear in the experimental results. This could be due to the fabrication of the device such as discrepancies with the alignment of the sapphire Bragg resonators. There are two distinct resonances that appear in the simulation, one at 17.18 GHz and another at 17.97 GHz. Using the stronger resonance frequency a field plot was made across the x-z plane and the simulated results are shown below in Figure 6.33.

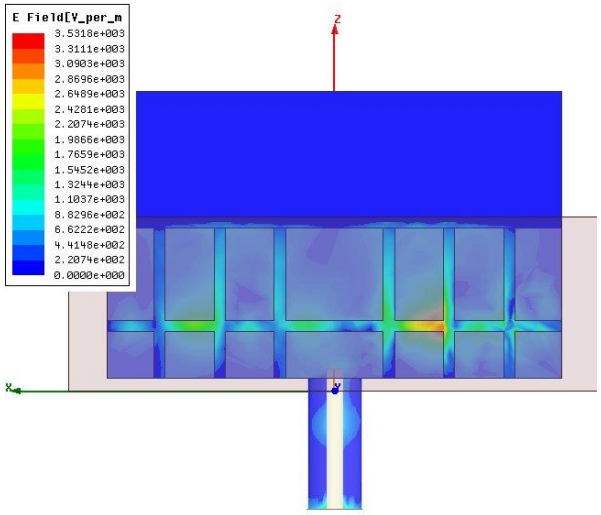

Figure 6.33 Electromagnetic field plot at 17.97 GHz

The field plot indicated that the field is at its highest intensity in the next outer ring of the DBR. This means that the fabricated device is not in the correct mode. As stated earlier further simulation and modification to the DBR structure would be required to rectify this. Alternatively if changes cannot be made to the fabricated device, the sample point can be moved to the high field position. This would not provide the greatest sensitivity but would demonstrate the concept of the DBR as a sensor.

6.7. Conclusions

The theoretical design of the Bragg resonator sensor has been discussed using various techniques. The initial simulation studies of the Distributed Bragg Resonator structure show promising results. The resonant frequency of the optimised design is 21.13 GHz and the Q-factor is approximately 44,016. Initial results of the fabricated device were presented. Samples of water and oil were introduced manually into the cavity in Eppendorf tubes. The results showed resonance frequency shifts up to approximately 20 MHz from the base resonance of the cavity. However using simulations the cavity was found to be in the incorrect mode and therefore the nearfield was not at its peak at the centre of the device. For future work the device requires more precision machining as well as optimisation of the insertion pin of the coaxial connection.

6.9. References

[6.1] M. E. Tobar, J. M. le Floch, D. Cros, and J. G. Hartnett, "Distributed Bragg reflector resonators with cylindrical symmetry and extremely high Q-factors," *Ultrasonics, Ferroelectrics and Frequency Control, IEEE Transactions on*, vol. 52, pp. 17-26, 2005.

[6.2] S. Bale and J. Everard, "High-Q X-band distributed Bragg resonator utilizing an aperiodic alumina plate arrangement," *Ultrasonics, Ferroelectrics, and Frequency Control, IEEE Transactions on*, vol. 57, pp. 66-73, 2010.

[6.3] R. Baets, "Chapter 3: Thin Films," in *Course of Microphotonics*, ed, 2010.

[6.4] C. A. Flory and R. C. Taber, "High performance distributed Bragg reflector microwave resonator," *Ultrasonics, Ferroelectrics, and Frequency Control, IEEE Transactions on*, vol. 44, pp. 486-495, 1997.

[6.5] M. L. Crespo, "DBR-based Cavity Microwave Sensor," Heriot Watt University, Internal Report.

[6.6] *Saint-Gobain Crystals*. Available: http://www.crystals.saint-gobain.com/

[6.7] *Kyocera International Inc.* Available: http://americas.kyocera.com/kicc/industrial/crystal.html

[6.8] *Logitech UK*. Available: http://www.logitech.uk.com/products-solutions/products-and-accessories/consumables/saw-blades-cutting-wires.aspx

[6.9] M. Kumagai, N. Uchiyama, E. Ohmura, R. Sugiura, K. Atsumi, and K. Fukumitsu, "Advanced dicing technology for semiconductor wafer -Stealth Dicing," in *Semiconductor Manufacturing, 2006. ISSM 2006. IEEE International Symposium on*, 2006, pp. 215-218.

7 Conclusions and Future Work

The main objective of this thesis was to investigate a microwave sensing device for small volume fluids. A microwave E-plane waveguide configuration was designed and modelled, and integration of the microfluidic channels into the waveguide was achieved. An extensive literature review was carried out to discover which microwave sensing techniques had already been employed. Many variations of waveguide structures were discussed including cavity resonators, coplanar waveguides, and Terahertz frequency devices. It was clear that low frequency structures did not offer the sensitivity required for such devices, therefore a device with a frequency greater than 10 GHz was chosen.

A waveguide aperture E-plane filter was designed with optimised sensing capability, i.e. narrow band resonant features, using the software package Ansoft HFSS^{TM}. A standard X-band waveguide was fabricated from aluminium and the E-plane filter was then tested within this waveguide. Simulation results from HFSS and the experimental results were in good agreement. The next step was to integrate a microfluidic channel for small volume fluids.

Various microfluidic structures were then designed and fabricated for integration. Various materials for the fabrication of these channels were also discussed. SU-8, a common micromachining photoresist, was found to be an inadequate solution due to the current fabrication facilities available. As the microfluidic channels were only to be used once, especially when testing biological samples, other appropriate materials were investigated. PDMS was also a material that was difficult to work with as it is a highly viscous substance and therefore difficult to control when fabricating small microfluidic channels. As both of these materials were liquid based, a solid material was sought to create the microfluidic channels. PMMA, which is sold under various trade names such as Plexiglas®, was used to create the final design for integration into the microwave sensing device. Microfluidic channels were etched onto the PMMA substrate using an Epilog CO_2 laser ablation system. A second sheet was then bonded to the engraved sheet using a heat and pressure system to seal the channels. This method was found to be quick, cheap and highly repeatable once the engraving procedure was established. Straight channels as well as channels with autonomous capillary pumps were fabricated.

Experimental results were presented for the successful microfluidic channel designs. Various fluid samples were tested including water/alcohol dilutions, animal blood and solid particulates in water. The final results were then compared to a simplified model in Ansoft HFSS. The results from the simulated comparison showed some discrepancies due to the irregularities within the microfluidic channels as well as the oversimplified model in HFSS. The simulations also did not include the exact permeability values for the tested materials and the microfluidic chip was also excluded from the simulation model.

A second device was then considered that would eliminate moving parts. A Bragg reflector was investigated as a possible solution. A Bragg reflector works by causing reflections within a cavity using low loss dielectric material to concentrate the field within the device. With the concentrated field this acts similar to the near field interactions of the E-plane filter and can therefore be exploited as a sensing device. Various designs were investigated in the literature review. A simple design was chosen as a first prototype and is outlined in Chapters 6 and 7. Preliminary tests were then carried out on the fabricated device.

7.1 Future Work

Future work for this project includes the development of the E-plane resonator device. Manufacturing techniques such as die casting could be employed in order to limit the movement and facilitate the alignment of the E-plane filter. Other waveguide designs such as Substrate Integrated Waveguide (SIW) would also integrate the filter with the waveguide. Low loss materials such as Low Temperature Cofired Ceramic (LTCC) and Liquid Crystal Polymer (LCP) could also help facilitate the alignment issues discussed. These multilayer technologies offer highly integrated design possibilities as well as smaller devices allowing higher frequencies to be achieved. Both materials have low loss tangents making them ideal for microwave sensing. This therefore increases the sensitivity of the device as well as allowing the device to become more portable.

7.1.1 Low Temperature Co-fired Ceramic (LTCC)

Low Temperature Co-fired Ceramic (LTCC) is a multilayer packaging scheme using ‘green’ tape. In this ‘green’ state the ceramic is easily machined. The main advantage of LTCC is the low sintering temperature (around 850°C) that allows the inclusion of conducting metals such as silver, gold and copper. Ceramic has also a desirable dielectric

constant for use at high frequencies and very resistant to harsh environments withstanding temperatures up to 350°C. The integration of passive components is possible between the layers while active components can be mounted on the top making this a highly dense 3D packaging scheme. As each layer is fabricated independently they can be inspected individually before sintering for imperfections without the need to fabricate a whole new device. Two of the main techniques used at Heriot-Watt for the machining of the green tape are sandblasting and laser cutting. Below are examples of structures that can be machined using these techniques as shown in Figure 8.1.

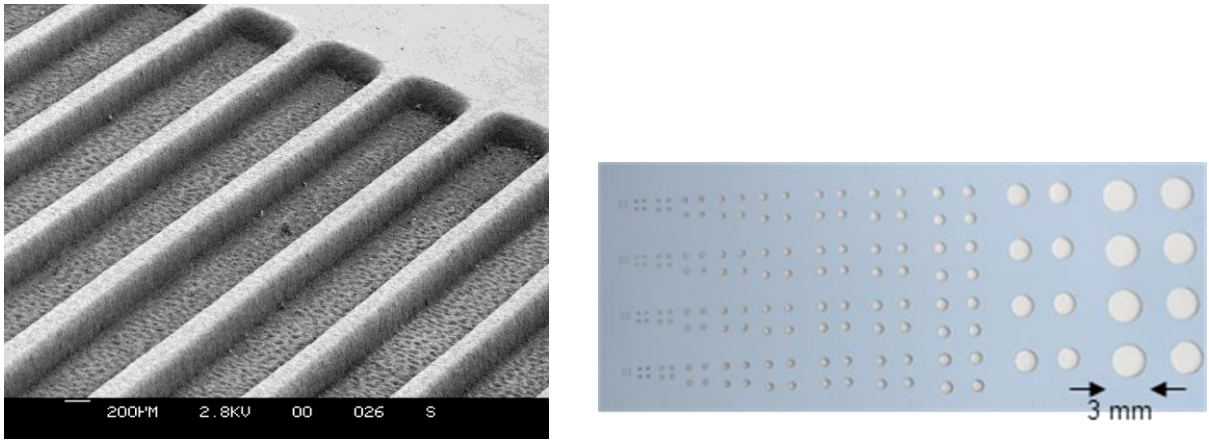

Figure 8.1 Left: sandblasted green tape. Right laser cut green tape [7.1].

Although sandblasting can achieve smaller features it also requires more time, preparation and the inclusion of a hard mask. By laser cutting there is no need for a mask as the pattern is achieved through computer design. In this way the laser cutter acts like a printer as described in Chapter 4.

7.1.2 LTCC cavity fabrication

A small embedded cavity in LTCC was investigated as a possible method for fabricating the microwave E-plane filter sensing device using this material. The design is shown below, Figure 8.2.

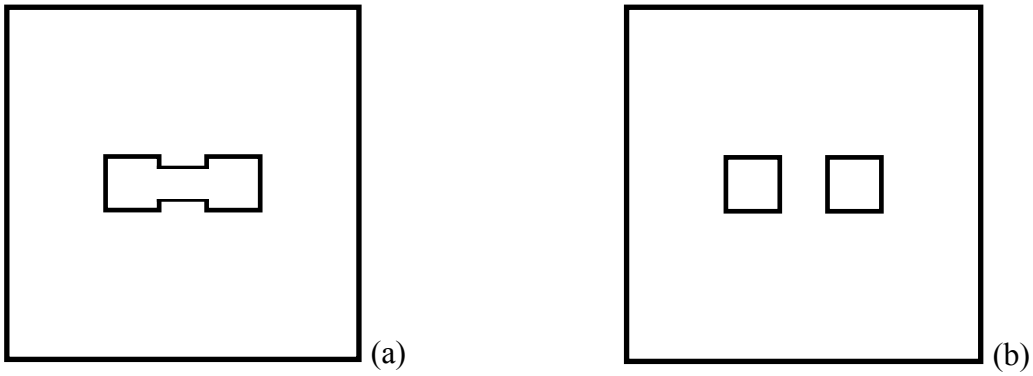

Figure 8.2 LTCC layer designs for a cavity

The designs above were used to create a cavity 0.82 mm x 1.24 mm, 10 times smaller than the X-band WR90 dimensions. Two square vias were cut either side of the cavity as shown in Figure 8.2 above for the VNA probes. The initial design included one (b) layer for the bottom and top covers seven (a) layers for the cavity. The cavity was filled with a sacrificial material to ensure that it did not collapse during the initial bonding. These layers were then aligned and bonded at 10 MPa at 70°C for 8 minutes. The sacrificial material was removed before the bonded layers were then sintered at 850°C for 150 minutes. The first cavity produced using carbon paste as a sacrificial material is shown in Figure 8.3.

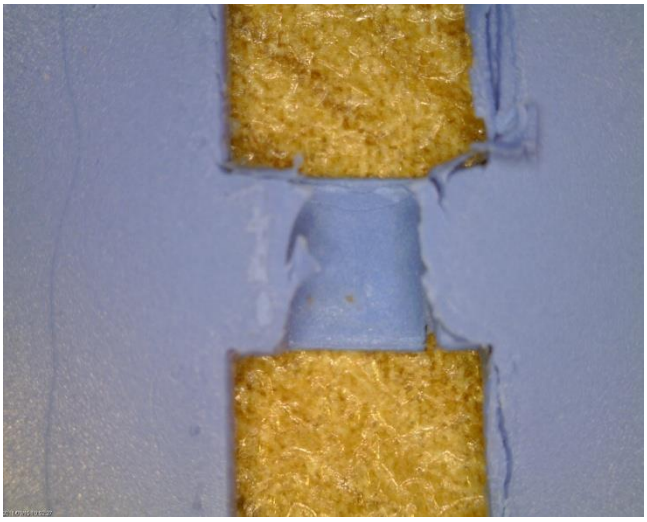

Figure 8.3 LTCC cavity using carbon paste as a sacrificial material

As the photograph shows above the cavity was extremely fragile and the carbon paste sacrificial material did not ensure its integrity. Another sacrificial material, silicone, was used to create an open and closed cavity. The results are shown in Figure 8.4.

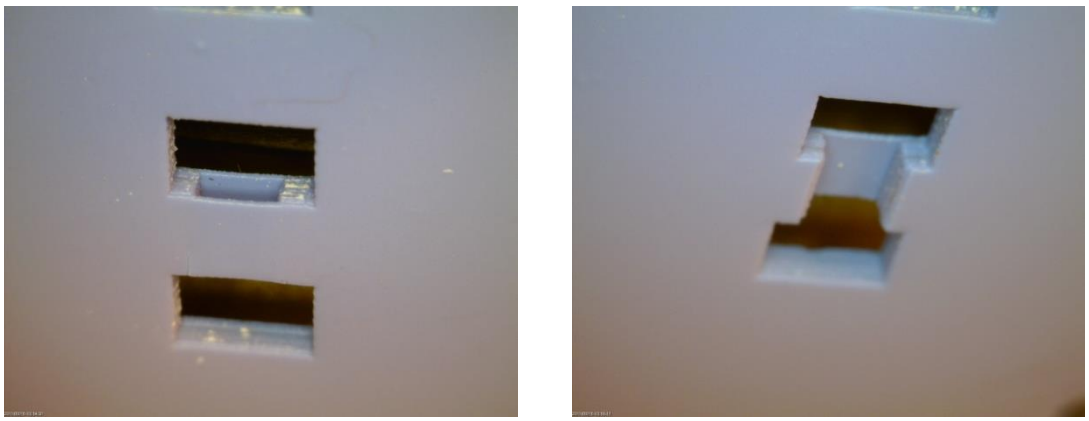

Figure 8.4 Left: closed; right: open LTCC cavity using silicone as a sacrificial material

This method of using silicone as a sacrificial material proved to work well. Future work for this would be to design and incorporate the E-plane resonator and a microfluidic capillary for sample delivery.

7.1.3 LCP

Liquid Crystal Polymer is another multilayer packaging technique that is used in fabricating microwave electronics due to its low relative dielectric constant as well as the readily available laminates. Each laminate layer is machined/etched/printed then sandwiched with a bonding layer. The LCP stack is then aligned and this is then laminated at 230°C for approximately 1 hour.

7.1.4 LCP cavity fabrication

Similar to the LTCC designs ablation of a cavity in LCP were attempted using the Epilog laser system. Firstly layers of LCP were laminated to ensure a thickness of approximately 800 µm. This was carried out before ablation as it was documented that when trying to create cavities in LCP it is difficult to obtain straight walls or collapse of the cavity due to the bonding layers used in this process. Various settings for the Epilog laser system were tried to ablate this LCP stack. The results of these are shown in the following photographs in Figure 8.5.

Figure 8.5 LCP ablation attempts using the Epilog laser ablation system

As Figure 8.5 shows, the layers proved to be too thick to form a clean cavity.

7.2 Bragg Sensor

Future work to be carried out on the Bragg Sensor include extensive experimental work, further resonant enhancements through modelling and further investigations into fabrication techniques. Numerous materials can be characterised and analysed using this system. By exploiting the external sample point, solids and liquids can be investigated. For automation of this system, integration of microfluidic structures would be required. Further modelling to improve the Q-factor of the device is required. Other low loss dielectric materials can also be investigated for future fabrications.

7.3 Conclusion

Overall the results from the E-plane sensor device were promising however slight variations in fabrication of the microfluidic channels as well as instability of the E-plane filter resulted in poor repeatability of the measurements. The Bragg device shows promising preliminary simulations and results, with greater stability than the E-plane sensor.

In conclusion the original contribution of this thesis can be summarized as follows:

- A prototype microwave resonator with integrated microfluidics has been presented. Design considerations using finite element analysis methods were discussed. Microfluidic channel fabrication techniques were investigated and tested. Extensive testing of the prototype device using various microfluidic designs was carried out. Materials under test included: Methylated Spirit/Water concentrations, lubricant and motor oils and animal red blood cell concentrations. A resonant frequency change of 2 MHz was observed between that of DI water and the cell suspension media PBS. A 0.05 dB difference was also observed between pure 100% PBS and the sample containing 1:200 ratio of mouse red blood cells.
- A second prototype Distributed Bragg Reflector (DBR) device was proposed as a sensing device. Design of the DBR was carried out using Ansoft HFSS. A Q-factor of 1,942 was obtained in the simulations. Fabrication and initial testing of the device was conducted. Resonant frequency changes up to 20 MHz were observed between various liquid samples including water and oil.
- Several manufacturing techniques were described and used throughout this thesis. These included:
    - Photolithography processes
    - Soft lithography
    - Laser ablation
    - Multilayer fabrication technologies
        - Low Temperature Co-fired Ceramic
        - Liquid Crystal Polymer

7.4 References

[7.1] Y. Lacrotte, "Novel Patterning Technology for the LTCC based Packaging of an Optical Encoder," Engineering and Physical Sciences, Heriot Watt University, 2013.